HIGH DENSITY SUPERSOLIDUS LIQUID PHASE SINTERING OF STEEL POWDERS

by

ERIN YOUNG
B.Eng., Materials Science and Engineering
McMaster University, 1999

A THESIS SUBMITTED IN PARTIAL FULFILMENT OF
THE REQUIREMENTS FOR THE DEGREE OF

MASTER OF APPLIED SCIENCE

in

THE FACULTY OF GRADUATE STUDIES
Department of Metals and Materials Engineering

We accept this thesis as conforming
to the required standard

THE UNIVERSITY OF BRITISH COLUMBIA

October 2001

In presenting this thesis in partial fulfilment of the requirements for an advanced degree at the University of British Columbia, I agree that the Library shall make it freely available for reference and study. I further agree that permission for extensive copying of this thesis for scholarly purposes may be granted by the head of my department or by his or her representatives. It is understood that copying or publication of this thesis for financial gain shall not be allowed without my written permission.

Department of Metals and Materials Engineering

The University of British Columbia
Vancouver, Canada

Date Oct. 29, 2001

DE-6 (2/88)

Abstract

In this study, supersolidus liquid phase sintering (SLPS) of an industrially relevant Fe-C-Mo alloy powder was investigated with particular attention to the evolution of density and porosity. The material was produced by mixing graphite with a pre-alloyed Fe-Mo alloy. Differential Scanning Calorimetry (DSC) was employed to determine the solidus and liquidus temperatures of the alloy, and a high temperature experimental furnace was used to provide information on density evolution as a function of time and temperature. Specimens were sintered both in the solid state and in the presence of a supersolidus liquid phase, over a range of temperatures between 1000 and 1300°C, providing both densification data and metallographic specimens. Diffusion calculations and thermodynamic calculations using Thermocalc™ software were performed to complement the experimental data.

On heating, several processes occur in the material prior to liquid formation, including delubrication of the material, phase transformation, carbon diffusion, and solid state sintering. It was determined that the carbon diffusion is rapid and the bulk concentration is homogeneous at temperatures well below those of first liquid formation. Following homogenization, some solid state sintering takes place, and while minimal densification occurs, the number of pores decreases markedly from the green state.

At temperatures above the solidus where a liquid phase is present, it was found that densification occurs in two regimes. The first regime involves a fast rate of densification due to the capillary forces of the liquid, followed by a second, slower regime of densification that is governed by pore removal processes.

The maximum amount of densification possible is determined by the fraction of liquid present, as defined by the sintering temperature. If the temperature is low, insufficient liquid is present and densification is extremely slow. If the temperature is too high, the liquid promotes distortion of the semi-solid sample; in addition, pores subject to sufficient internal gas pressure are capable of expansion in the weakened structure, actually increasing the volume of porosity. Samples were, however, successfully sintered to densities approaching theoretical in a narrow temperature window intermediate between these extremes. Recommendations for the development of robust sintering practices are offered.

Table of Contents

List of Tables

List of Figures

Acknowledgements

This thesis could not have been completed without the assistance of many people. First mention must go to my supervisor, Dr. Warren Poole, for his contributions to the work in every possible respect, and particularly for his adoption of a lone graduate student in powder metallurgy. Thanks are also due to Dr. Indira Samarasekera for her generous financial support of the project, and to Stackpole Ltd., particularly Andrew Dempsey, for providing assistance and research material.

In a more technical capacity there were also many contributions; Pat Wenman for his dedication to building the most accurate and reliable experimental apparatus possible, Rudy Cardeno for sharing his significant expertise with image analysis and metallography, Grant Caffery and Pierre Constantineau for valuable technical suggestions, assistance and discussion, and Fateh Fazeli for his proficiency and assistance with the Thermocalc software. I am also grateful for the use of the Differential Scanning Calorimeter at the University of Waterloo, generously provided by Dr. Stephen Corbin, and his contributions to the analysis of the results.

I also owe a great deal to my friends and family in Ontario for their continued support and encouragement of my studies, as well as my friends in Vancouver, who provided a wonderful atmosphere in which for me to complete this work. And of course to Joey, whose support in every respect was unconditional and absolute. Thank you.

Chapter 1: Introduction

1.1 Powder Metallurgy Overview

Powder metallurgy (P/M) is a materials processing route that exists not only as a well-established sub-discipline of materials science, but also a substantial parts and products industry, with estimated sales of over $5 billion a year in North America alone and shipments of over 1 million tons worldwide[1]. P/M offers a cost effective method of net or near-net shape component production, with considerable scope in material properties, chemistry, heat treatment and microstructure (German, 1994). These advantages stem from the flexibility inherent in the traditional P/M processing route, which involves blending elemental metal powders to give a desired composition, cold pressing in a die to form green parts, and then sintering in a high temperature furnace to promote metallurgical bonding and densification. In particular, the time and temperature variables of the sintering operation may be controlled to achieve specific microstructural features and phase distributions in the finished product. Post sintering operations such as carburising, nitriding and heat-treating may also be performed to realize more specialized properties.

As a result of this flexibility, P/M processes find application in the manufacture of hundreds of diverse products, from superalloy turbine components and tungsten lamp filaments to stainless steel surgical instruments and carbide cutting tools. However, niche applications such as these are far outweighed by the principal success of P/M, which lies in the extensive and increasing use of iron and steel powders by the automotive industry (see Figure 1.1). A typical North American passenger car produced in the year 2000 contains more than 15 kg of powder metal parts, a figure that has more than doubled in the last twenty years and is continuing to escalate, as illustrated in Figure 1.2.

1.2 Rationale

In the automotive industry there exists a perpetual drive for increased economy and efficiency in all aspects of production. As a consequence, the increase in P/M parts per vehicle has come at the expense of many less cost effective traditionally cast and

[1] Metal Powder Industries Federation Website: www.mpif.org (2000)

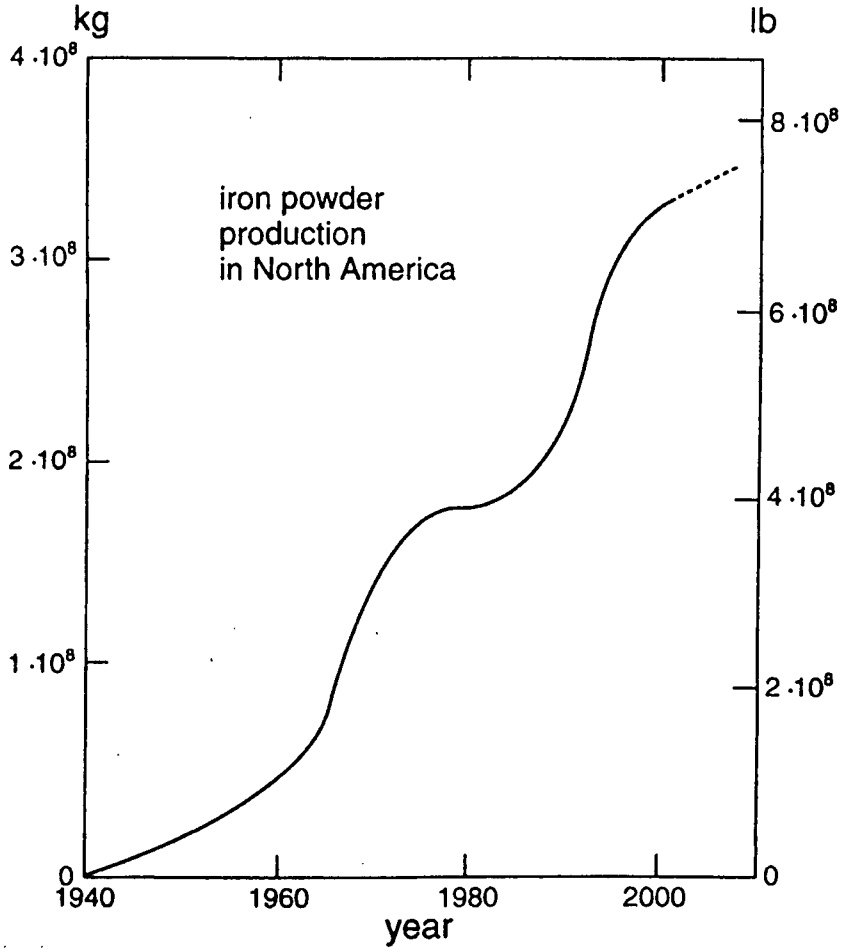

Figure 1.1 Iron powder production in North American (German, 1998)

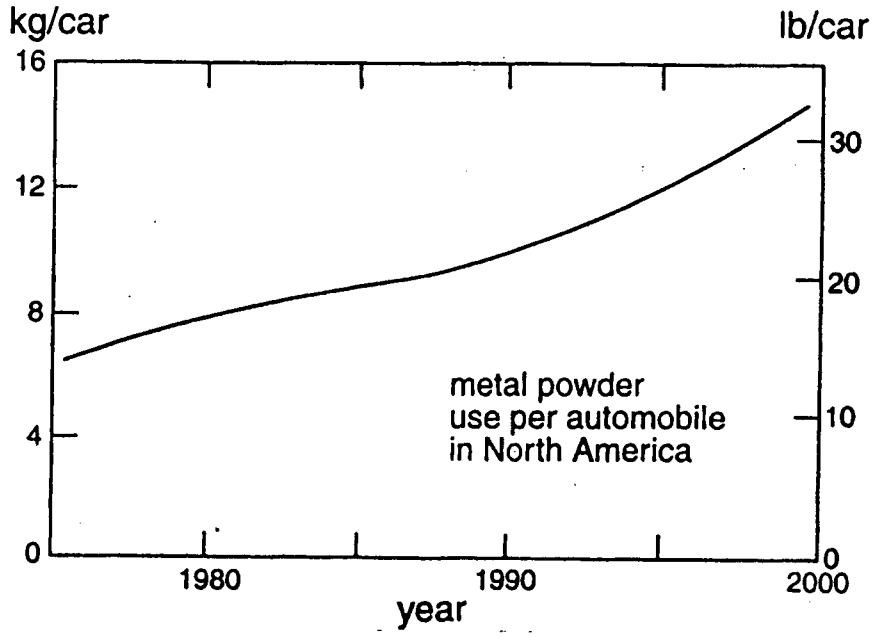

Figure 1.2 Metal powder use per automobile in North America (German, 1998)

machined parts (made primarily of iron and steel alloys) that have been displaced by P/M parts. The principal advantages of P/M as seen by the automotive industry are 1) net shape processing of complex parts; 2) high production quantities; and 3) modest processing costs. Thus it is in the industry's best interest to produce as many parts as is practical using P/M methods.

However, although traditionally produced P/M parts are suitable for many automotive applications (including parts such as gears, bearings, sprockets, clutch plates), a broader scope of applications has, until recently, been somewhat limited due to an inability to match all major properties of P/M parts to those of traditional wrought steel parts. This can only be achieved when the densities of the P/M parts approach wrought steel values (Jones et al, 1996). Full density is an important specification for some structural parts and critical components such as connecting rods. The current ferrous powder metallurgy industry can produce fully dense (>99% of theoretical density) steels by mechanically aided processes such as hot isostatic pressing (HIP) and powder forging (P/F), or by providing a driving force for accelerated sintering with very small (and expensive) initial powder sizes. However, there is much interest in using a conventional press and sinter process as described above to achieve fully dense ferrous products. While powder forging is an extremely effective process, tool wear can be relatively high leading to dimensional and shape attributes that may be inferior to traditional P/M methods, which also enjoy an inherent economic advantage over mechanical processes.

1.3 Supersolidus Liquid Phase Sintering

In order to maximize the potential of P/M parts to displace wrought steel parts, a Canadian powder metallurgy company, Stackpole, Ltd., has developed a new process (U.S. Patent # 5641922) that can achieve full sintered density in parts made from high carbon (0.8-2.0 wt%) steels, utilizing a process termed supersolidus liquid phase sintering. The finished products exhibit excellent mechanical properties very similar to those of wrought steel, including a high modulus, good tensile properties, high toughness, and high fatigue strength. The suitability of such ultrahigh carbon steels to automotive applications has been well recognized (Lesuer et al. 1996).

The process of supersolidus liquid phase sintering is a special case of liquid phase sintering that involves heating a pre-alloyed powder to a temperature above the solidus line on the phase diagram in order to form solid-liquid mixture. The primary advantage is that the liquid and solid are compositionally similar, so good wetting is achieved, allowing full densification. The supersolidus sintering process will be defined and discussed in more depth in the literature review presented in Chapter 2.

From an industrial perspective, the primary advantage of supersolidus processing is the ability to make full-density steel parts using the economically attractive traditional P/M press-and-sinter processing route. As mentioned, this involves blending metal powders together, adding an organic lubricant to aid compressibility, pressing in a die to a desired shape and then passing the so-called "green" compact through a sintering furnace to achieve full density. After sintering, the high carbon steels are heat treated in order to spheroidize the high carbon content of the alloy, and thus develop the desirable mechanical properties. This process flow diagram indicating process details is shown in Figure 1.3, with a schematic of the sintering furnace steps shown in Figure 1.4. The maximum sintering temperature selected for the alloy is 1285°C, and it is typically held between 40 and 60 minutes at that temperature. The furnace atmosphere is typically reducing, which aids the delubrication process and removes oxides from the surface of the metal powders.

1.4 Present Work

While standard liquid phase sintering has been a viable production route for several decades, supersolidus sintering has not been practiced on a full-scale production level, primarily due to processing sensitivities (German, 1997); there exists a narrow temperature range for sintering between densification and shape distortion. The process has secured a somewhat greater level of interest on the academic side, and while currently there is more knowledge about methods of avoiding distortion, fundamental knowledge of the process is still relatively incomplete. Each alloy system behaves differently during sintering.

For example, after supersolidus sintering of the high carbon steels described, extremely large (>200 μm) pores can be observed. These pores are irregularly shaped and

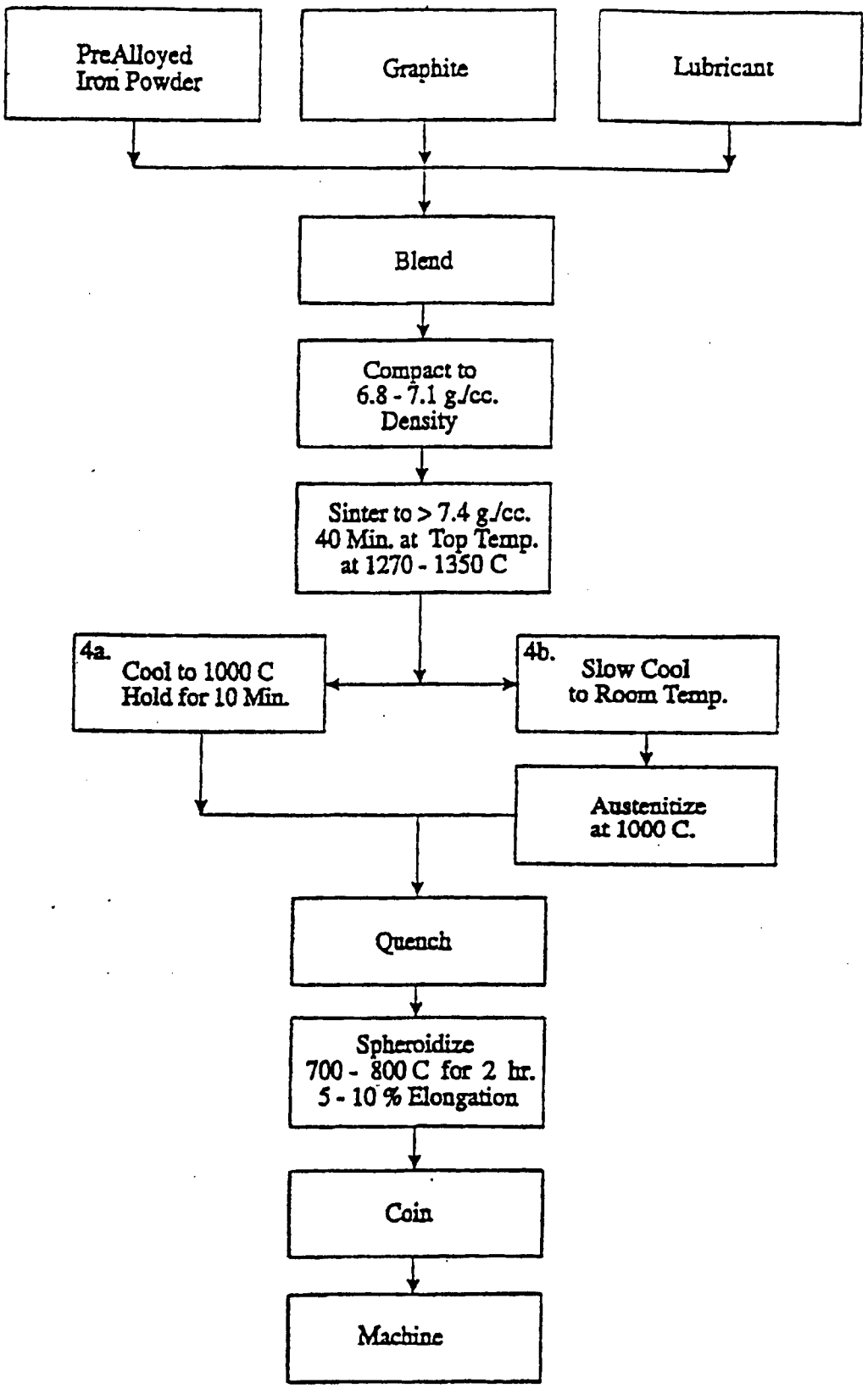

Figure 1.3 Process flow diagram for the SinterDens™ full density process

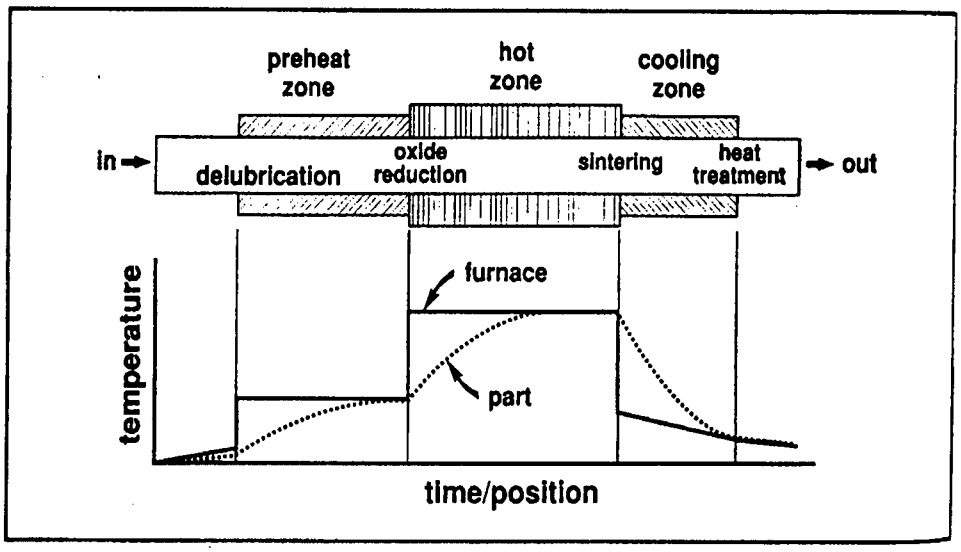

Figure 1.4 Sequence of operations occurring in a typical sintering furnace (German, 1994)

can have aspect ratios of up to 4. Obviously such pores are undesirable as they greatly reduce fatigue life when the part is in service by acting as crack initiation sites. It would be desirable to reduce the maximum pore size in the product to <40 μm and ensure that the pores are spherical in shape. The underlying causes of the irregular porosity are unclear, and it is obvious that an issue such as this must be resolved before full-scale production.

The current work has been undertaken in order to provide more information on the supersolidus liquid phase sintering of high carbon steels. The broad objective of the work is to perform a characterization of the sintering process for these materials, and ultimately, provide insight on the porosity evolution during the process.

The approach taken was primarily an experimental one; a systematic experimental program was designed and executed to serve the objectives of characterization of two different high carbon steels. The study was carried out from a process-oriented point of view, as the variables associated with the sintering cycle (time, temperature) were focused on while green density, powder composition, powder size distribution and furnace atmosphere were held constant.

Two types of experimental techniques were employed. Differential scanning calorimetry (DSC) was performed to identify, categorize and quantify thermal events occurring during sintering, while experiments in a high temperature experimental furnace served to investigate densification behaviour and microstructural and porosity evolution. Characterization techniques and thermodynamic calculations provided additional insight.

This thesis is intended to document the work performed and consists of six chapters. Chapter 2 provides a review of some of the pertinent literature available on supersolidus liquid phase sintering and the alloy system investigated. Chapter 3 outlines the experimental and analytical procedures followed, while Chapter 4 presents the results of the experimental work. Chapter 5 puts forward a discussion of the results and additional analysis that is organized as a temporal progression through the sintering cycle. Finally, Chapter 6 summarizes the major conclusions and possible implications of this work and proposes a direction for future study on this topic.

Chapter 2: Literature Review

This chapter presents the fundamentals of the theory developed on the topic of supersolidus liquid phase sintering, as well as providing a summary of some of the experimental work detailed in the literature to date. This summary indicates results relevant to the present work as well as describing some of the approaches taken to studying this phenomenon. While it is not meant to be an exhaustive review, this chapter should provide a sufficient foundation for the subject matter covered in this thesis.

2.1 Sintering

2.1.1 Driving Force

In powder metallurgy, the term "sintering" is used generally to describe the metallurgical bonding of packed particles at temperatures in excess of 0.5 T_m, the melting point of the material. This bonding may or may not be accompanied by densification. The excess surface free energy of the powders provides the initial driving force for the sintering process; as sintering progresses pores and thus internal free surfaces are eliminated by the replacement of the solid-vapour interface by the lower energy solid-solid one. This is achieved by the formation of interparticle "necks", and the simultaneous disintegration of the three-dimensional pore network present in the green compact. Using thermodynamic considerations it may be shown (as, for example, in Borg and Dienes, 1992) that the driving pressure ΔP associated with a curved surface relative to a flat surface (due to excess surface energy) is

$$\Delta P = \gamma_s \left(\frac{1}{R_1} + \frac{1}{R_2} \right) \tag{2.1}$$

where γ_s is the surface energy of the material and R_1 and R_2 are the two principal radii that define the curvature of the surface. It should be noted that this equation represents only the isobaric, isothermal case for a system of constant composition. For spherical particles of radius R under the same conditions, equation 2.1 becomes

$$\Delta P = \frac{2\gamma_S}{R} \tag{2.2}$$

For a realistic surface energy of 1 J/m^2, the driving pressure is obviously quite small, and the implication is that high temperatures are the means necessary to achieve sintering by atomic transport. Another important consequence is that small particles will have a much greater driving force for sintering (German, 1994).

2.1.2. Sintering Mechanisms

All of the mechanisms contributing to sintering involve transport processes that may be classified into two categories. There are surface transport processes such as surface diffusion and evaporation-condensation, and bulk transport processes including lattice diffusion, boundary diffusion, and dislocation creep. While all these mechanisms are capable of contributions to particle bonding, only the bulk transport processes contribute to densification, that is, the rate at which particle centers approach each other and thus achieve compact shrinkage. If one of the mechanisms listed can accomplish removal of matter from the grain boundary that separates the two particles or from dislocations in the neck region, then it is classed as densifying. Non-densifying mechanisms are those that do not move particle centers together. For example, grain growth occurs by lattice diffusion at high sintering temperatures, but does not result in densification. A simple illustration of densifying and non-densifying mechanisms is given in Figure 2.1. Different mechanisms are operational under different sintering conditions, and in a simple, one component solid state sintering system, it is possible to predict the sintering rate (rate of neck growth) by identifying the dominant sintering mechanism. A good summary of this technique and the mechanisms involved is given in Ashby (1974).

Recognizing the dominant sintering and densifying mechanisms allows for the identification of important parameters and how it is possible to manipulate them to enhance the sintering process. Possible enhancements include controlling temperature for optimal diffusivity, applying external stress, and adjusting composition to stabilize phases with a high sintering rate (German, 1994). Another important method of enhancing sintering is the introduction of a liquid phase.

2.2. Liquid Phase Sintering (LPS)

Many advantages are realized by the introduction of a liquid phase to the sintering process. Primarily, diffusivities in the liquid phase are high, and may be orders of magnitude greater than in the solid state, particle rearrangement using the liquid as a lubricant may occur, resulting in densification, rough edges are dissolved in the liquid, allowing efficient packing and finally the liquid introduces capillary forces that draw liquid in to fill pores. Capillary forces to a large extent are responsible for the high degree of densification possible by LPS. A schematic diagram of LPS is shown in Figure 2.2.

2.2.1 Wetting and Capillarity

Successful LPS depends highly on the properties of the liquid phase and its relation to the solid phase. A high solubility of the solid in the liquid aids densification (German, 1985), while good wetting and grain boundary penetration of the solid by the liquid are paramount (Allibert, 1998). Wetting describes the equilibrium between three phases; solid, liquid and gas, and dictates the contact angle θ, as shown in Figure 2.3 for a sessile drop, where γ_{sv} is the interfacial surface energy between solid and vapour, γ_{sl} that between solid and liquid, and γ_{lv} is that between liquid and vapour. For mechanical equilibrium, the surface tension vectors must balance:

$$\gamma_{sv} = \gamma_{sl} + \gamma_{lv} \cos\theta \tag{2.3}$$

Equation 2.3 can then be manipulated to give the contact angle

$$\cos\theta = \frac{\gamma_{sv} - \gamma_{sl}}{\gamma_{lv}} \tag{2.4}$$

where $\theta = 0^\circ$ implies complete wetting, and $\theta = 180^\circ$ implies no wetting. As surface energies are often highly dependent on surface purity (Prutton, 1998), contaminants on powder surfaces may drastically alter the wetting behaviour in a particular system.

The dihedral angle Ψ, illustrated in Figure 2.4, describes the solid-solid grain boundary penetration capability of the liquid, and is also determined by the surface energy;

$$\gamma_{ss} = 2\gamma_{sl} \cos\frac{\Psi}{2} \tag{2.5}$$

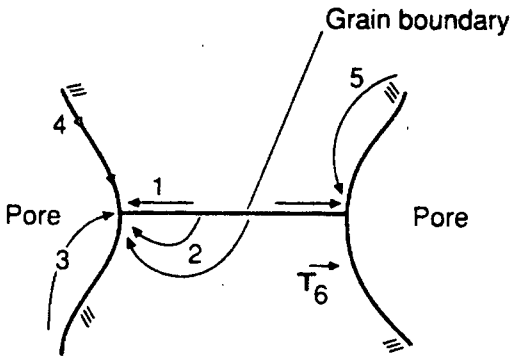

Mechanism	Densifying	Non-densifying
1. Grain boundary diffusion	×	
2. Volume diffusion	×	
3. Evaporation/condensation		×
4. Surface diffusion		×
5. Coarsening by volume diffusion		×
6. Dislocation (T) creep	×	

Figure 2.1 Schematic of various atomic transport paths for two sintering particles showing densifying and non-densifying mechanisms (Evans and DeJonghe, 1991)

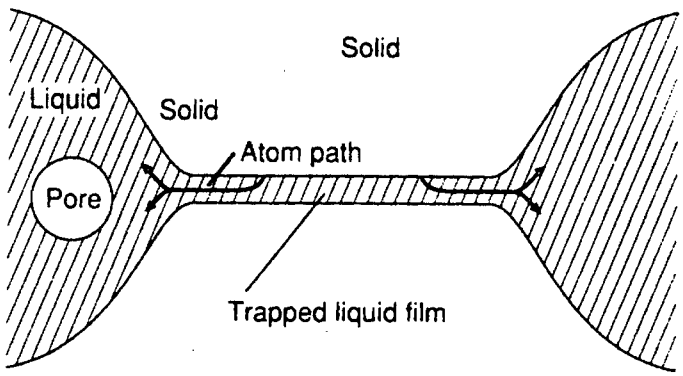

Figure 2.2 Schematic of the densification mechanism during liquid phase sintering (Evans and DeJonghe, 1991)

Complete penetration occurs when γ_{sl} is less than ½ γ_{ss}, the solid-solid surface energy (i.e. $\Psi = 0$). Using the dihedral angle, it is now possible to calculate the capillary force. In Figure 2.5, a liquid bridge is shown between two particles, where X is the meniscus height. Heady and Cahn (1970) calculate the force F exerted on the particles as

$$F = \pi(X^2/4)\Delta P + \pi X \gamma_{lv} \cos\Psi \qquad \Delta P = -\gamma_{lv}/R \tag{2.6}$$

When the force is attractive (ie. the case of good wetting), the particle separation goes to zero and densification occurs. It is worth noting that to achieve a large capillary force, a small particle size is required, often on the order of 1 μm (German, 1997).

2.2.2 Stages in Liquid Phase Sintering

Liquid can be introduced into the compact in several ways, usually by mixing two powders of differing chemistry (German, 1985). A low melting point component may provide the liquid, or the blended chemistry may result in eutectic liquid formation. In these cases the liquid may be transient or persistent throughout the sintering process. In the case of supersolidus sintering, a prealloyed powder is heated to a temperature between the liquidus and solidus on the phase diagram; this will be discussed in more detail in Section 2.3.

Kingery (1959) argues that liquid phase sintering can be generally characterized as a four-stage sequence:

(1) Formation of liquid phase over a certain temperature range and subsequent penetration of liquid between powder particles.
(2) Extensive rearrangement of particles acting under capillary forces.
(3) Solution-precipitation; at wetted liquid-particle interfaces solid material dissolves and precipitates elsewhere. Solution-precipitation may result in microstructural coarsening.
(4) Isolated pores fill with liquid; contacts grow, maximum density is reached.

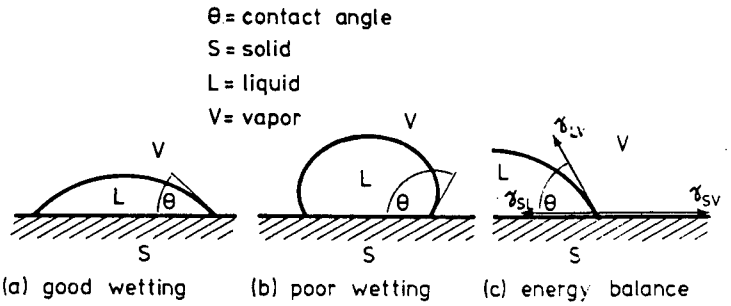

Figure 2.3 The contact angle defined by the solid-liquid-vapour equilibrium (German, 1985)

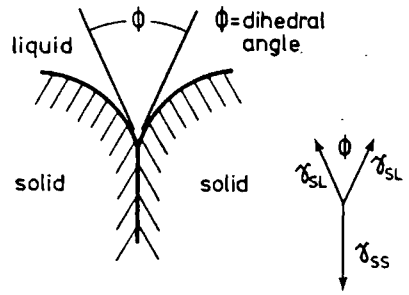

Figure 2.4 The dihedral angle and surface energy equilibrium between two intersecting grains with a partially penetrating liquid phase (German, 1985)

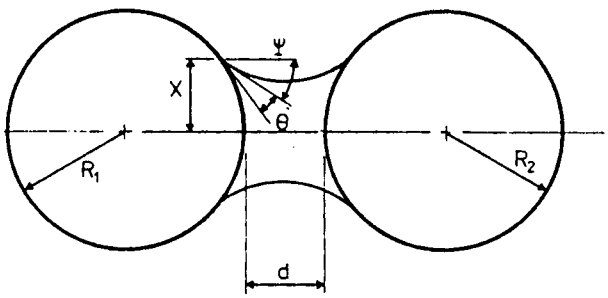

Figure 2.5 Two spherical particles with a liquid bridge and the defining geometric parameters of the wetting force (German, 1985)

It is to be noted that Stage (2), rearrangement of particles by capillary forces, plays an especially important role in the extensive shrinkage observed during LPS, and was first studied by Cannon and Lennel (1953) and then described extensively by Kingery (1959), who proposed that viscous flow is responsible. The viscous flow model is well accepted (German, 1990), and the degree of densification is dependent on only particle size R and solubility. Shrinkage in length, $\Delta L/L_o$ is increases with time t as

$$\Delta L / L_o \sim t / R \tag{2.7}$$

Unfortunately the kinetics of rearrangement is extremely rapid, precluding detailed experimental study.

2.3 Supersolidus Liquid Phase Sintering (SLPS)

In supersolidus liquid phase sintering (SLPS), a prealloyed, or solid solution powder compact is heated to an intermediate temperature between the solidus and liquidus. An amount of liquid, prescribed by the phase diagram at the specific sintering temperature, then forms both at locations inside the grains and at the grain boundaries within the particles. Typically, liquid amounts used in practice vary from 5% to 65% as reported in the review by German (1990). SLPS is a special case of LPS, where the following conditions are held (Lund and Bala, 1974):

(1) Throughout sintering, the compact is a heterogeneous solid liquid mixture ie. there is a persistent liquid phase.
(2) The solid – liquid volume fractions and compositions are constant throughout the sintering process.
(3) There is a high mutual solubility of the solid and liquid, due to similar composition.
(4) The liquid has ideal wetting properties, with a contact angle of 0^o. Wetting is immediate, uniform, and perfect (Cambal and Lund, 1972).

It is this last point that provides SLPS the capability of achieving high densities. The liquid formed inside the particles easily spreads to the particle contacts, yielding a large capillary force that acts on weakened, semi-solid particles (German, 1997). As in

regular LPS, a viscous flow model for densification is applicable to SLPS. The fragmenting process is illustrated schematically in Figure 2.6. The large capillary force suggests that rearrangement is the most important stage in densification during SLPS, and the much slower solution-precipitation stage that aids regular LPS densification is unimportant. Indeed, it is observed that once a sufficient amount of liquid exists to fragment particles into individual grains, then densification can be quite rapid (Cambal and Lund, 1972), a definite advantage from a processing point of view. Another important advantage is that because the particles eventually fragment, and it is these fragmented grains that eventually influence capillarity, small initial powder sizes are not necessary for successful SLPS, as they are for traditional LPS.

2.3.1 Significance of the Phase Diagram

It is obvious that the phase diagram plays an important role in SLPS, since the onset of densification is reliant primarily on the formation of a critical amount of liquid, as illustrated by the results of density achieved vs. sintering temperature for a nickel alloy (30 μm particle size, 0.62 green density) shown in Figure 2.7 (German, 1990). The shape of this curve is standard for alloys densified by SLPS. In addition, the extent of densification is dependent on the amount of liquid, as indicated in Figure 2.8 for a Fe-0.9%C alloy with 0.55 green density sintered above the solidus for 10 minutes. In addition, temperature also controls dimensional precision and microstructural coarsening during SLPS, and the identification of the (often narrow) optimal sintering window is of utmost concern, as illustrated in Figure 2.9.

German (1990) suggests a list of phase diagram attributes that may indicate the suitability of a system for SLPS. Figure 2.10 shows a generalized phase diagram displaying these attributes:

(1) A high concentration of alloying elements (X_a), leading to a wide separation of the liquidus and solidus temperatures. Because the dependence of the liquid volume fraction on temperature varies inversely with this separation, ease of process control will be improved with a wide separation. It is suggested that at least 100K is necessary in practice.

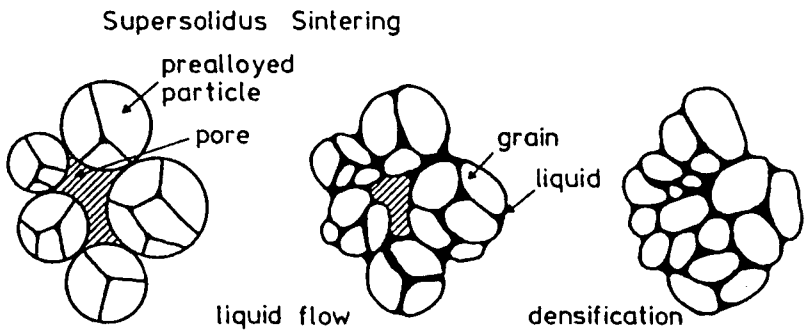

Figure 2.6 Liquid formation and particle fragmentation processes in a polycrystalline prealloyed powder heated to a temperature between the solidus and liquidus temperatures (German, 1990)

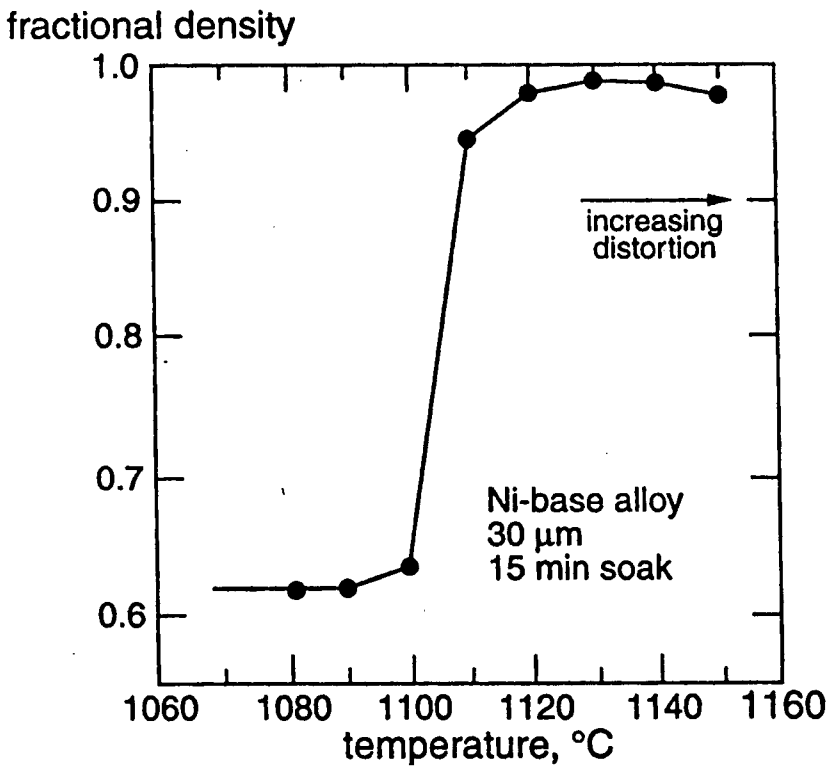

Figure 2.7 Sintered fractional density vs. sintering temperature for a 30 μm Ni-Cr-Co alloy with green density of 0.62 and 15 minute hold time at each temperature (German, 1990)

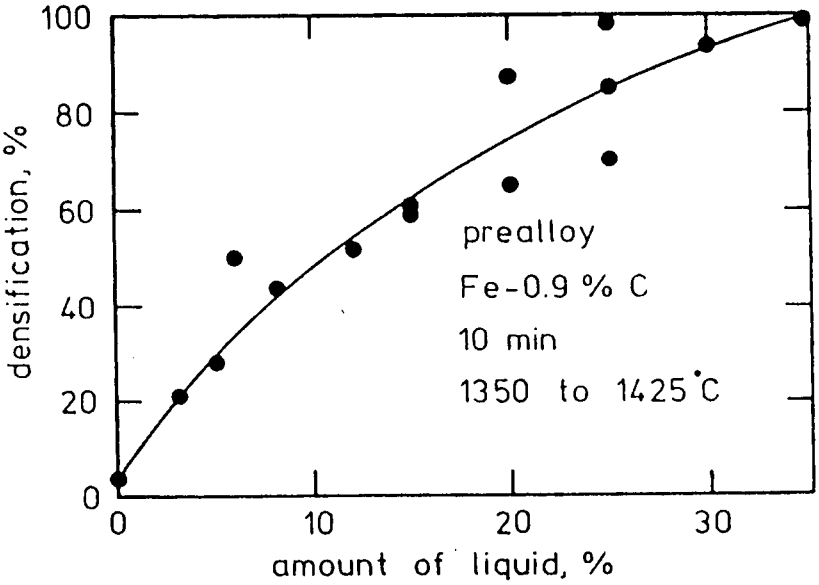

Figure 2.8 Sintered density vs. liquid content for prealloyed Fe-C processed with SLPS for 10 minute hold times (Lund and Bala, 1974)

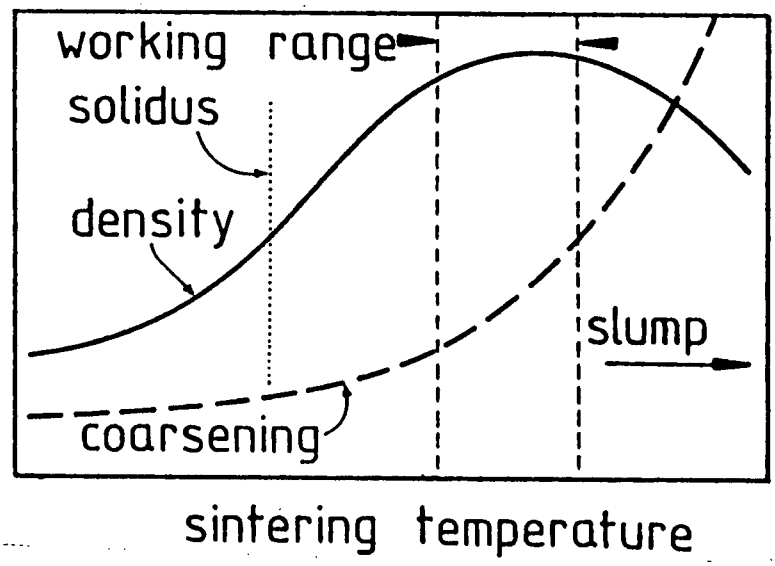

Figure 2.9 Generalized plot of density and microstructural coarsening as functions of the sintering temperature and the optimal working range (German, 1990)

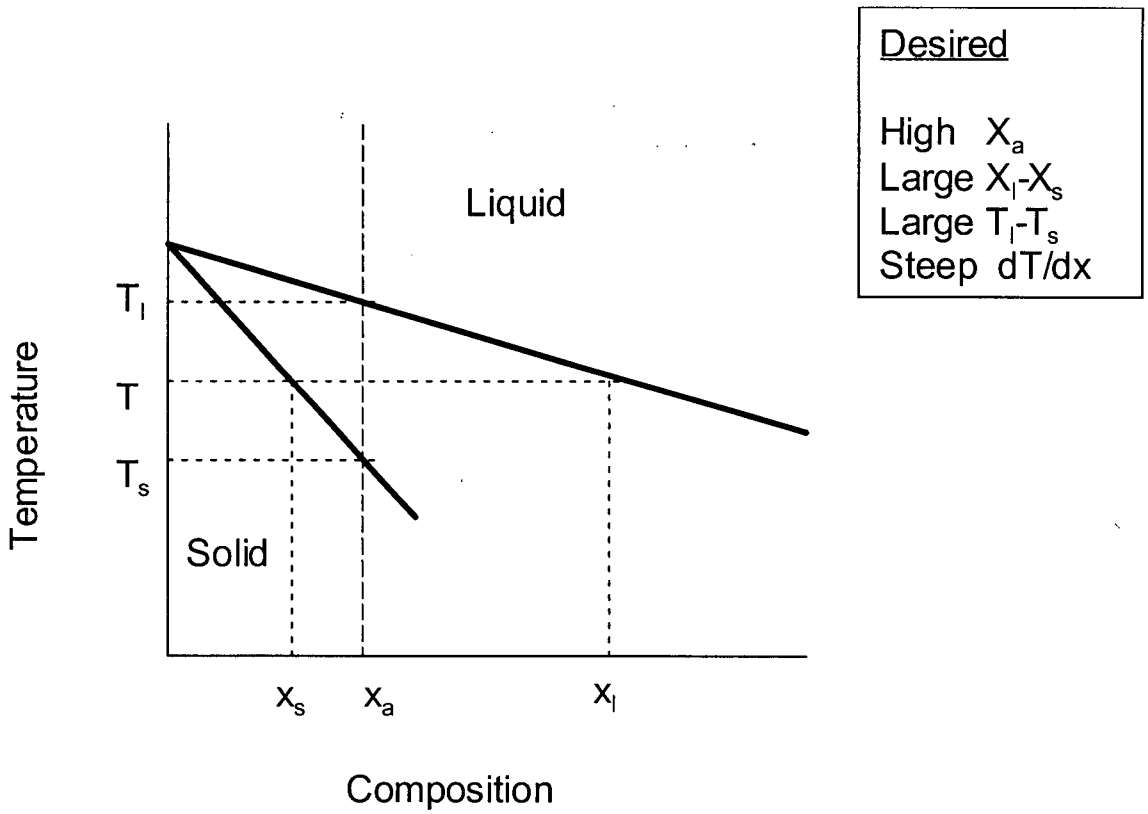

Figure 2.10 Schematic phase diagram showing key parameters for SLPS (Wright, 1992)

(2) A large separation X_l-X_s between liquid and solid composition is desirable to minimize sensitivity to compositional fluctuations, but only to a limit. Compositional similarity provides superior wetting properties.

(3) Steep liquidus and solidus lines, also for process control considerations, so that the volume of liquid does not fluctuate with small variations in temperature.

Some of the alloys systems that have been successfully sintered by SLPS include iron-carbon (Cambal and Lund, 1972), copper-nickel (Bala and Lund, 1979), cobalt-base alloys (Guyard et al., 1981) and tungsten-base alloys (Wright et al., 1995). However, the widest commercial success of supersolidus sintering has been in production of high-speed tool steels with high alloy contents (Cr, Mo, W, V). Reports in the literature of sintering this type of steel are numerous ie. Podob et al. (1981), Takajo et al. (1986), Wright et al. (1992) and Myers et al. (1998). A major limitation, however, in understanding the science behind sintering of tool steels, is the absence of phase diagrams for these complex alloy systems.

2.3.2 Densification

Densification theory for SLPS is a topic that has been covered extensively only in recent years almost exclusively by German and coworkers (Liu, Myers, Lal) in several papers (1995, 1997, 1999, 2000). Along with a phenomenological description of the process, a model has been developed that agrees quite well with experimental results.

As the compact is heated up, normal solid state sintering takes place and is characterized by neck growth between powder particles. The degree of solid sintering is generally less than in most solid state sintering systems because the large SLPS powder size decreases the solid sintering driving pressure. As the solidus temperature is approached, liquid begins to nucleate heterogeneously at the sites that were the last to solidify during atomization of the prealloyed powder. These sites are typically grain boundaries, interparticle necks and interdendrite spaces within the particles that have a locally greater solute concentration than the rest of the material and thus a lower melting temperature than that predicted by the phase diagram. However, once liquid is formed,

and once the solidus temperature is reached, the microstructure tends toward the equilibrium solid-liquid ratio through necessary time-dependent changes in the amount and composition of the liquid, aided by the high diffusivity in the liquid phase. The mass fractions of liquid and solid can be calculated from the phase diagram.

Once the liquid forms, it rapidly forms a continuous film that penetrates the grain boundaries. Eventually, grain boundaries at the interparticle bonds formed during solid-state sintering are also attacked. The grain boundaries are completely wetted when the dihedral angle becomes 0^{o} (German, 1990), and eventually liquid flows to the particle surfaces, forming pendular bonds with other particles. The liquid can then exert a strong capillary force, placing the microstructure under a large stress σ, defined by German as

$$\sigma = \frac{5.2\gamma_{lv}\cos\theta}{R\left(\frac{\Delta L}{L_o}\right)} \tag{2.8}$$

where all symbols have their previous connotations. The wetting angle θ is assumed to be 0^{o}. The capillary force is isotropically oriented.

Immediately following liquid formation and spreading, the capillary forces induce massive rearrangement, densification and contact flattening within the compact. Densification begins when fractional coverage of the grain boundaries by liquid reaches a critical value, near 0.73. The semi-solid particles turn mushy and flow as a viscous, thixotropic system. The expression for the viscosity of such a system is complex and was determined by German (1990) using a modified model from the literature on rheocasting. The apparent viscosity η of the solid-liquid mixture present during sintering can be given by

$$\eta = \eta_0\left[1-(\Phi/\Phi_m)\right]^{-2} \tag{2.9}$$

where η_o is a combination of factors including strain rate sensitivity and numerical constants, Φ is the solid-liquid ratio, and Φ_m is the critical ratio above which the system exhibits infinite viscosity ie. a rigid structure is achieved.

Using this expression for viscosity, the shrinkage $\Delta L/L_o$ during isothermal sintering can be described by

$$\frac{\Delta L}{L_o} = \frac{\gamma_{lv} t}{R\eta} \tag{2.10}$$

Finally, assuming constant mass and isotropic shrinkage, the shrinkage can be related to the fractional sintered density ρ by

$$\rho = \frac{\rho_g}{\left(1 - \frac{\Delta L}{L_o}\right)^3} \tag{2.11}$$

where ρ_g is the fractional green density. This model corresponds extremely well to results obtained both by German and by other researchers for a wide range of alloy systems. Examples are given in Figure 2.11.

2.4 The Ideal SLPS System

This section will discuss some of the factors that lead to a successful SLPS process, based on a survey of the literature. The material to be sintered should exhibit certain properties, including desirable phase diagram attributes, as presented in section 2.3.1, as well as appropriate green density and powder characteristics. Processing conditions also play a major role.

2.4.1 Powder Characteristics

Pre-alloyed powders produced by water atomization appear to be the most attractive candidates for SLPS. Water atomization is superior to gas atomization as it reduces the risk of entrapping gas inside the particles as spherical pores. In addition, the powders are not only easily processed by this method, but they also exhibit low levels of oxide, and the resultant irregular shape (Beddow, 1978) allows a high strength in the green state after pressing. A broad powder size distribution is desirable, as this increases packing density. Small powders also melt faster and produce more liquid than large particles (Guyard et al., 1981), so their presence increases the temperature range over which SLPS can be practiced. And although powder sizes as large as 500 μm have been sintered to full density, it is recommended (German, 1990) that the average powder size be kept under 80 μm as a practical limit.

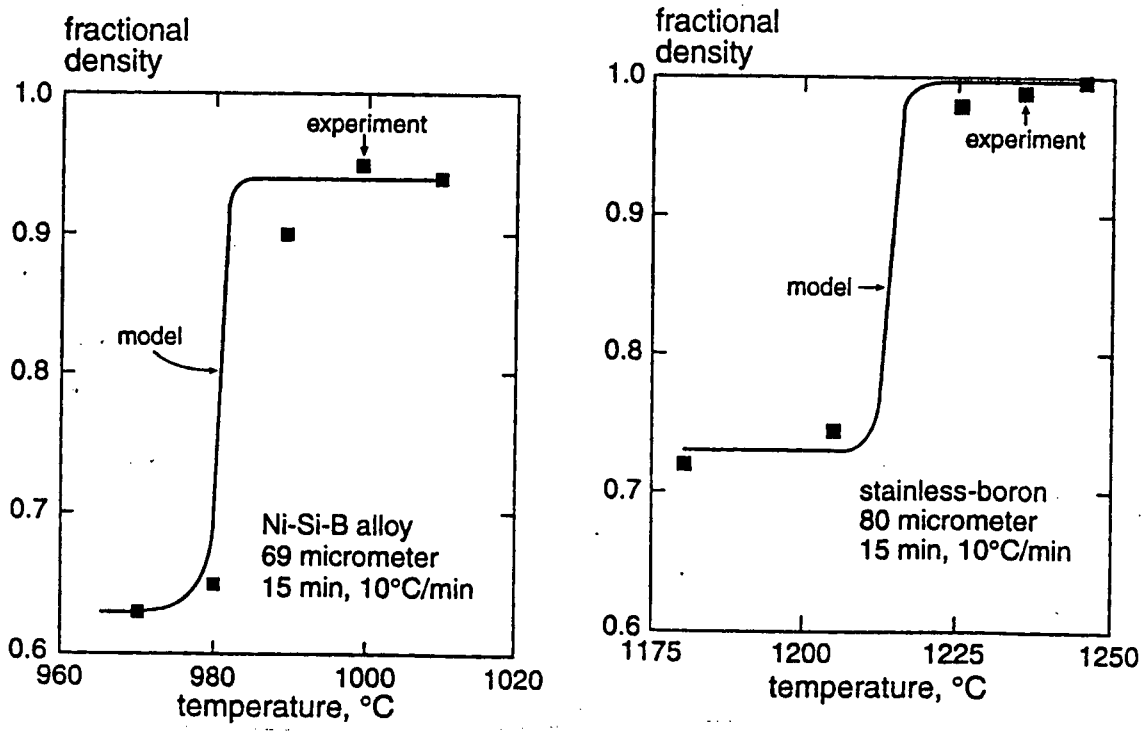

Figure 2.11 Comparison of German's densification model for SLPS with experimental results. Experimental parameters for composition, powder size, hold time and heating rate are shown on the graphs (German, 1990)

2.4.2 Green Density

In general, there has been no reported effect of green density on densification during SLPS processing. In fact, some of the earliest studies (Lund, 1972, 1974) report that full densification was achieved simply by sintering loose, tapped steel powders of 55% theoretical density. Too high a green density is actually undesirable, as in the 90 – 92% green density range there is a transition from open, interconnected porosity to isolated, closed pores in which gas may remain, limiting the final density achievable. This transition is illustrated in Figure 2.12 for a nickel-base superalloy (Westerman, 1962). The first closed pores begin to form at green densities as low as 85%. A high green density will also lessen capillary flow (German, 1990). It is thus desirable to limit the green density to less than 90% theoretical.

One important phenomenon to avoid is that of density gradients present in the green part as an artifact of the pressing process. While density gradients in the green part will not necessarily lead to density gradients in the finished part, they will promote distortion and slumping.

2.4.3 Sintering Conditions, Thermal Cycle and Sinterability

In practice, on entry into the SLPS sintering furnace, a green part experiences an elevation in temperature that corresponds to the furnace heating capabilities. This heating rate is the first element in the sintering cycle. In general, higher heating rates (~10 K/min) are good for SLPS since there is less time for homogenization of compositional gradients to occur (German, 1990). If there are regions of higher solute concentration present, they will melt and allow for densification below the optimal sintering temperature, accelerating the process. However, the heating rate must be sufficiently slow to allow all oxides to reduce before liquid formation. As mentioned, oxides significantly alter the good wetting and spreading characteristics needed for densification. In addition, oxides that remain during the sintering process may react with carbon in the alloy to form CO bubbles that result in large pores in the finished product (Vollertson, 1991). Sometimes a hold step at a temperature that is sufficiently high, yet below the solidus is introduced to the sintering cycle in order to ensure reduction of all surface oxides.

The sintering and heating process may take place in a number of atmospheres. Vacuum sintering avoids the phenomenon of entrapped gases during the final densification stages, but is in most cases prohibitively expensive. SLPS typically takes place in a hydrogen atmosphere.

Once the maximum temperature is reached, parts are typically held between 10 to 60 minutes. In most cases densification occurs quite quickly, and prolonged holds are not beneficial, as pores can agglomerate, and excessive grain growth may ensue at the high temperature. It has also recently been reported (Liu et al., 2000) that when distortion occurs, it occurs as a separate event following densification, so prolonged holds may also promote slumping. The sintering temperature must be carefully selected to provide optimum densification but avoid distortion, as was illustrated earlier in Figure 2.9, and is usually located within a narrow window. This sintering window defines the particular "sinterability" for a specific alloy.

Most alloys that are sintered by SLPS exhibit the generic isochronal sintering curve shown in Figure 2.13, produced by holding samples at different sintering temperatures for the same length of time (Wright et al., 1999). Densification begins to occur T_{OS}, a temperature just following liquid formation, and continues to increase with increasing temperature until T_m, the temperature at which maximum density is obtained. The sintering window is described by the temperature range between T_m, and T_d, the temperature at which the compact distorts due to excess liquid, and over all temperatures in this range the alloy achieves acceptable densities and microstructures. Ideally, the length of this sintering plateau is between 20-30K (German, 1990), in which case the alloy is said to have good sinterability. This window is related to the composition of the alloy; as indicated in section 2.3.1, choice of an alloy with low sensitivity to temperature as indicated by the phase diagram will be easier to sinter in terms of process control.

After SLPS, cooling back to room temperature must take place. Slow cooling is a more expensive option, but attractive from a microstructural viewpoint, since the grain boundary liquid films present during sintering will decompose as equilibrium dictates, promoting a homogeneous structure. Fast cooling introduces the risk of solidification pores (German, 1990). In general the chosen cooling rate must take into account the microstructure and properties anticipated for the final product.

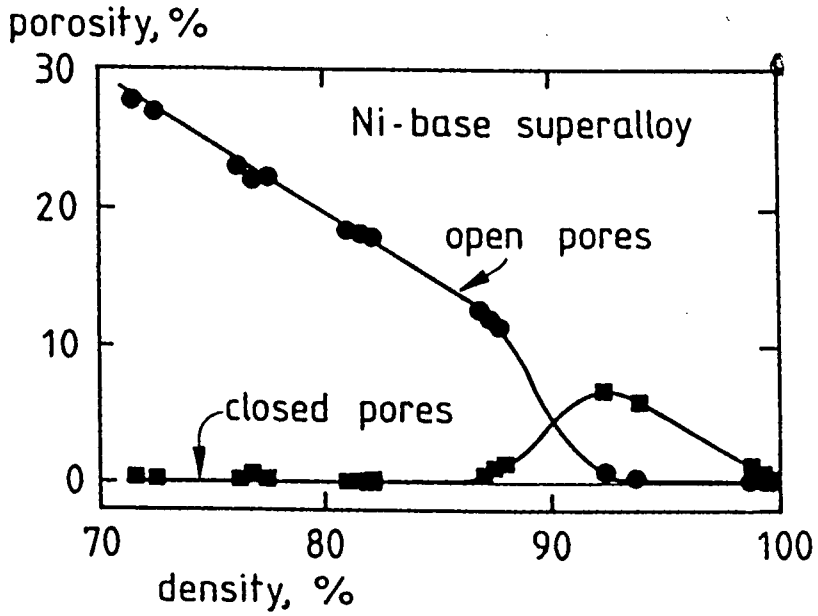

Figure 2.12 Pore structure evolution during supersolidus liquid phase sintering of a Ni-base superalloy (Westerman, 1962).

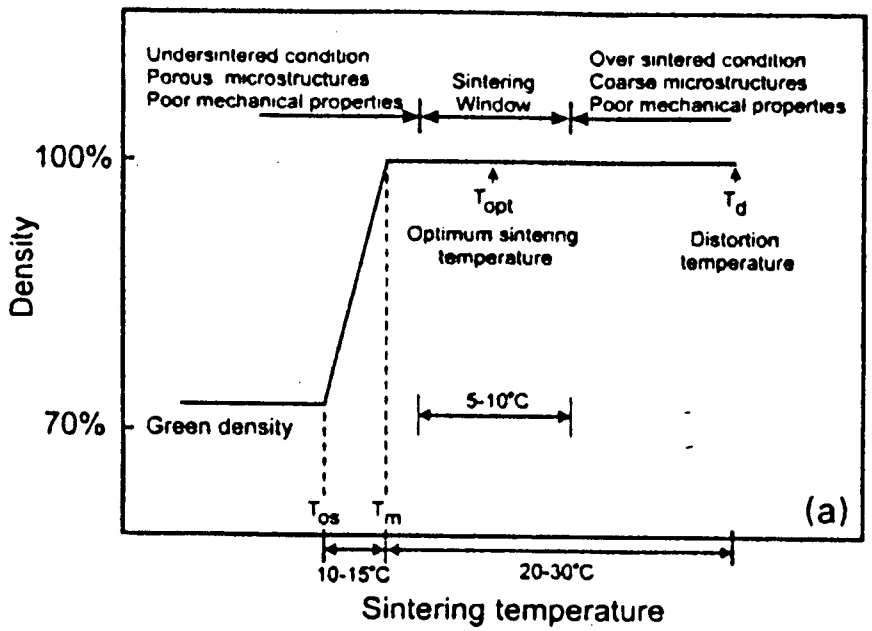

Figure 2.13 Classic sintering curve defining the inherent "sinterability" of an alloy (Wright et al, 1997)

2.5 Summary

In general it appears that there is a solid knowledge foundation on which to base further study of supersolidus liquid phase sintering. The process is a consequence of the driving pressure to eliminate high-energy interfaces within the P/M compact, and it proceeds by means of capillary-driven viscous flow of a semi-solid system at temperatures above the solidus. The resultant densification is rapid, and has been modeled successfully for numerous alloy systems. However, the densification is exceptionally sensitive to processing parameters, and successful sintering without distortion is dependent on the sintering window, which is inextricably linked to the alloy composition, and thus the phase diagram.

This suggests that the first undertaking in the application of SLPS to a specific alloy should be a determination of the densification behaviour as a function of time and temperature, and thus construction of the characteristic sintering curve of the alloy. An accurate phase diagram is also essential for both experimental design as well as analysis of the results.

Chapter 3: Experimental Methods

This chapter provides information on the metal powders used, sample preparation, experimental procedures and material characterization techniques used in the study of supersolidus sintering of steel powders.

3.1 Metal Powders and Sample Preparation

All samples used in the study were prepared from a base metal powder produced by powder metal supplier Hoeganaes Corporation under the trade name Ancorsteel 85 HP, hereafter referred to as 85 HP. This powder is produced by the process of atomization, which is the dispersion of molten metal into droplets by a rapidly moving stream of gas or liquid; subsequently the droplets solidify in the cooler atmosphere. Specifically, 85 HP is produced by water atomization of an iron molybdenum alloy, resulting in polycrystalline powder particles of average composition Fe-0.85 wt % Mo, with trace amounts of unavoidable impurities such as manganese, carbon and oxygen. This type of powder is termed "pre-alloyed" since the desired composition is achieved by alloying the melt before atomization, rather than mixing two elemental powders. The composition of 85 HP is given in Table 3.2 and the rough particle size distribution is given in Table 3.3.

Table 3.1 Typical composition (wt%) of Ancorsteel 85 HP

C	Mn	Mo	O	Fe
<0.01	0.12	0.86	0.08	Balance

Table 3.2 Sieve distribution of Ancorsteel 85 HP powder

Particle Size (μm)	>250	150-249.9	45-149.9	>45
U.S. Standard Mesh	(+60)	(-60 +100)	(-100 / +325)	(-325)
Weight %	Trace	10	70	20

After atomization, the 85 HP powder is blended with other additives for a variety of purposes. Spherical graphite particles, 10 microns in size and produced by Timcal, are

added to achieve the final desired carbon content of the powder. Modified ethylene bi-stearamide (EBS) sold under the trade name Acrawax is added as a lubricant to reduce friction between powder particles and also between the powder and the walls of the die during subsequent pressing, increasing flowability and compressibility. Finally, a polymeric binder, PVB, is also blended with the powder. This binder may act as an additional lubricant, but is also a cementing agent to improve the green strength of the compact after pressing. The resultant blend has an apparent density (density of powder in a loose state without agitation) of 3.10 g/cm^3 and its final composition is given in Table 3.3. Both binder and lubricant are later removed prior to sintering.

Table 3.3 Final composition (wt %) of experimental powder Blend A

85 HP	Graphite	Acrawax	Binder
97.45	1.35	0.60	0.60

The powder blend shown in Table 3.3 is the blend that was used for the majority of the experiments performed at the University of British Columbia and in this dissertation will be called Blend A. However, a limited number of tests were conducted on a proprietary powder, to be called Blend B. The only significant difference between the blends was the addition of a small amount of a proprietary alloying element to Blend B, comprising 0.4 wt% of the powder blend. The function of this addition relates primarily to the heat treatment process following sintering. After it was established that this alloying addition has little or no effect on the sintering process, Blend A was established as the primary experimental material. Figure 3.1 shows a scanning electron micrograph of Powder Blend A. To all intents and purposes blends A and B share essentially the same morphology and both exhibit irregularly shaped particles, consistent with production by water atomization.

Experimental specimens were produced from powder blends A and B using a single-acting hydraulic press and die at Stackpole Ltd. Compaction pressures on the order of 600 MPa were used in order to yield specimens with green densities of approximately 7.0 g/cm^3, or 90% of theoretical density. During compaction, green density was monitored using Metal Powder Industries Federation (MPIF) Test Method 42

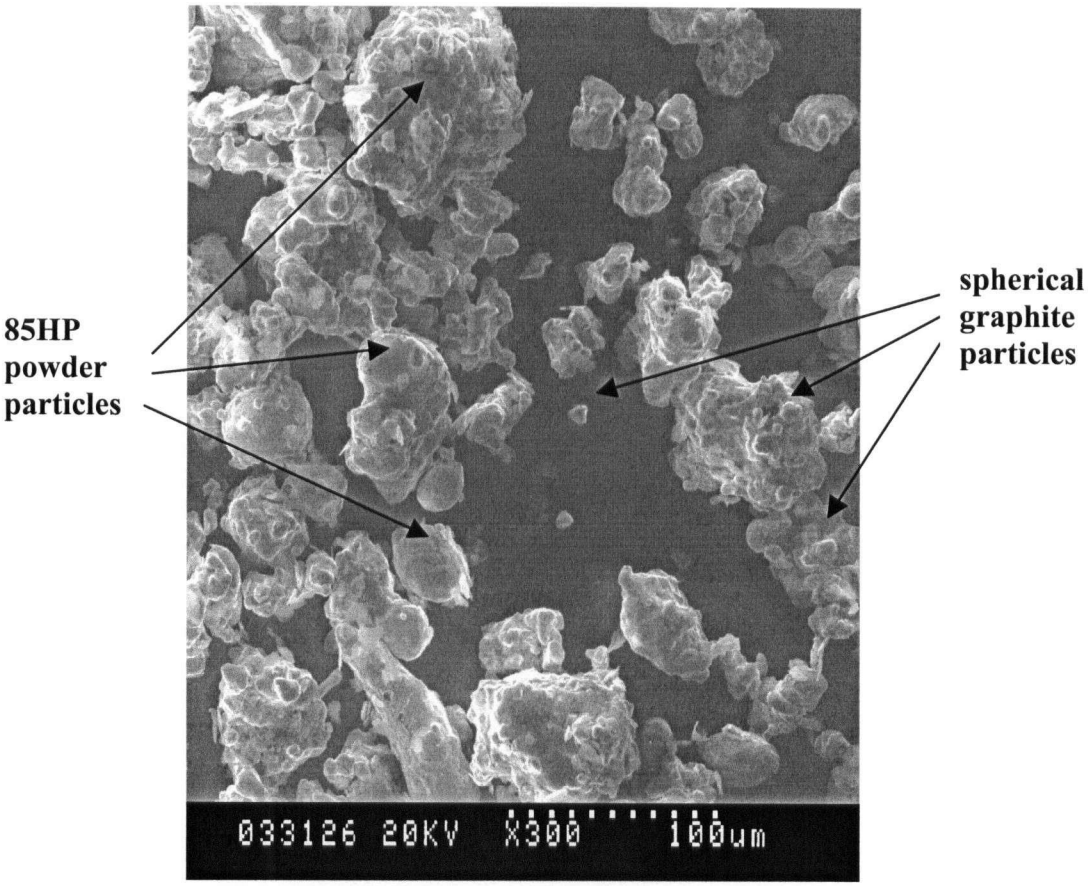

Figure 3.1 SEM Micrograph (300x) of Powder Blend A

(i.e. the Archimedes Principle). Details of density determination by hydrostatic weighing may be found in Bowman et al. (1967). All of the specimens used were cylindrical with diameters of either 5 or 6 mm, while lengths ranged from 6 to 12 mm.

3.2 High Temperature Experimental Furnace

3.2.1 Description

With a view to performing sintering experiments at elevated temperatures, a high temperature experimental vertical tube furnace was modified at UBC. The resultant apparatus is shown schematically in Figure 3.2. An Omega CN9000A controller and shielded platinum type S thermocouple provided temperature control of two molybdenum disilicide heating elements capable of temperatures in excess of 1400°C. The tube in which the samples were heated was situated between the two heating elements, and temperatures inside the tube were monitored by another shielded type S thermocouple attached to a cold junction compensator and chart recorder. It was determined that the accuracy of the thermoouple was +/- 5°C, ie. a range of 10°C. Water-cooled gas inlets and outlets were located at the bottom and top of the alumina tube respectively, and a valve at the bottom of the tube allowed material to be dropped from the interior of the furnace into a quenching medium if desired. Omega flowmeters were used to regulate the flow of gas into the furnace, and were calibrated using standard bubble tests and calibration charts from the manufacturer.

After modification, the temperature profile of the furnace at a high temperature setpoint (1290°C) was measured in order to determine the location of the "hot-zone". This profile is shown in Figure 3.3. In this profile temperature measurements were initiated just below the water-cooling coils at the top of the furnace and mapped the temperature increase with depth into the furnace. The profile revealed a constant temperature hot zone of approximately 100 mm in length. During all experiments, samples were kept in this zone to minimize temperature gradients that could produce inhomogeneities during the sintering process.

3.2.2 Experimental Procedure

All trials in the high temperature furnace were executed with the same procedure. The furnace was brought to the specified experimental temperature and flushed with

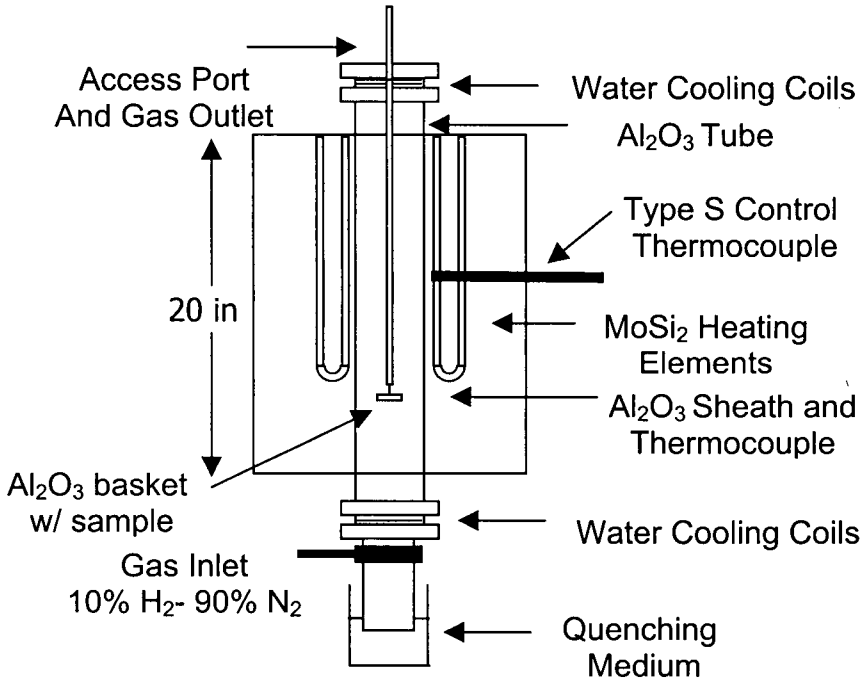

Figure 3.2 Schematic of High Temperature Experimental Furnace

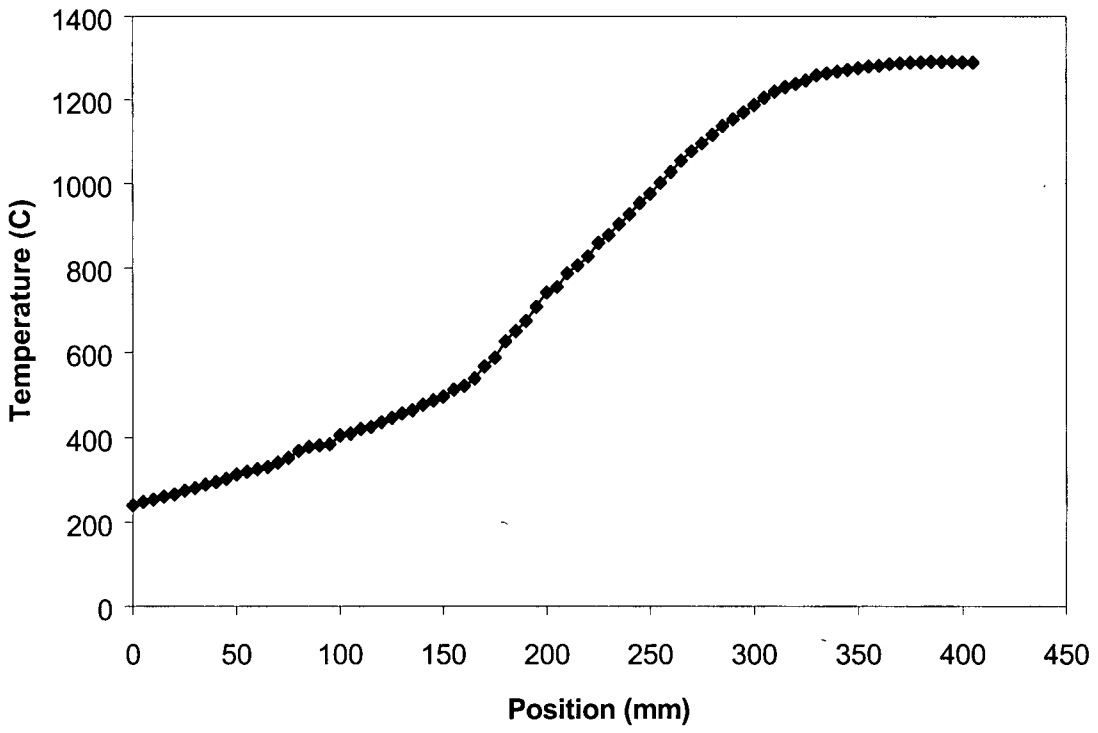

Figure 3.3 Temperature profile of experimental furnace at 1290°C setpoint

nitrogen to remove residual oxygen. Following this, 2.5 l/min flow of a 10% hydrogen – 90% nitrogen (by volume) premixed gas was initiated through the furnace, and continued throughout the experiment. The H_2-N_2 furnace mixture is standard in the powder metallurgy industry, and provides a reducing atmosphere to extract oxygen from the powder samples, prevent further oxidation, and aid the delubrication and debinding processes.

Sample dimensions were measured with Mitutoyo digital calipers, and mass was determined with a Mettler AE240 electronic balance in order to calculate the green density of the sample. Density was measured by this method as opposed to the Archimedes method in order to prevent degradation of the porous sample by measurement in water. Samples were then placed in a high purity alumina crucible. Alumina and platinum, both chemically inert in the presence of a liquid/solid steel mixture, were both considered as crucible materials. However, it was discovered that of the two, alumina was the only surface that was non-wetting to the partially liquid sample and was subsequently employed. The sample-containing crucible was then suspended by a wire hook from the end of the shielded alumina thermocouple. A mechanized table was used to lower the sample and thermocouple into the furnace at a constant rate. Care was taken to ensure that the sample was placed into the constant temperature hot zone of the furnace, particularly so that there was no discrepancy between the temperature of the sample and the thermocouple reading. Samples were then kept at temperature for the prescribed length of time, then removed from the hot zone and cooled in one of two ways:

1) Quenched in water at 25°C – these experiments were performed in order to preserve the microstructures present at a specific point in the sintering process. In order to achieve this, a valve at the bottom of the furnace was opened, and the crucible containing the sample was released from the end of the shielded thermocouple and allowed to fall into the quenching medium (water).

2) Rapidly cooled (cooling rates in excess of 200°C/min) under atmosphere – these experiments were performed in order to prevent oxidation of the sample surface and allow for accurate density

measurements. This was achieved by raising the sample into a cooler zone of the furnace and continuing the flow of the H_2-N_2 gas mixture.

Relevant experimental details of the heat treatments (temperature and time) for each test are described where appropriate with the experimental results (Chapter 4). Immediately following each experiment, the samples were dried (if quenched), weighed, and measured to calculate the final density. In the case that a sample underwent distortion during the heat treatment, the standard Archimedes technique (MPIF Test 42) was employed to determine the final density. There were no significant differences between results obtained by the two different density measurement techniques. The Archimedes technique involves the measurement of the weight of the sample in both air (w_a) and water (w_w), and then calculating the density of the sample, ρ_s, according to

$$\rho_s = \frac{\rho_w w_a - \rho_a w_w}{w_a - w_w} \tag{3.1}$$

where ρ_w is the density of water (g/cm^3) as a function of temperature T (^{o}C), according to

$$\rho_w = 1.0017 - 0.0002315T \tag{3.2}$$

and ρ_a is the density of air. The value of ρ_a is generally assumed to be negligible, and thus equation 3.1 reduces to

$$\rho_s = \frac{\rho_w w_a}{w_a - w_w} \tag{3.3}$$

3.3 Differential Scanning Calorimetry (DSC) Experiments

3.3.1 Technique and Objectives

Differential Scanning Calorimetry (DSC) experiments were performed on both powder blends A and B at the University of Waterloo in order to characterize the thermal events occurring during the sintering process. DSC is a powerful experimental technique that provides quantitative data on thermal events occurring as a sample is subjected to a specific thermal schedule (heating, cooling, isothermal holds etc). The DSC apparatus applies the specified thermal schedule to two crucibles; an empty one, and one containing the sample, and then measures the difference in heat flow between the two. Each thermal event (ie. phase transformation, chemical reaction etc.) is recorded as a peak on a graph of heat flow as a function of time during an applied heat treatment, and thus indicates the

temperature that the event occurred at. Integration of these peaks yields the energy associated with the event. For a more complete reference on the theory of DSC, the reader is referred to the monograph on calorimetry by Hemminger (1984).

In total, 15 DSC experiments were performed. The first sample set consisted of 8 experiments performed on specimens made of Blend B. In general the experiments were designed to examine the effects of heating rate and presence of lubricant on the thermal events occurring, as well as incorporating tests for reproducibility. The second sample set consisted of 7 tests performed on specimens produced from Blend A. In this case, experiments were designed to deduce differences in the behaviour of the two blends under the same experimental conditions and provide a characterization of Blend A as had been done for Blend B in the first sample set. Complete experimental details for the individual tests are presented with the results in Chapter 4.

3.3.2 Experimental Apparatus and Procedure

All experiments were performed in a Netzsch 404C High Temperature Differential Scanning Calorimeter at the University of Waterloo, and data was collected and analyzed with a desktop computer running Netzsch Thermal Analysis software. The apparatus is capable of heating rates from 0.1 to 50 K/min, and can achieve temperatures of up to 1500°C. A photo of the apparatus is provided in Figure 3.4.

The powder samples tested, both blend A and blend B, consisted of 5 mm diameter cylindrical specimens, all cold pressed to a green density of approximately 7.0 g/cm^3 as described in section 3.1. These specimens were then cut to a height of approximately 3 mm with an alumina saw. Several samples underwent a heat treatment at UBC prior to DSC testing in order to remove the binder and lubricant. These samples were soaked at 800°C for 10 minutes in a $10\%H_2 - 90\%N_2$ atmosphere, then cooled to room temperature under atmosphere. All samples were weighed before testing, placed in high purity alumina crucibles with lids (height 3.7 mm, diameter 5.5 mm), and placed in the DSC furnace.

Once the crucibles were inside the DSC furnace, it was closed and evacuated twice to minimize the presence of oxygen in the system. It was then backfilled with 5% H_2–$95\%N_2$ gas and measurements were initiated. All samples were heated from, and cooled to room temperature.

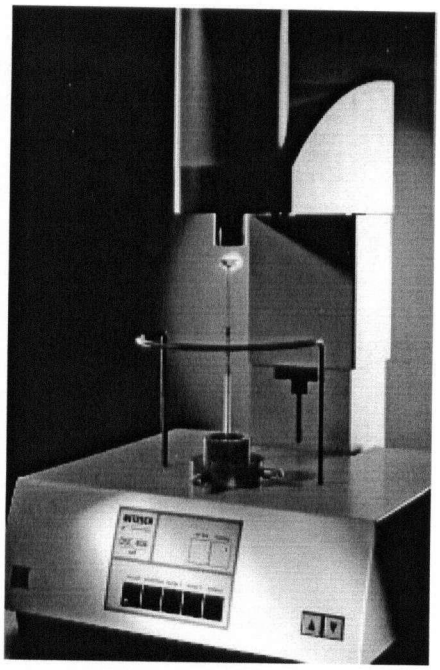

Figure 3.4 Netzsch 404C Differential Scanning Calorimeter

During measurement, temperature and mass corrected heat flow data were collected at 0.66 Hz. The error associated with specific measurements is discussed where appropriate with the presentation of experimental results. In each case, measured data was combined with data from a specific correction file for each run that had been generated prior to each test by operating the DSC with two empty crucibles under identical experimental conditions.

After each DSC experiment, quantitative data regarding onset temperatures, location of peaks and peak energies were calculated with the Netzch Thermal Analysis software. Onset temperatures are calculated by taking the intersection point of the extrapolated baseline with an extrapolation of the slope of the peak. Peak locations are simply the maximum value for a particular segment of curve and finally, peak energies are calculated by the software based on the integration of a segment of curve selected by the user. Unfortunately this introduces the possibility for error in energy values based on the length of curve selected for integration, but an attempt was made to reduce this margin by consistently selecting the limits at points where the slope of the baseline was zero, both prior to and after the occurrence of the peak. The error in energy values was estimated to be approximately +/-10 J/g.

3.4 Inspection Techniques

3.4.1 Mounting, Polishing and Etching

A standard procedure for metallographic preparation of the porous sintered specimens was observed. Samples were mounted in cold cure epoxy resin, then progressively ground with SiC abrasive grit paper with water as a lubricant from 80 to 600 grit. They were then polished using 6 and 1 micron diamond paste, followed in some cases by a final polishing step with 0.05 colloidal SiO_2 solution. Ultrasonic vibration was performed in between each grinding and polishing step to minimize the occurrence of "lidding", i.e. residual material filling pores and masking the true porosity levels. Samples were then chemically etched in 2% Nital solution by cotton swabbing for 5-25 seconds.

3.4.2 Microscopy and Image Analysis

Optical microscopy for observation of microstructures was performed on all specimens using a Nikon Epiphot 300 Microscope. Image analysis by area measurement

was performed for quantitative determination of two-dimensional porosity using C-imaging LC software and a Leitz Optical Microscope. Finally, scanning electron microscopy (SEM) and chemical analysis (EDX) was performed on powders and sintered samples using the capabilities of the Electron Microscopy Laboratory in the Metals and Materials Engineering Department at UBC, including both Hitachi H-3800 and H-570 electron microscopes.

Chapter 4: Experimental Results

This chapter presents the results obtained from all experimental work performed in this study. The first section introduces the results of the differential scanning calorimetry (DSC) work, the second section shows results from the furnace experiments performed to investigate density evolution, and the third presents the results of the microscopy and image analysis.

4.1 DSC Results

In this study, DSC work was undertaken in order to achieve several objectives that may be encompassed by a general characterization of the reactions that occur in the powder during the heating cycle. Specifically, experiments were designed and conducted with a view to determine the following phenomena in the powder system:

1) Temperature range of delubrication and debinding events
2) Temperature of the $\alpha \rightarrow \gamma$ phase transformation on heating
3) Solidus and liquidus temperatures
4) Temperature of the $\gamma \rightarrow \alpha$ phase transformation on cooling
5) Effect of heating rates on the above events

The first sample set consisted of 7 experiments performed on specimens made of the base Fe-C-Mo alloy, Blend A. In general the experimental program was designed to obtain the information listed, while incorporating tests for reproducibility. The second sample set consisted of 8 tests performed on specimens produced from Blend B, the proprietary industrial alloy. In this case, experiments were designed to deduce differences in the behaviour of the two blends under the same experimental conditions, and also to characterize Blend B. The results of the DSC tests include heat flow traces as a function of time and temperature. Micrographs taken of the samples on completion of the experiments are presented later in section 4.3.6. In total, 15 DSC experiments were performed.

Figure 4.1 shows the DSC curve as a function of temperature for Blend A sample 1, which was heated at 30°C/min to 1460°C and then cooled to room temperature at 30°C/min. All of the DSC curves obtained share some similarities and this curve will be discussed in detail to provide an example of how to interpret the data. The negative heat flow portion of the curve indicates the heat evolution on heating, while the positive heat flow portion shows the heat evolution upon cooling. As a temporal progression the graph can be read from bottom left to bottom right, upwards, and then from top right to top left.

On the commencement of heating, it can be seen on the DSC trace that the sample absorbs a specific amount of heat before reaching a constant heat flow value. This constant heat flow value is termed the baseline, and it should have the same absolute value on both heating and cooling, i.e., the amount of heat absorbed during heating should equal the heat released on cooling. Any departure from the baseline indicates a thermal event occurring in the sample, the first of which is the endothermic peak for the $\alpha \rightarrow \gamma$ phase transformation occurring between 700 and 900 °C for this sample. The next significant event is the onset of the endothermic melting peak. On cooling, the first significant event is solidification, followed by the $\gamma \rightarrow \alpha$ phase transformation beginning between 600 and 500 °C.

In the following sections (4.1.1-4.1.2), DSC results will be given for the Blend A samples (1-6) made of the simpler Fe-C-Mo alloy, and the results for the proprietary Blend B samples (7-13) will be presented in sections 4.1.3-4.1.4. For reference purposes, Table 4.1 summarizes the experimental conditions for each test.

Where appropriate, tests with similar heat treatments are plotted on the same graph for the purpose of comparison. Relevant quantitative data regarding onset temperatures, location of peaks, and peak energies, calculated with the Netzsch Thermal Analysis software will also be presented. In addition, this information will be tabled for reference in Table 4.2.

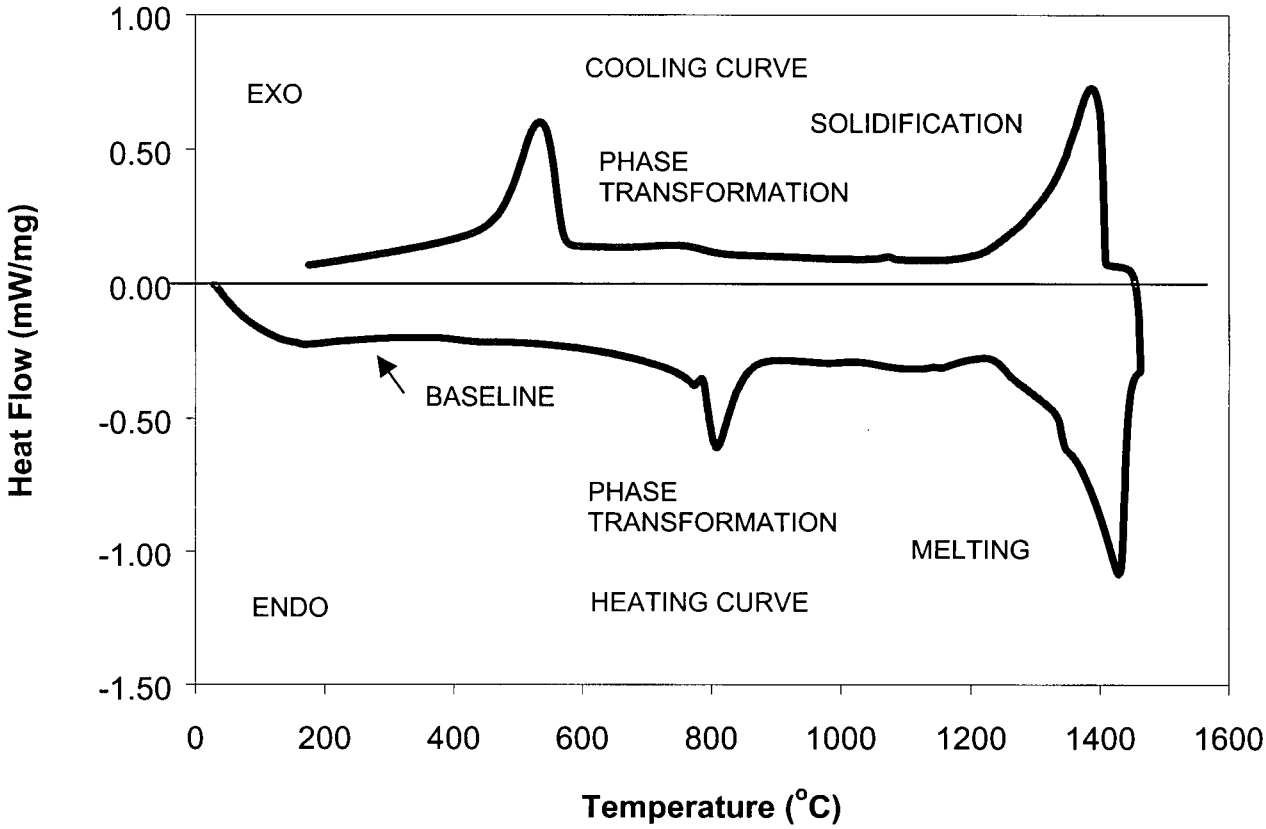

Figure 4.1 DSC trace vs. temperature for DSC experiment 1, heated to full melting at 1460°C

Table 4.1 Experimental conditions for each DSC test

Test #	Blend	Lubri-cant	Heating Rate (°C/min)	Maximum Temp (°C)	Isothermal Hold	Cooling Rate (°C/min)
1	A	Yes	30	1460	No	30
2	A	Yes	30	1460	No	30
2 a)	A	No	30	1460	No	30
3	A	Yes	10	1290	20 min	20
4	A	Yes	20	1410	No	20
5	A	Yes	30	1290	60 min	20
6	A	Yes	20	1410	No	20
7	B	No	20	1410	No	20
7 a)	B	No	20	1410	No	20
8	B	Yes	20	1410	No	20
9	B	Yes	30	1460	No	30
10	B	No	10	1290	20 min	20
11	B	Yes	10	1290	20 min	20
12	B	Yes	10	1290	20 min	20
13	B	No	45	1460	No	30

4.1.1 DSC Results for Blend A Samples – Full Melting

Figure 4.2 shows the traces for DSC tests 1, 2 and 2a). (Sample 2 was reheated during test 2a). All samples were heated at 30°C/min to 1460°C and cooled at 30°C/min. The maximum temperature of 1460°C was chosen as it was assumed to be above the liquidus and the samples would fully melt, thus determining the solidus and liquidus for the alloy. One immediate observation from Figure 4.2 is the good reproducibility of the traces for three tests with identical heat treatments.

The first event observed in all three cases is the solid-state $\alpha \rightarrow \gamma$ phase transformation. The onset temperatures, or T_{Ac1}, are calculated to be 741°C for sample 1,

Table 4.2 - Temperatures and energies associated with thermal events for each DSC test

	Phase Transformation on Heating			Melting Event			Solidification Event			Phase Transformation on Cooling		
SAMPLE #	Onset T	Peak T	Energy (J/g)	Onset T	Peak T	Energy (J/g)	Onset T	Peak T	Energy (J/g)	Onset T	Peak T	Energy (J/g)
1	742	808	-20	1218	1428	-115	1407	1385	105	572	533	59
2	751	803	-27	1230	1418	-114	1399	1384	102	570	533	59
2a	736	765	-29	1215	1421	-83	1404	1383	96	571	535	60
3	757	774	-28	1221	-	-	-	-	-	559	514	66
4	749	793	-24	1230	-	-	-	-	-	577	542	55
5	743	831	-22	1235	-	-	-	-	-	554	514	64
6	740	786	-39	1232	-	-	-	-	-	579	546	56
7	740	755	-33	1215	-	-	-	-	-	670	586	79
7a	734	763	-34	1222	-	-	-	-	-	651	572	65
8	756	785	-35	1211	-	-	-	-	-	660	576	57
9	767	796	-36	1206	1411	-189	1405	1373	129	587	509	85
10	734	746	-30	1213	-	-	-	-	-	577	508	54
11	750	768	-33	1206	-	-	-	-	-	577	508	60
12	748	769	-28	1221	-	-	-	-	-	575	504	68
13	750	772	-34	1215	1422	-143	1402	1377	101	556	510	54

* All Temperatures in degrees Celsius

752°C for sample 2, while the peak temperatures are 808 and 803°C for samples 1 and 2 respectively. On reheating sample 2, the transformation onset temperature was 736°C and a peak temperature of 765°C was observed. Since sample 2a) had already undergone a full cycle of heating, melting and cooling, the lower onset and particularly the lower peak transformation temperatures are not surprising. During its previous heat treatment, the sample was able to homogenize both with respect to microstructure and solute distribution; ie. carbon initially present as graphite powder was already dissolved when the onset of the phase transformation occurred. The more homogeneous microstructure present in test 2a) as compared with tests 1 and 2 allowed the phase transformation to proceed more quickly, and to initiate and terminate at a lower temperature.

The next significant feature is the melting peak, whose onset yields the solidus temperature. The mean solidus temperature was determined to be 1227 +/- 5 °C for the Blend A material, and samples were fully melted at the mean liquidus temperature of 1422°C. It is to be noted that due to the differential method used by the DSC to measure heat flow, measured values for onset temperatures, ie. the solidus, are more accurate than finish temperatures. For example, on the upper, cooling portion of the curve, some degree of undercooling from the measured liquidus, 1422°C, was observed before the onset of solidication at 1407°C. Since molten metals do not generally supercool more than 1 or 2 degrees (Chalmers, 1964), the measured liquidus of 1422°C may be too high. It is certain however, that the true liquidus falls somewhere between 1407 and 1422°C. It is observed that solidification is not complete until 1200°C, a temperature well below the solidus observed on heating, again an artifact of the DSC heat flow measurement.

The solid-state $\gamma \rightarrow \alpha$ transformation occurred with good consistency in the three cases, with a slightly lower T_{Ac1} than expected; 572, 570, and 571 °C respectively for samples 1, 2 and 2a), and all transformations had a peak temperature of 533°C. The consistency may be attributed to the similar microstructures all exhibit after full melting and solidification at the same rate of cooling.

4.1.2 DSC Results for Blend A Samples – Partial Melting

Since the liquid phase sintering process occurs under conditions of partial melting, it was of interest to conduct DSC tests under similar conditions. Experiments

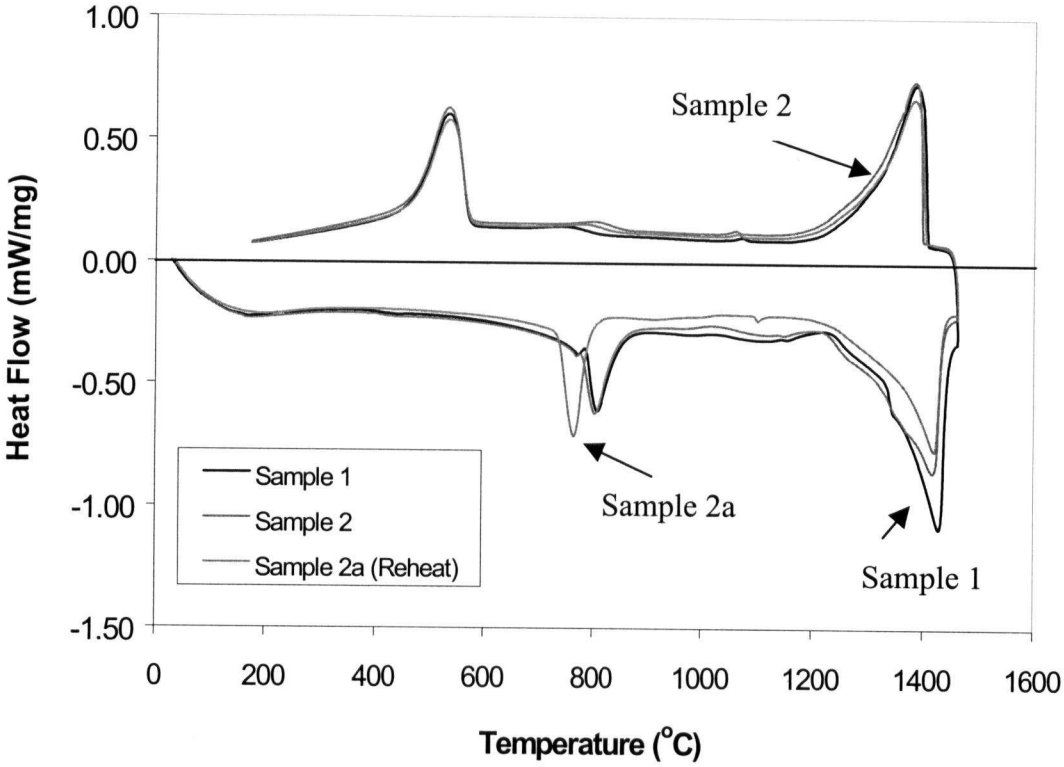

Figure 4.2 DSC trace vs. temperature for DSC experiments 1, 2, and 2a), taken to full melting at 1460°C

with maximum temperatures corresponding to two degrees of partial melting were executed. 1290°C was selected as it is in the temperature range of interest during sintering with a relatively low volume fraction of liquid, and 1410°C was chosen to provide information about the system when a relatively high volume fraction liquid is present.

The amounts of liquid present in the Fe-Mo-C alloy at 1290°C and 1410°C were calculated with Thermocalc™ software (to be discussed in more detail in Section 5.4) and are 16% and 76.5% respectively. Figure 4.3 presents the DSC traces for samples 4 and 6, heated to 1410°C at the same rates of heating and cooling. Again it is observed that there is good reproducibility for the experiments performed under the same heat treatment conditions.

In terms of the solid-state phase transformation behaviour, there are no significant differences between sample 4 and 6, and those taken to full melting shown in Figure 4.2. Samples 4 and 6 show the onset of the $\alpha \rightarrow \gamma$ transformation at 740 and 749°C respectively. The onsets of the $\gamma \rightarrow \alpha$ transformation on cooling were 577°C and 579°C.

The principal difference between Figures 4.2 and 4.3 is that in Figure 4.3, immediately upon cooling, sharp jumps from endothermic to exothermic heat flow are observed in the DSC traces, characteristic of an interrupted melting process and correctly indicating a liquidus temperature greater than 1410°C. This exothermic to endothermic jump is also evident, to a lesser degree, in Figure 4.4 which presents the DSC trace for sample 3, partially melted by heating to 1290°C. A general comparison of the two figures, 4.3 and 4.4 confirms that in this case, the maximum temperature achieved has little effect on the nature of the transformation curve on cooling, except that the peak temperature of transformation observed for sample 3 was 514°C, while the peak temperature for samples 4 and 6 were 542 and 546 °C respectively. While this is not particularly significant for sintering, it may be important for subsequent heat treatments.

4.1.3 DSC Results for Blend B Samples – Full Melting

As seen in Table 4.1, the conditions of the experiments for the proprietary Blend B samples were essentially the same as those for the Blend A samples, with one

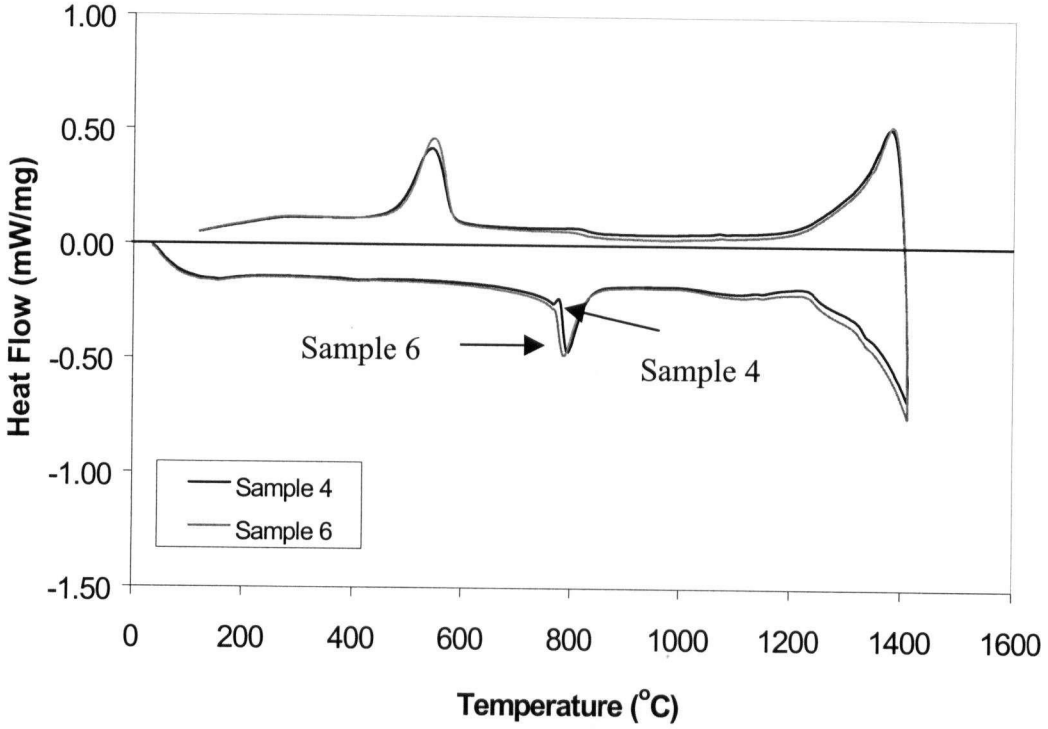

Figure 4.3 DSC trace vs. temperature for DSC experiments 4 and 6, heated to partial melting at 1410°C, with approximate liquid content of 76.5%

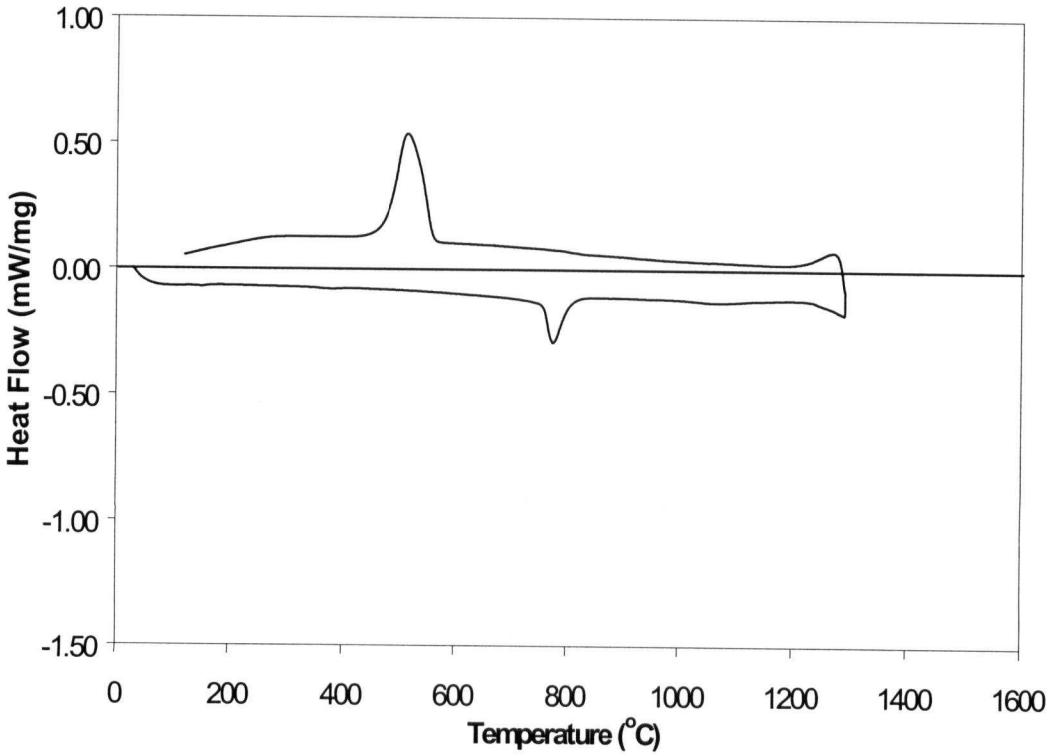

Figure 4.4 DSC trace vs. temperature for DSC experiment 3, heated to partial melting at 1290°C, with approximate liquid content of 16%

exception. Several of the Blend B samples underwent a brief prior heat treatment, as described in Section 3.3.1, in order to extract the polymeric binder and the organic lubricant from the green samples. This was done in order to observe the effects, if any, of the binder and lubricant on subsequent events during the sintering cycle. The legends of the figures will indicate which samples underwent a prior delubrication treatment.

The results of tests 9 and 13 are presented in Figure 4.5. Note that the heat flow scale differs slightly from that used for the Blend A samples. These samples were heated at different rates to 1460°C, a temperature high enough to induce full melting in both samples, and thus determine solidus and liquidus, expected to differ slightly from those observed for Blend A. The variance in heating rate does not appear to have any significant effects. The mean solidus temperature was found to be 1213 +/- 5 °C, and the liquidus for sample 9 was found to be 1412 +/- 5° C. Unfortunately, however, the DSC trace for sample 13 does not exhibit a heat flow plateau between the liquidus and the maximum temperature of 1460°C, making it impossible to determine the liquidus temperature, again due to the nature of measurement in the DSC. In addition, the heats of melting and solidification for this sample are not consistent. Theoretically, the two should be equivalent; however for sample 9 we observe a heat of melting of 143 +/- 5 J/g, while the heat given off during solidification for the same sample was 100 +/- 5 J/g. The problem seems to alleviate however; as the results for samples 9 and 13 on cooling are quite consistent. Again a so-called "undercooling" is observed before the onset of solidification at 1400°C, thus providing the possible temperature range of the liquidus between 1400 and 1412°C. Both samples show a $\gamma \rightarrow \alpha$ phase transformation peak that is similar in terms of onset, peak and energy, and the peak temperatures were 509 and 510 ^{0}C.

One additional feature of note from these two tests is the difference in broadness of the $\alpha \rightarrow \gamma$ transformation peak between sample 13, which had undergone a prior delubrication heat treatment at 800°C and sample 9, which had not. The observation of a sharper peak for the delubricated sample can be attributed not to the presence of the lubricant itself, but rather the effects of the delubrication treatment, which allowed for diffusion and general microstructural homogenization of the sample, similar to the fully remelted sample (2a) in Figure 4.2. The more homogeneous microstructure allowed the

phase transformation to proceed at a lower temperature (a peak of 772°C was observed for sample 13 compared with 796°C for sample 9).

4.1.4 DSC Results for Blend B Samples – Partial Melting

As with the Blend A samples, partial melting experiments were performed at 1410°C and 1290°C on the Blend B samples; however the volume fractions of liquid present in Blend B are obviously different at these temperatures. Thermocalc™ calculations predict that in Blend B, the material is 96.5% liquid at 1410°C, and 22% liquid at 1290°C. Recall that the onset of melting, or solidus was determined to be approximately 1213°C.

Figure 4.6 shows the DSC traces for tests 7, 7a, and 8 on heating to 1410°C. (Sample 1 was reheated during experiment 1a). The exothermic to endothermic jump characteristic of partial melting is again observed. However, in this case it appears that either the composition of the alloy or the high volume of liquid present does affect the phase transformation on cooling, in all of the three experiments. The transformation onset occurred at a much higher average temperature (660°C) than for previous Blend B samples, and in addition, two overlapping transformation curves were observed. Observation of such double peaks in carbon steels is not necessarily unusual (Kreielaart, 1996), and is most likely due to the decomposition of austenite non-simultaneously into two different product phases; pearlite and either ferrite or cementite depending on the carbon content. While the occurrence of the double transformation peak is very interesting, it will require further investigation to clarify, and is not critical to the melting or sintering behaviour of the alloy. It may, however, be of importance to subsequent heat treatment of the material.

It should also be noted that as in Figure 4.5, those samples that underwent a heat treatment (delubrication, prior DSC) exhibit a sharper $\alpha \rightarrow \gamma$ phase transformation peak than those samples that did not. A sharper transformation peak is also observed for the previously delubricated sample in Figure 4.7 for samples 11, 12 and 13, heated and held at 1290°C for 20 minutes. In other respects, these results are unremarkable. On cooling the average $\gamma \rightarrow \alpha$ transformation onset was 576°C.

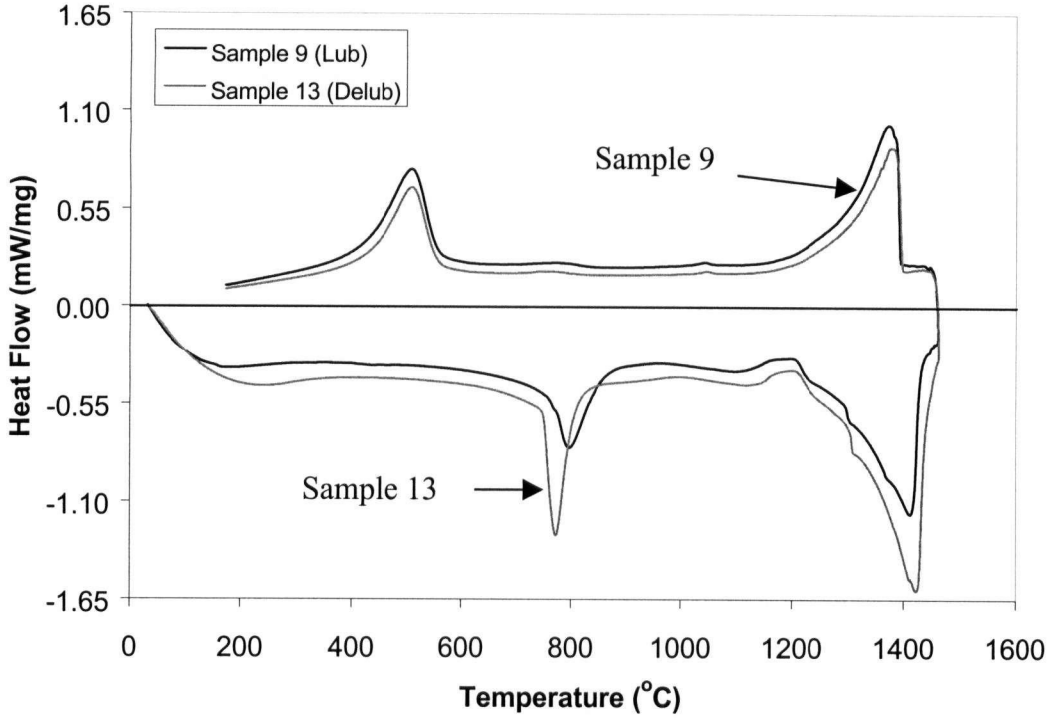

Figure 4.5 DSC trace vs. temperature for DSC experiments 9 and 13, taken to full melting at 1460°C

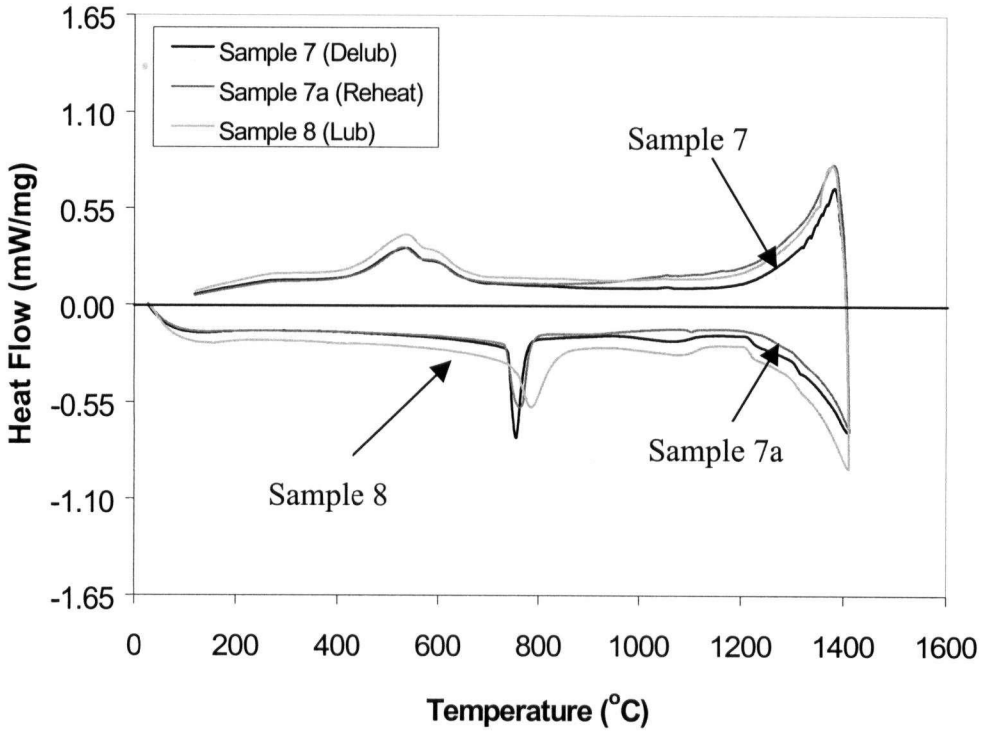

Figure 4.6 DSC trace vs. temperature for DSC experiments 7, 7a) and 8, heated to partial melting at 1410°C, with approximate liquid content of 96.5%

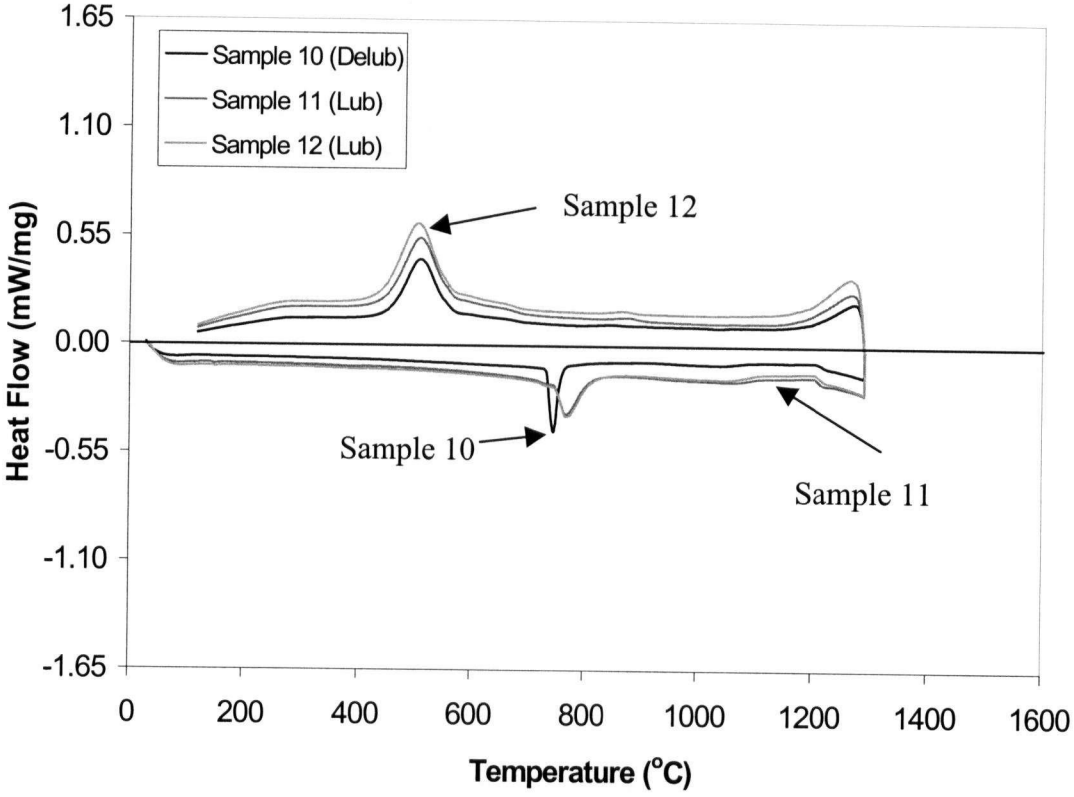

Figure 4.7 DSC trace vs. temperature for DSC experiments 10, 11 and 12, heated to partial melting at 1290°, with approximate liquid content of 22%

4.1.5 Comparison of Blend A and Blend B DSC Results

In general, the results of the Blend A (Fe-C-Mo alloy) samples were extremely similar to those of the Blend B samples. As expected there were small differences in solidus and liquidus temperatures as well as phase transformation behaviour that are ascribed to the compositional difference in the alloys, as Blend B was more highly alloyed than Blend A. Figure 4.8 plots comparatively the DSC traces of samples 1 and 9, one from the Blend A set and one from the Blend B set, that have undergone heating to and full melting at 1460°C. This plot highlights the principal differences and similarities in the behaviour of the two materials:

- Blend A exhibits higher liquidus and solidus temperatures than Blend B
- Both blends exhibits a small degree of undercooling before solidification
- Blend B exhibits a lower $\gamma \rightarrow \alpha$ transformation temperature
- Both blends exhibit sharper $\alpha \rightarrow \gamma$ transformation peaks for samples that underwent prior heat treatment
- Heating rates did not appear influence the behaviour of either blend

Table 4.3 Solidus and Liquidus of Blend A and Blend B Powders

	Blend A	**Blend B**
Solidus Temperature (°C)	1227 +/-5	1213 +/- 5
LiquidusTemperature (°C)	1407-1422	1400-1412

The comparable DSC results for the two powders helps to establish the similarity of their behaviour in a liquid phase sintering process. In particular, the separation between solidus and liquidus temperatures is an important property for supersolidus liquid phase sintering, as discussed in Chapter 2, and is roughly equivalent for the two alloys. However, even the slight differences in solidus and liquidus temperatures could mean that the volume fractions of liquid present could be quite different in the two alloys at the same temperature.

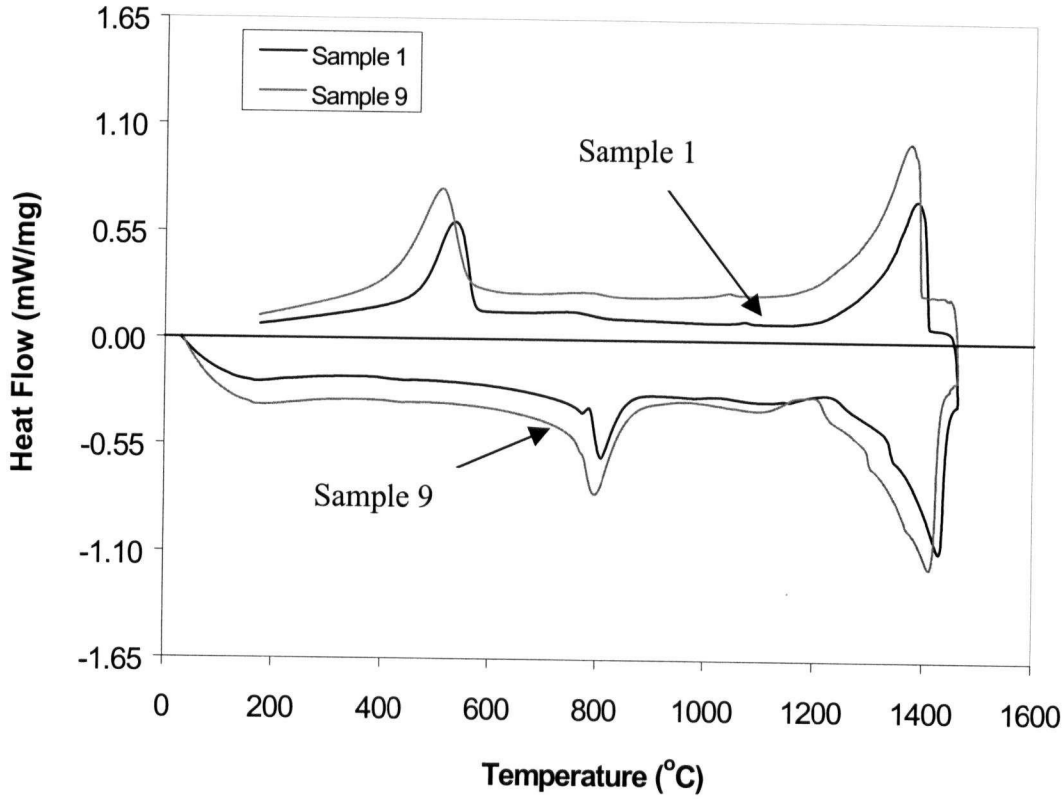

Figure 4.8 DSC trace vs. temperature for DSC experiments 1 and 9, taken to full melting at 1460°C

4.2 Density Evolution – Isochronal Furnace Experiments

All results in this section are for experiments performed on powder Blend A, the ternary Fe-C-Mo alloy. Density evolution is examined with respect to the two major sintering variables, time and temperature. The effects of heating rate are not studied explicitly as heating rates can be translated into an equivalent time at temperature, as was described by Su and Johnson (1996), using the concept of the master sintering curve. According to their theory, which combines the temperature and time variables of the sintering thermal history into one parameter, a series of isothermal runs may provide the same information regarding densification as a series of constant heating rate experiments.

4.2.1 Density and Temperature

The isochronal sintering curve is an important tool for identifying the sinterability of an alloy, as discussed in Chapter 2. To generate these curves, a number of tests are carried out by holding samples with the same initial green density at different temperatures for the same amount of time. Density, or densification parameter P is then plotted as a function of temperature. The densification parameter P may be defined by

$$P = \frac{\rho_f - \rho_i}{\rho_t - \rho_i} \times 100 \tag{4.1}$$

where ρ_f is the density after sintering, ρ_i is the green density, and ρ_t is the theoretical density of the solid alloy (7.80 g/cm^3 for the Fe- 0.85%Mo- 1.5%C alloy). The parameter P is useful as it plots relative densification, taking into account small differences in the starting green densities. In this study the high starting green density of the samples (~90%) means that the (0-100) scale of densification parameter occurs over a small range of densities (90-100%). It is to be noted then, that a densification parameter of 50 corresponds to about 95% theoretical density, a parameter of 80 to about 98% and so on.

Three series of isochronal tests were carried out on powder Blend A, using holding times of 15 minutes, 30 minutes and 60 minutes, and holding temperatures ranging from 840°C to 1300°C. Sintering temperatures above 1295°C produced distorted, blistered samples, precluding accurate density measurement, and thus are not included in the results.

Figure 4.9 shows the sintering curve for samples held at temperature for 15 minutes. A densification plateau is observed at the low temperatures where solid-state atomic diffusion activity is low and no liquid is present. (Recall that the onset of melting in Blend A occurs at approximately 1227°C). Some densification begins to occur at temperatures above 1200°C, but even at 1290°C the maximum densification parameter achieved only approaches a value of 50, indicating that a sintering time of 15 minutes is insufficient to achieve high densities.

Figure 4.10 presents the densification vs. temperature results for 30 minute holds. As with the 15-minute samples, density begins to increase slowly at temperatures above 1200°C, reaching a maximum densification parameter of approximately 80 at 1285°C, corresponding to a high final density of about 98% theoretical.

Finally, Figure 4.11 is the isochronal curve for 60 minute sintering time. Somewhat surprising is the fact that even a 60-minute hold at temperatures lower than 1200°C does not yield significant density changes. However, full density is finally approached in the 1285 – 1290°C temperature range.

4.2.2 Density and Time

Figure 4.12 presents results for density change, measured by densification parameter, with time at sintering temperatures of 1190, 1250, 1270 and 1285 °C. At 1190°C, a temperature below that needed for liquid formation, there is a slow but measurable increase in density with time, which, after an incubation period, appears linear. For sintering temperatures above the solidus, the shape of density-time curve is different. In all cases densification continued until the end of the 60-minute hold time, and the density evolution appears to be characterized by two rates of densification, a fast initial rate after liquid formation, followed by a slower rate of densification where long holds do not yield large increases in density. This indicates that for this alloy system a sufficiently high temperature (and thus volume of liquid) is absolutely necessary for the achievement of full density in a reasonable time period.

To examine more closely the two apparent rates of densification, some experiments were carried out at longer time scales, and the results for densification parameter vs. time are illustrated in Figure 4.13 for a sintering temperature of 1285°C.

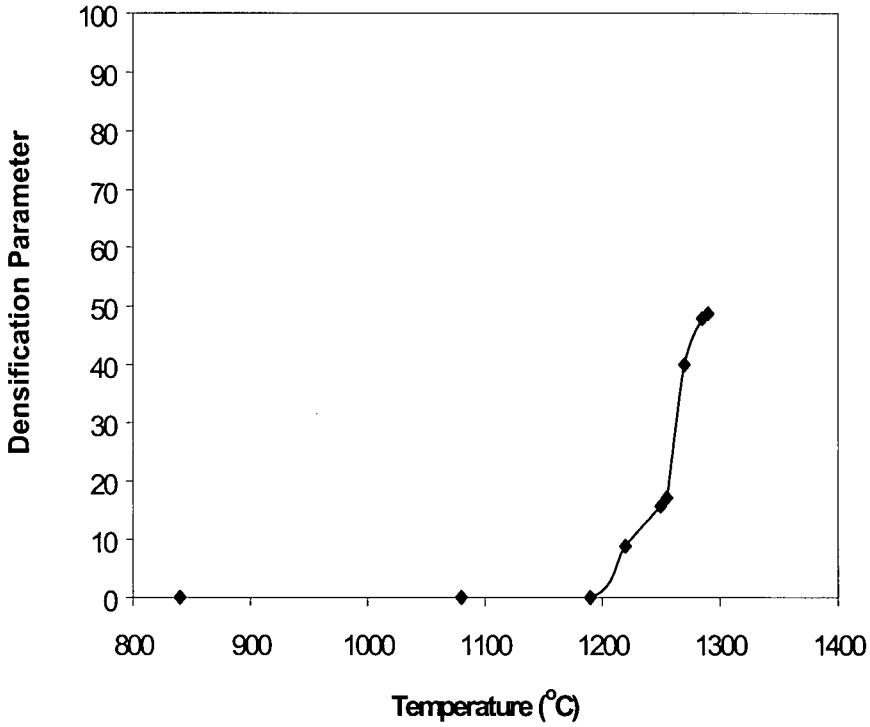

Figure 4.9 Densification vs. temperature (15 minute hold)

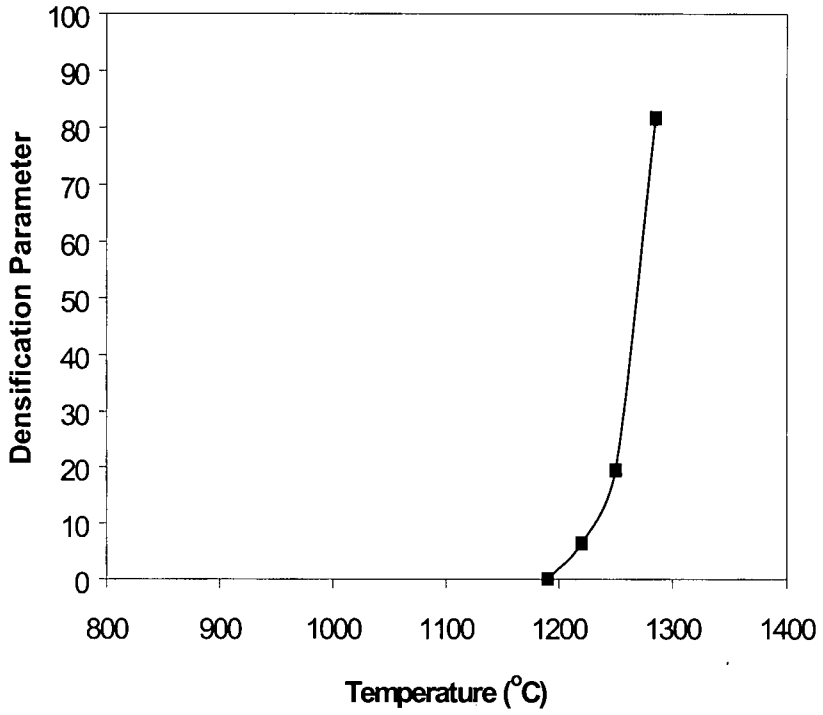

Figure 4.10 Densification vs. temperature (30 minute hold)

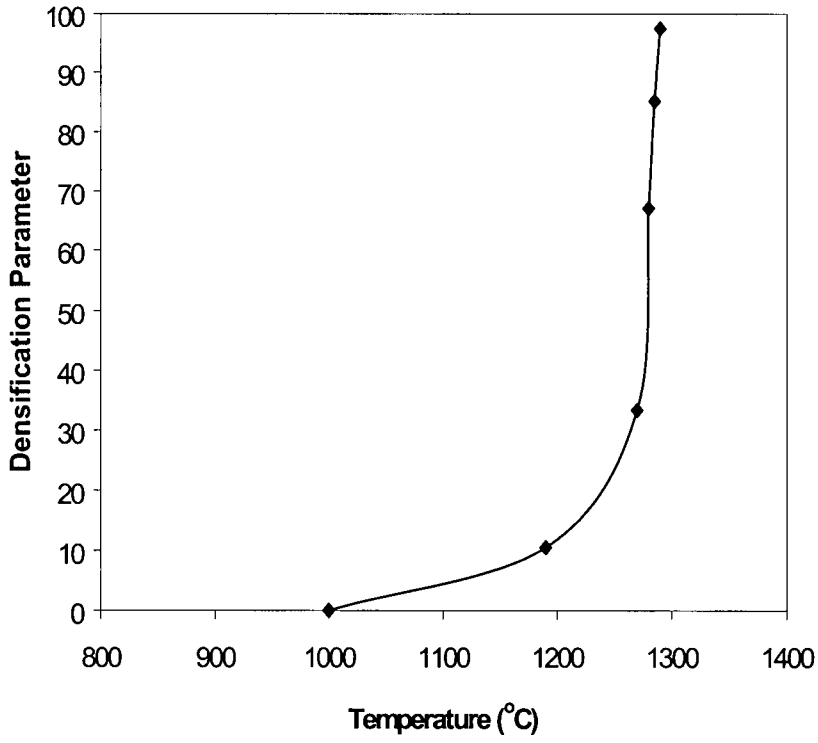

Figure 4.11 Densification vs. Temperature (60 minute hold)

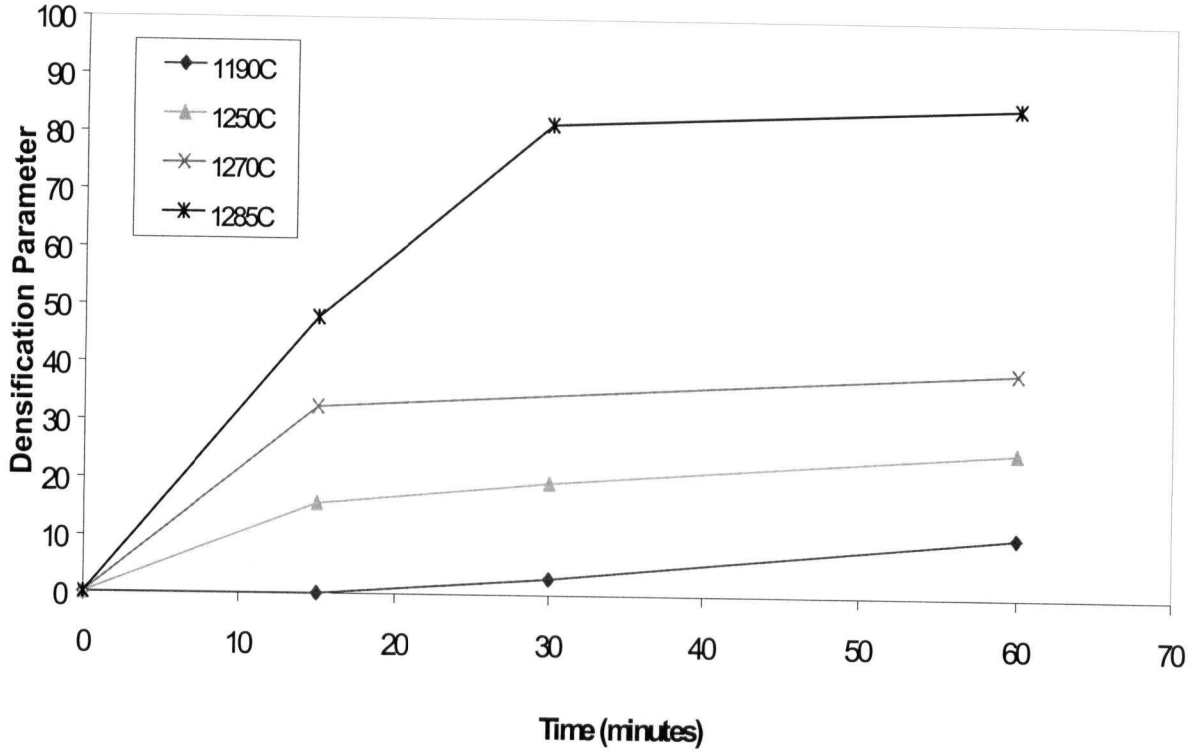

Figure 4.12 Densification parameter vs. sintering time

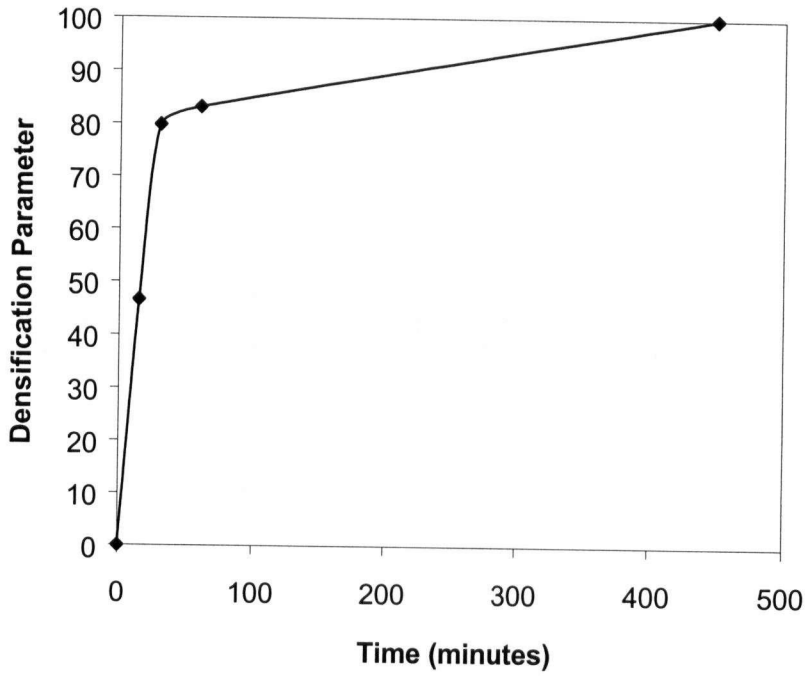

Figure 4.13 Densification vs. sintering time at 1285°C

The two different regimes of densification are clearly visible, as some 80% of the densification occurs during the first 30 minutes. It is observed that at longer hold times the density approached the theoretical value.

4.3 Qualitative and Quantitative Metallography

This section presents micrographs and image analysis data of samples that were heat-treated in the experimental furnace and DSC. Unless noted otherwise, all experiments were performed with powder Blend A, and were cooled quickly from the hold temperature by quenching in order to lock in the high temperature microstructure.

4.3.1 Initial Microstructures

Figures 4.14 and 4.15 show optical micrographs that depict the "initial" porosity structure of a typical sample in the green state following pressing. Samples are left un-etched or are lightly etched to facilitate image analysis identification of voids due to porosity, which appear as black entitities on the micrographs shown. This sample was placed in a 1000°C furnace for 30 minutes in order to remove the lubricant and binder from the pores, and also to strengthen the sample slightly through a small amount of particle-particle bonding in order that the specimen could be prepared metallographically. No measurable densification occurred from the green value of 6.95 g/cm^3 during this heat treatment. The same specimen was also examined quantitatively by image analysis, and the major features of this analysis are presented in the first row of Table 4.4. Assuming spherical pores, the equivalent area pore diameter d is calculated by

$$d = 2\sqrt{\frac{A_m}{\pi}} \tag{4.2}$$

where A_m is the mean pore area as calculated by the image analysis software.

Table 4.4 Porosity Characteristics at 1190°C – Solid State

Time	Porosity	Pore Density	Pore Diameter
0 min	10.88%	1434/mm^2	11.79μm
30 min	7.1%	808/mm^2	12.70 μm
60 min	6.83%	835/mm^2	12.30 μm

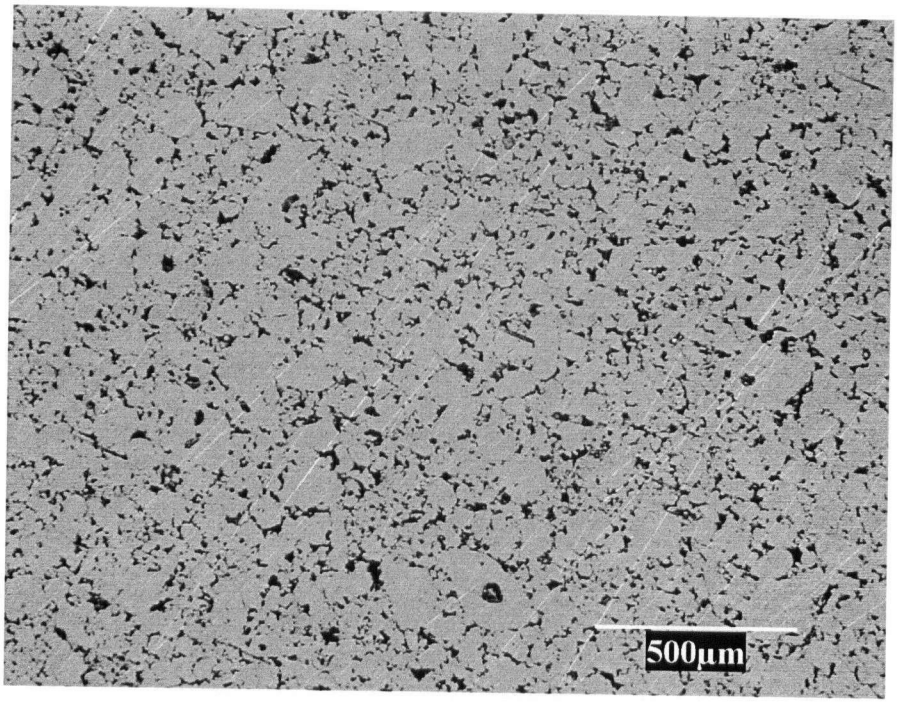

Figure 4.14 Initial porosity distribution of green sample, unetched

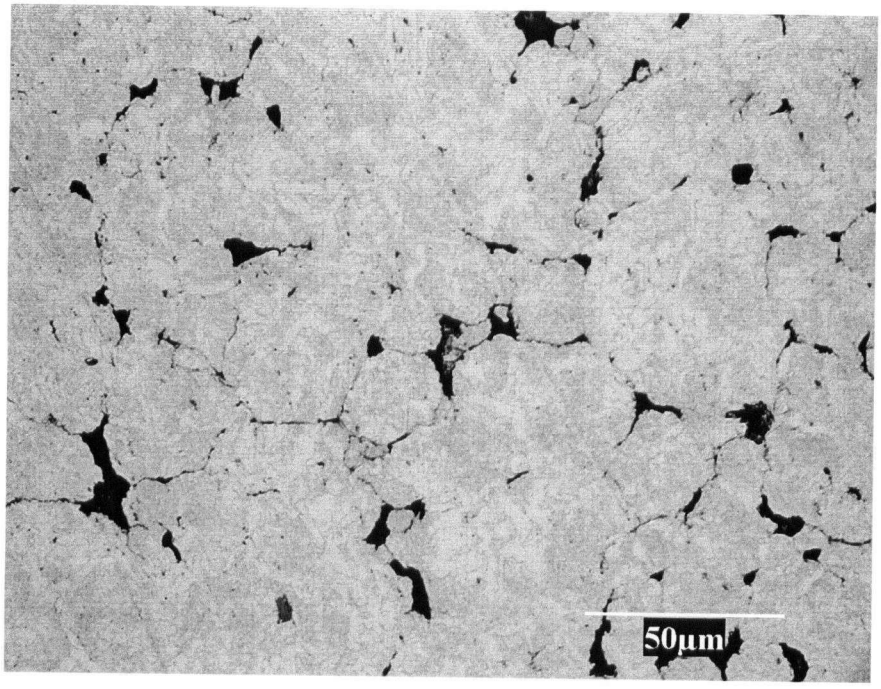

Figure 4.15 High magnification of initial porosity distribution, unetched

The percent porosity determined by image analysis agrees extremely well with the externally measured density of 6.95 g/cm^3, translating to 89.1% theoretical, while the high pore density is characteristic of the green state of the sample.

4.3.2 Porosity Evolution at 1190°C

Figures 4.16 and 4.17 show microstructures of samples sintered at 1190°C for 30 and 60 minutes respectively. Experiments at this temperature, slightly below the solidus, were performed in order to observe the effects of the solid-state densification processes that occur and to trace the evolution of the porosity to a point just before the formation of liquid. It is difficult to visually observe any significant differences between the two micrographs, and this is also true in a quantitative sense. The results of image analysis for these samples are presented in Table 4.4, and the porosity evolution with time at 1190°C is plotted in Figure 4.18 using the data for the green state as a starting point.

Differences in pore density and mean pore size between the two sintered samples are negligible. While there is a marked decrease in total porosity after 30 minutes at 1190°C, the change after 60 minutes is relatively small. It should be noted however, that the total porosities measured after 30 and 60 minutes at 1190°C are not totally consistent with the porosities determined from densities of samples with similar heat treatments in the isochronal test series. One sample sintered for 30 minutes at 1190°C showed negligible reduction in total porosity, ie. total porosity of 10% and after 60 minutes, a porosity of 8% was measured. Overall, however, we can assume a slight decrease in total porosity at this temperature. It should be kept in mind that image analysis is limited to one section through a sample, and may not necessarily be representative of the bulk.

4.3.3 Porosity Evolution at 1250°C

Quenching experiments were performed at 1250°C to observe the microstructures that develop at a temperature intermediate between those where solid-state densification processes dominate, and those where sufficient liquid is present for full densification. Samples were held at 1250°C for times of 15, 30 and 60 minutes, and micrographs of these samples are shown in Figure 4.19 (a-c). While no image analysis was performed on these samples, the densities measured after sintering are presented in Table 4.5.

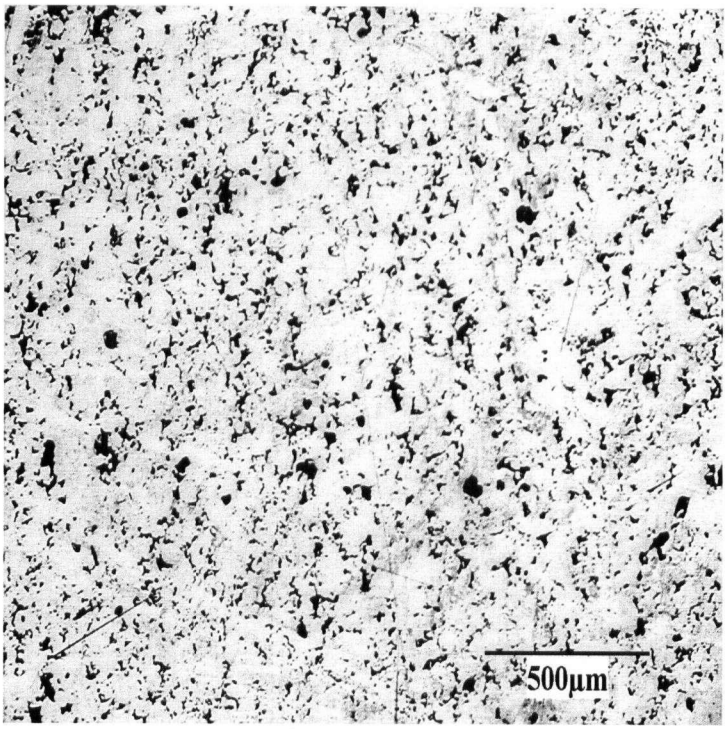

Figure 4.16 Porosity structure after 30 minutes at 1190°C, unetched

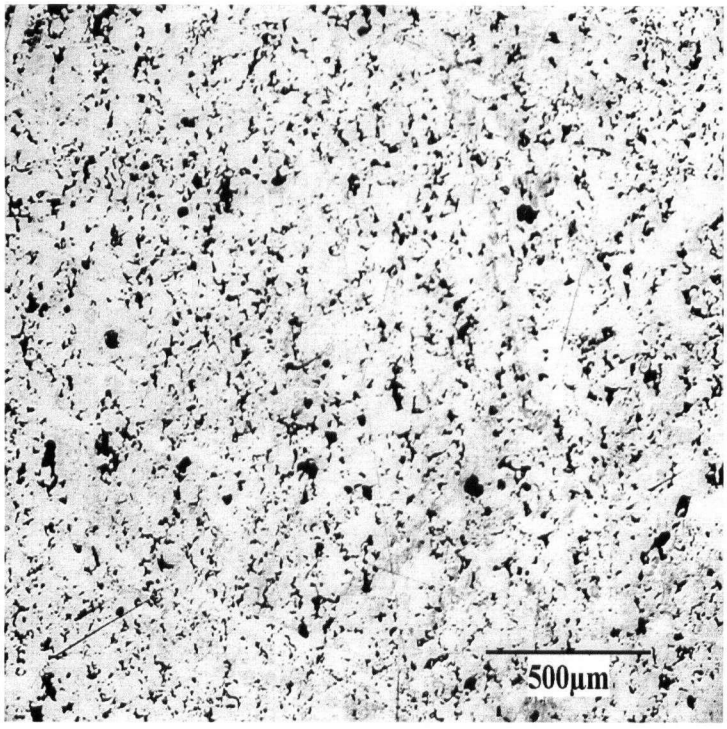

Figure 4.17 Porosity structure after 60 minutes at 1190°C, unetched

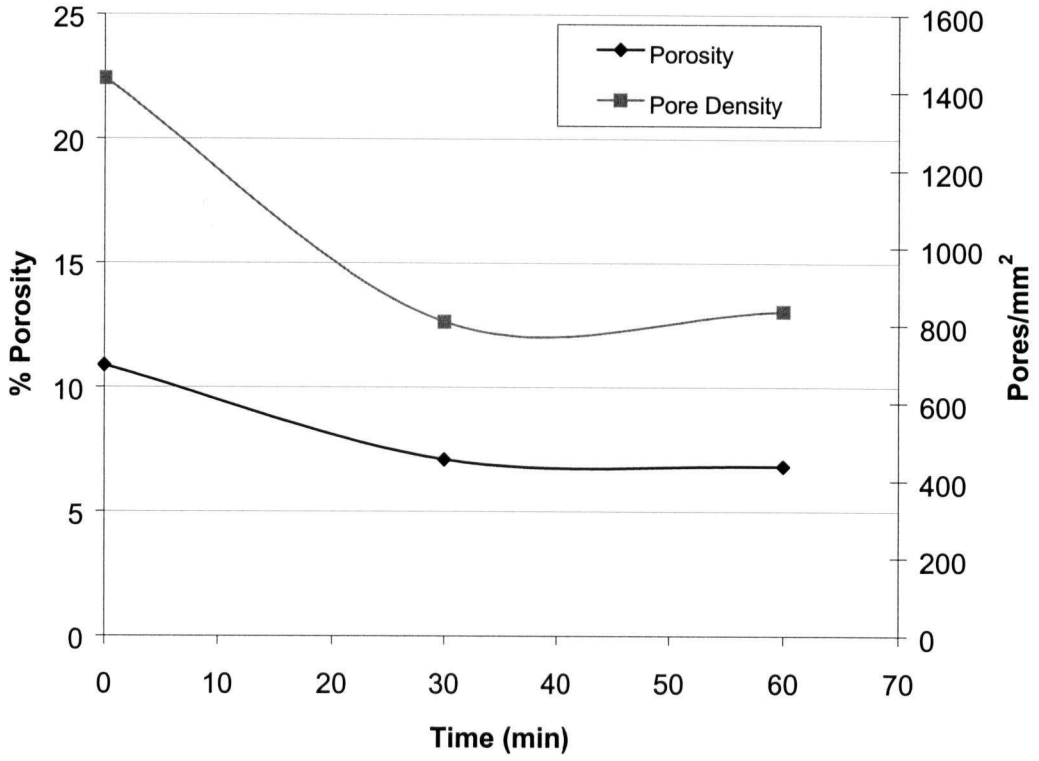

Figure 4.18 Porosity evolution at 1190°C

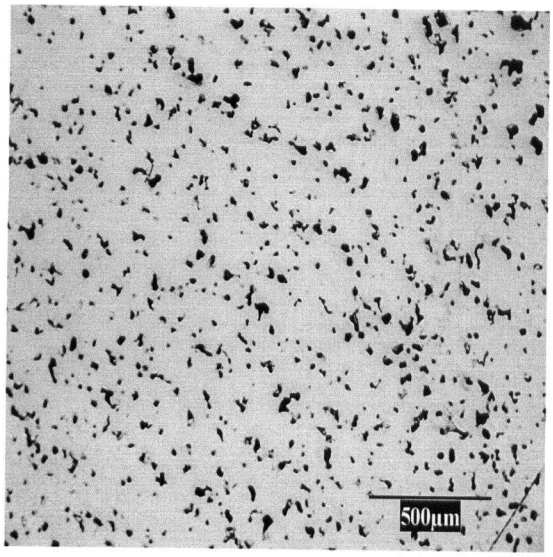

a) Held at 1250°C for 15 minutes

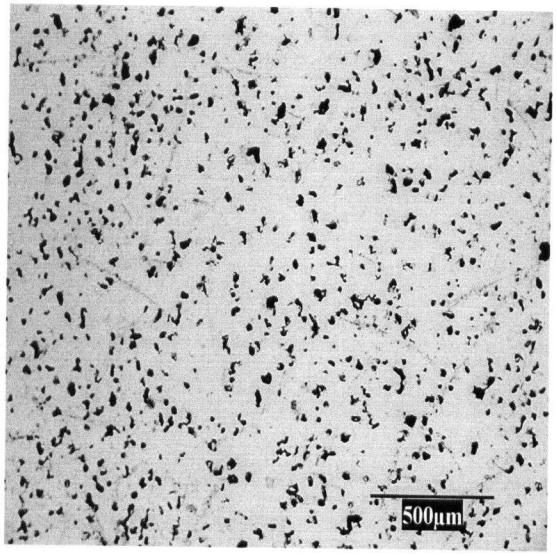

b) Held at 1250°C for 30 minutes

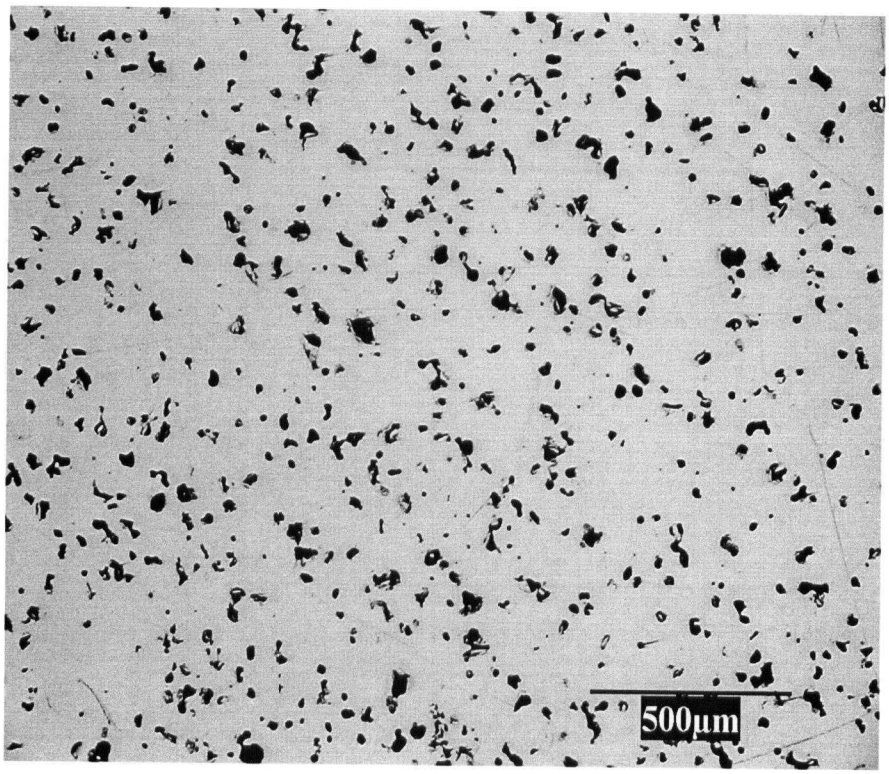

c) Held at 1250°C for 60 minutes, enlarged to show morphology

Figure 4.19 Micrographs of samples sintered at 1250°C, unetched

Table 4.5 Densities of samples sintered at 1250°C

Time	Green Density	Final Density	% Theoretical
15 minutes	6.97 g/cm^3	7.10 g/cm^3	91.0 %
30 minutes	6.98 g/cm^3	7.15 g/cm^3	91.5 %
60 minutes	6.97 g/cm^3	7.19 g/cm^3	92.2 %

From the micrographs and the final densities of these samples, it is interesting to note that increased holding time at 1250°C does not appear to have a significant effect on either densification or pore morphology. However, the pore morphology for these samples, which were sintered in the presence of a liquid phase, is significantly different than the morphologies evident for the samples in Figures 4.16 and 4.17. At the higher temperature, the pores are increasingly more spherical, and of a more uniform size.

4.3.4 Samples Sintered at 1285°C

In all experiments where high densities approaching the theoretical value were achieved, 1285°C was the sintering temperature employed. Two Blend B samples sintered at 1285°C for sixty minutes were subjected to image analysis; the first sintered in the high temperature furnace at UBC, and the other sintered at Stackpole Ltd. The results are presented in Table 4.6.

Table 4.6 Characteristics of Blend B samples sintered at 1285°C for 60 minutes

Sample	Porosity	Pore Density	Pore Diameter
Stackpole	0.81%	119 /mm^2	11.02 μm
UBC	0.55%	72 /mm^2	11.58 μm

Both samples exhibit a very low porosity and pore density and small mean pore size, as illustrated by their similar micrographs in Figures 4.20 and 4.21. Residual porosity is generally spherical, and the grain sizes of the two are comparable. For comparison purposes, the microstructure of a Blend A sample sintered at 1285°C for 60

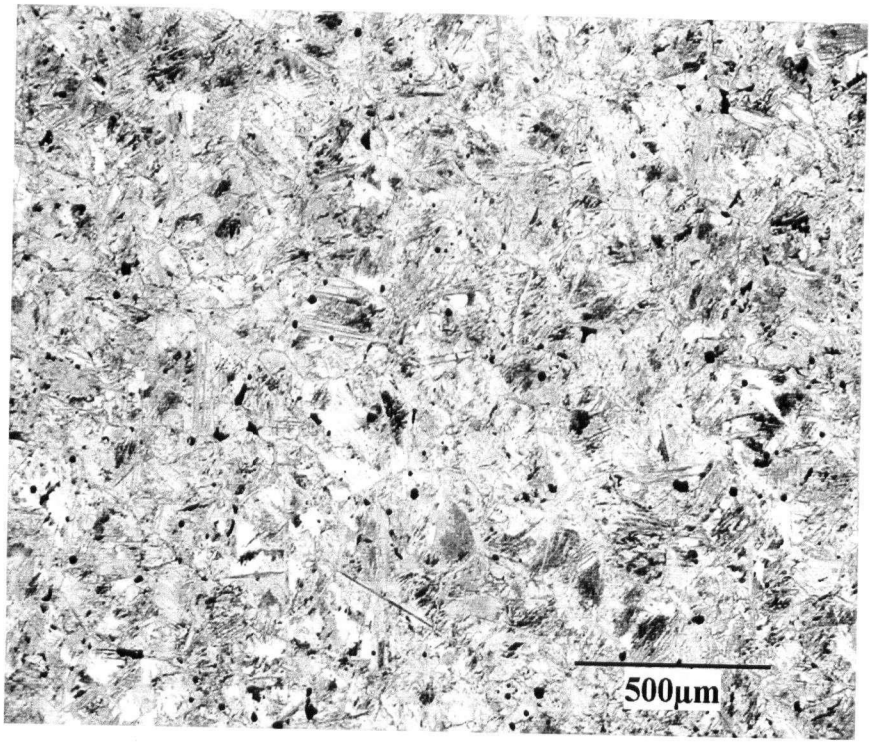

Figure 4.20 Micrograph of Stackpole Blend B sample sintered at 1285°C for 60 minutes

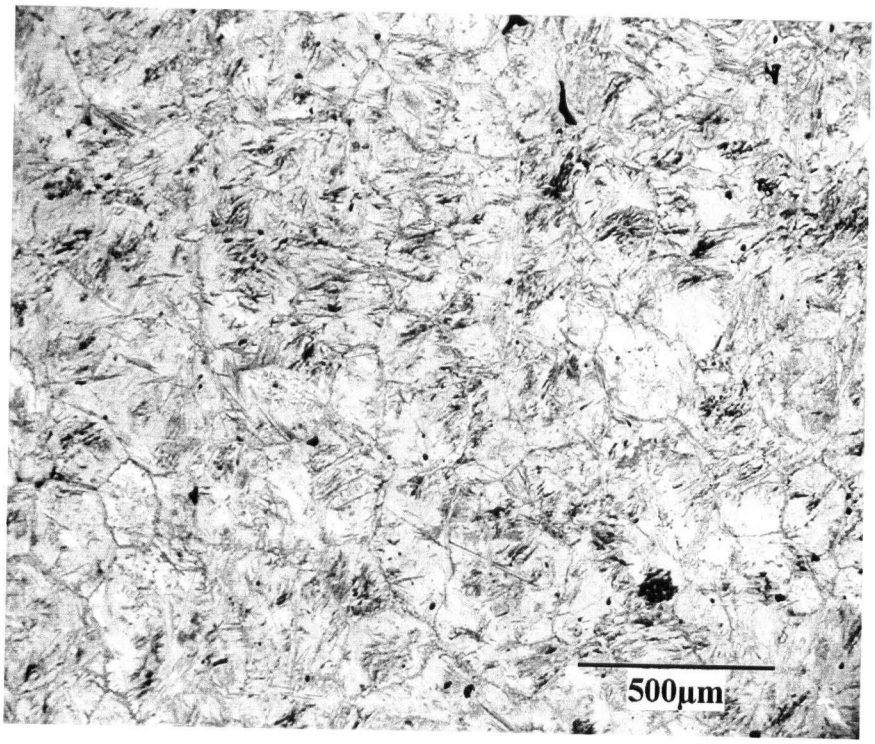

Figure 4.21 Micrograph of UBC Blend B sample sintered at 1285°C for 60 minutes

minutes to a density of 6.85 g/cm^2 (98.5% theoretical) is presented in Figure 4.22. (Note that at 1285°C the two blends will have different amounts of liquid present.)

4.3.5 Porosity Evolution at 1295°C

When samples were sintered at temperatures above 1290°C, they became distorted and blistered, as illustrated in the macrograph in Figure 4.23 for a sample held only 15 minutes at 1305°C. To investigate this phenomenon, a series of quench experiments were performed at 1295°C.

Samples were sintered at 1295°C for times of 5, 15, 30, 45 and 60 minutes, and the 15, 30 and 60-minute samples were chosen for image analysis. Results are shown in Table 4.7, and plotted in Figure 4.24.

Table 4.7 Porosity Evolution at 1295°C

Time	Porosity	Pore Density	Pore Diameter
15 minutes	7.4 %	187 /mm^2	5.26 μm
30 minutes	3.19%	52 /mm^2	5.73 μm
60 minutes	20.11%	59 /mm^2	67.7 μm

The observation that the total porosity actually increases from the level present in the green state while pore density plateaus for the sample held for 60 minutes is extremely surprising. A more complete visual representation of the porosity evolution is given by the micrographs for this series in Figures 4.25 (a-f).

Another interesting observation is that in general the pore density appears to be much greater closer to the surface of the sample as compared with the center of the sample (see Figure 4.25 c) and d)). The occurrence of dense surface porosity is also not restricted to distortion-inducing high temperatures, or long sintering times, illustrated by the micrographs in Figures 4.26 and 4.27, showing edge vs. center porosity for samples sintered at 1295°C for 5 minutes and 1285°C for 60 minutes respectively.

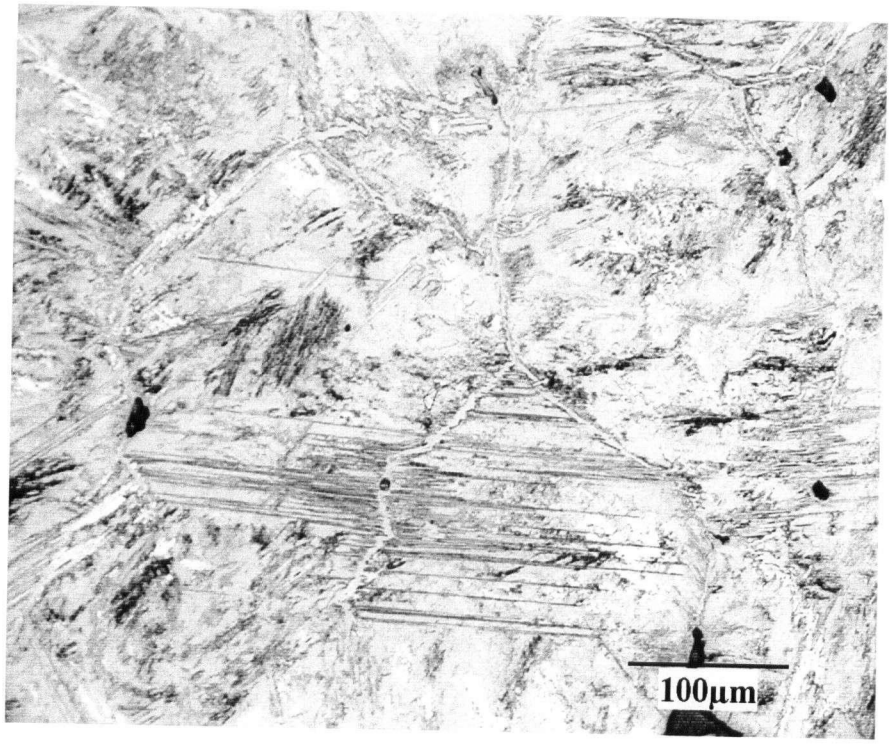

Figure 4.22 Micrograph of Blend A sample sintered at 1285°C for 60 minutes

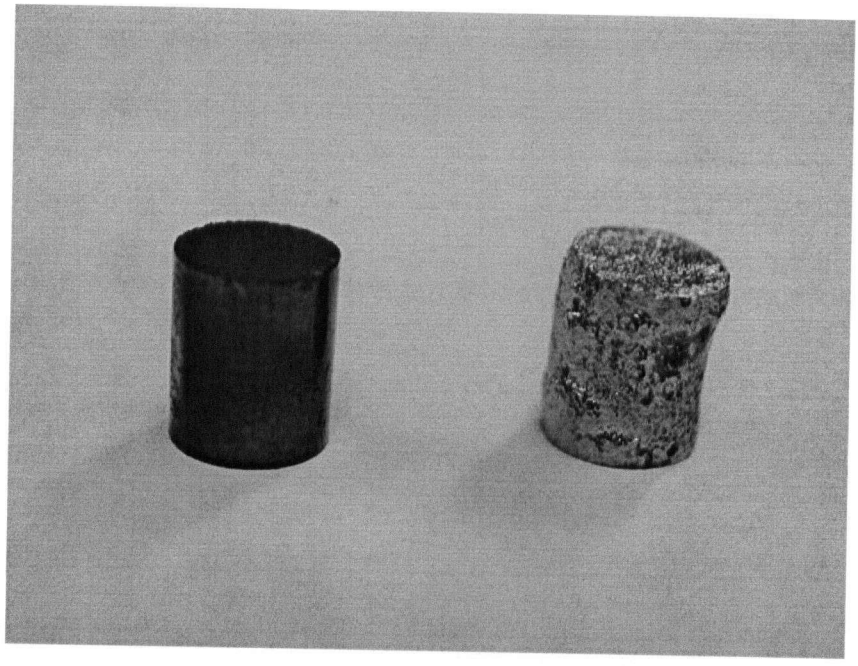

Figure 4.23 Distorted sample (right) produced by 15-minute hold at 1305°C

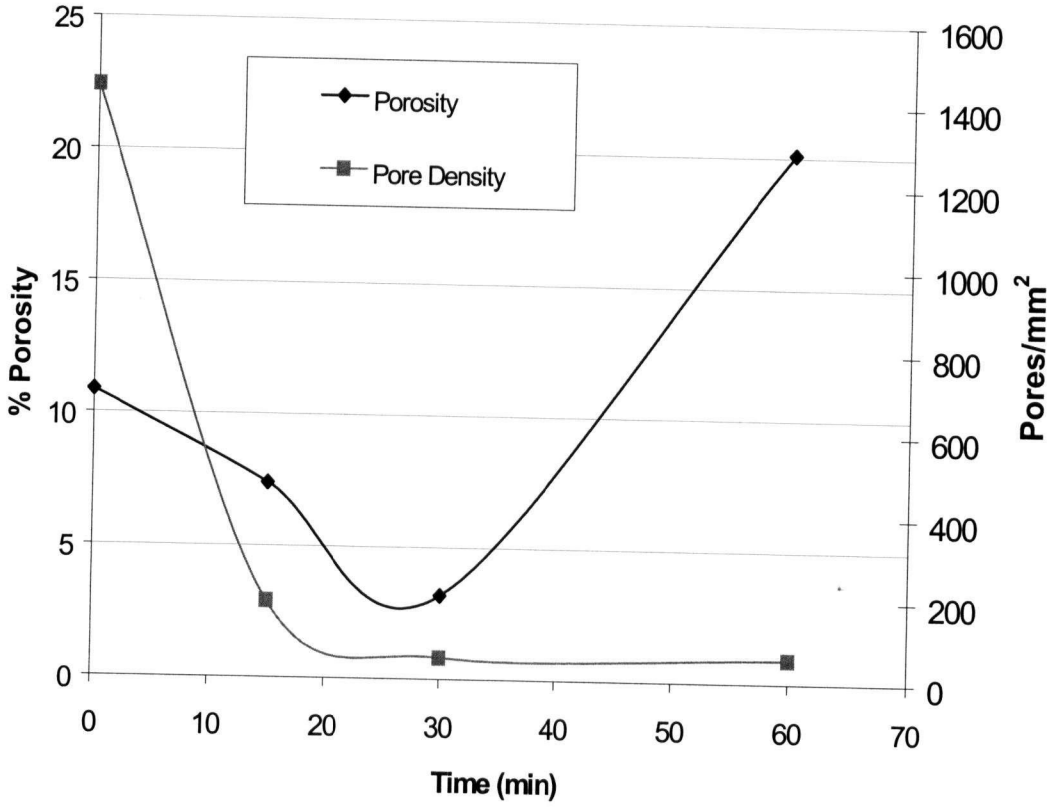

Figure 4.24 Porosity Evolution at 1295°C

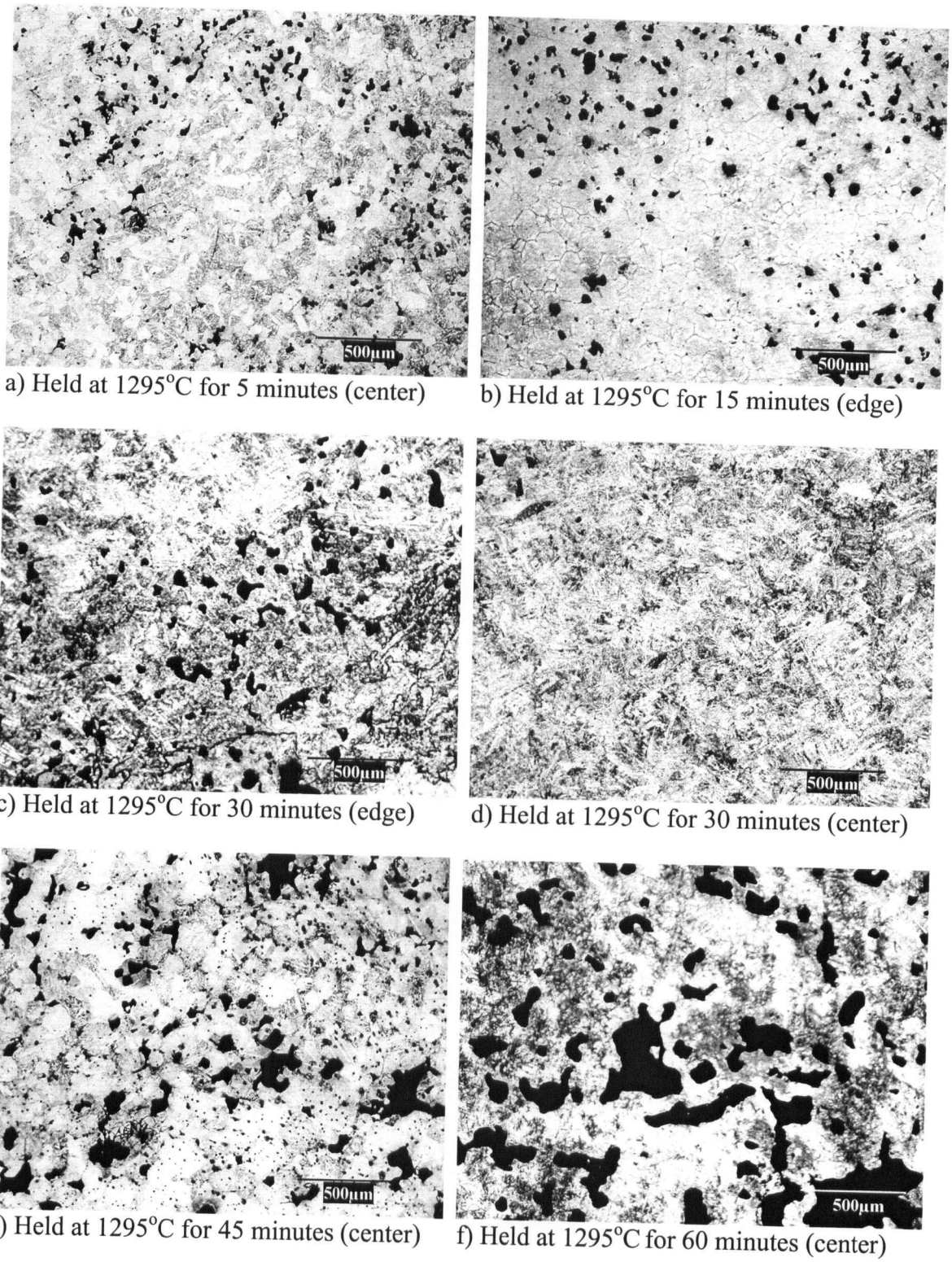

a) Held at 1295°C for 5 minutes (center)

b) Held at 1295°C for 15 minutes (edge)

c) Held at 1295°C for 30 minutes (edge)

d) Held at 1295°C for 30 minutes (center)

e) Held at 1295°C for 45 minutes (center)

f) Held at 1295°C for 60 minutes (center)

Figure 4.25 Porosity Evolution at 1295°C

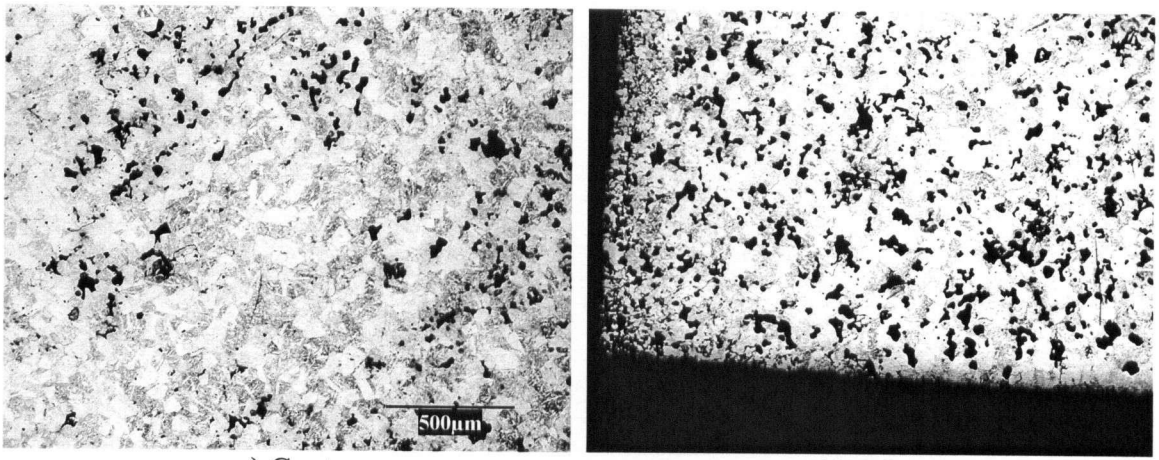

a) Center b) Edge

Figure 4.26 Sample sintered at 1295°C for 5 minutes

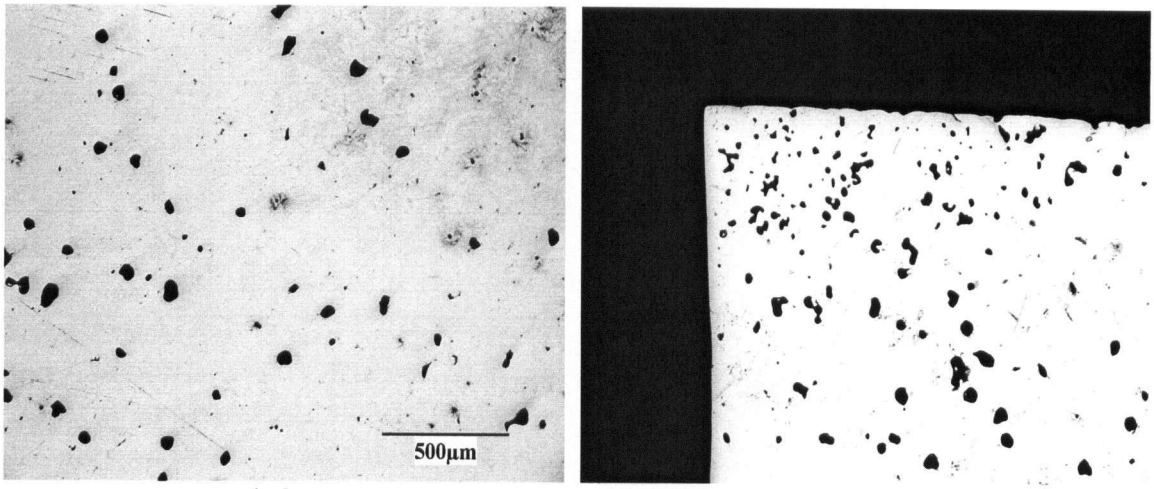

a) Center b) Edge

Figure 4.27 Sample sintered at 1285°C for 60 minutes

4.3.6 Metallography of DSC Samples

Several of the specimens from the DSC sample set using powder Blend B were subjected to further observation. One interesting feature of both sets of DSC tests was the noticeable shape change of the samples observed upon removal from the DSC. While the samples heated to 1290°C retained their initial cylindrical shape, the shape of those taken to near full melting at 1410°C evolved to an unusual, four-sided form with curved surfaces and visible dendrites as shown by the SEM macrographs in Figure 4.28 (a-b). Those samples taken to full melting at 1460°C solidified with the dome-like morphology shown in Figure 4.29, likely driven by surface tension.

Several DSC samples were also metallographically prepared to observe and identify the microstructures present. The microstructures of DSC samples 11 and 12 are presented in Figures 4.30 and 4.31. The high amount of residual porosity is to be expected and is attributed to the relatively short hold time of 20 minutes at 1290°C.

In general, the microstructures of the DSC samples were very similar, regardless of heat treatment, and upon close inspection appeared to comprise a mixture of fine pearlite colonies, carbide plates and varying levels of residual porosity (ie. virtually no porosity was visible in the samples taken to full melting). Individual grains were difficult to identify in most cases, although Figure 4.32 shows a clear magnification of a carbide plate structure spanning a grain boundary in DSC sample 13, taken to full melting. Figure 4.33 shows similar plates that appear to nucleate at an inclusion.

4.4 Remarks

The experiments performed in the DSC and high temperature furnace, as analyzed by heat flow measurements, density measurements, image analysis and metallography, provide many indications of the events that are most likely occurring in the Blend A and Blend B powders. The results of the experiments are analyzed and discussed in detail in Chapter 5.

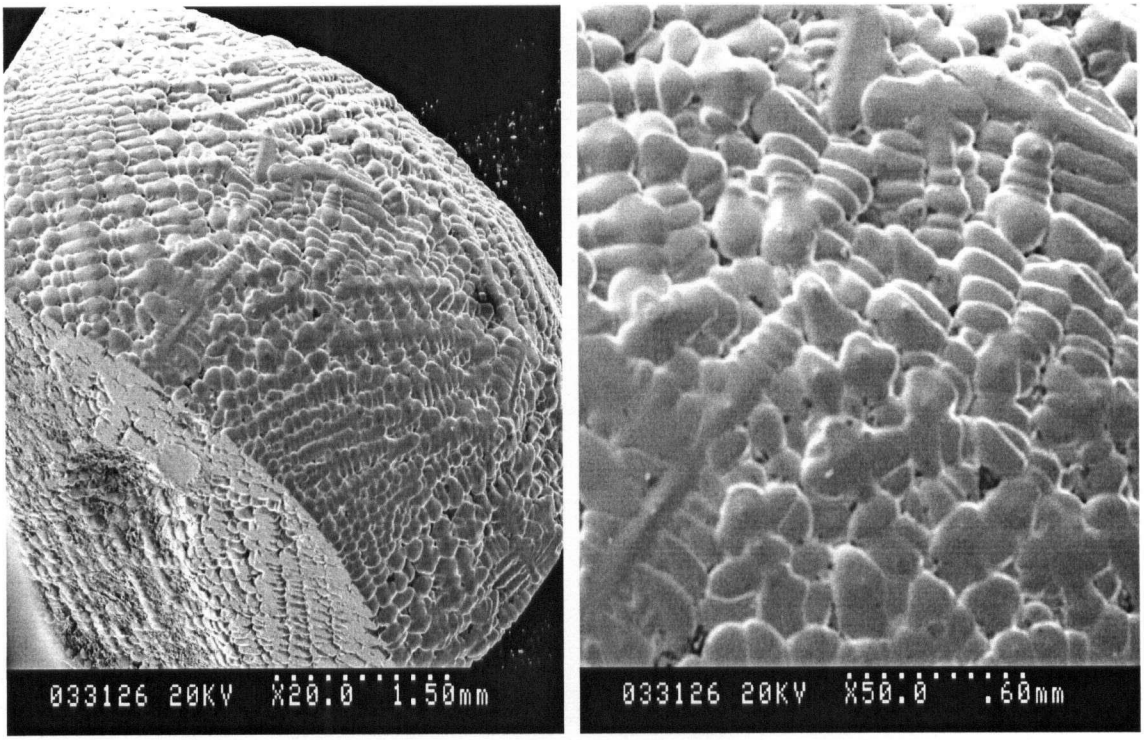

a) 20x magnification b) 50x magnification

Figure 4.28 Secondary electron SEM macrographs of DSC sample 7

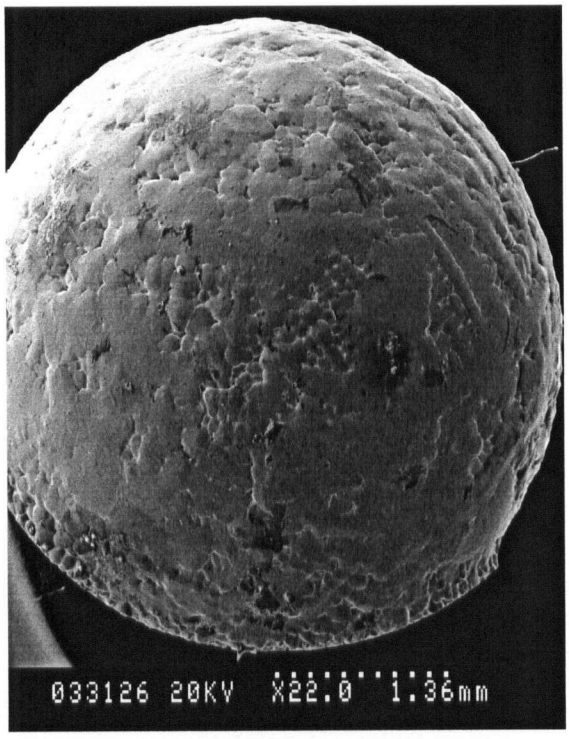

Figure 4.29 Secondary electron SEM macrograph (22x) of DSC sample 13

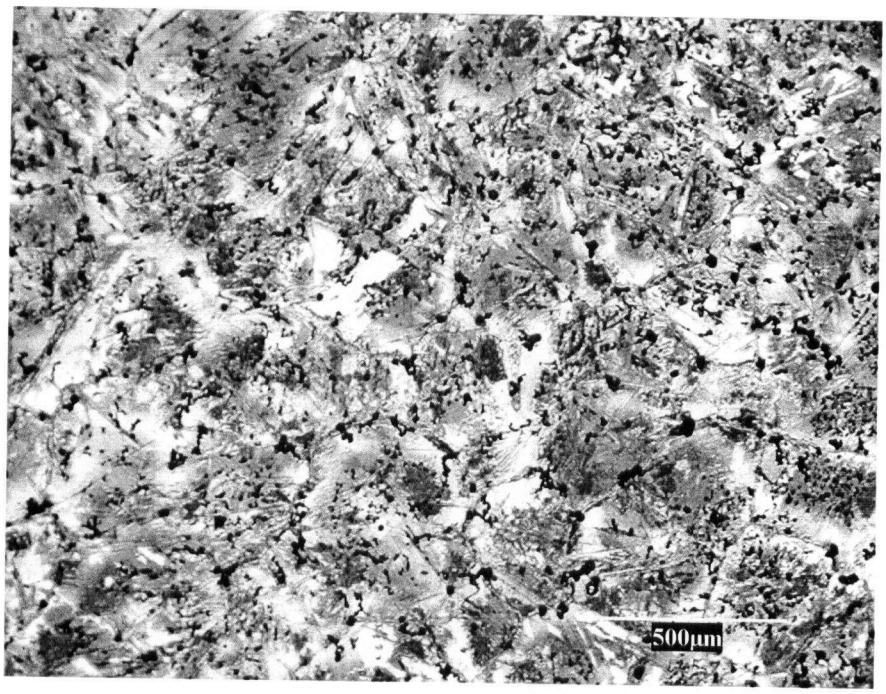

Figure 4.30 Porosity and microstructure of DSC sample 11, held 20 minutes at 1290°C

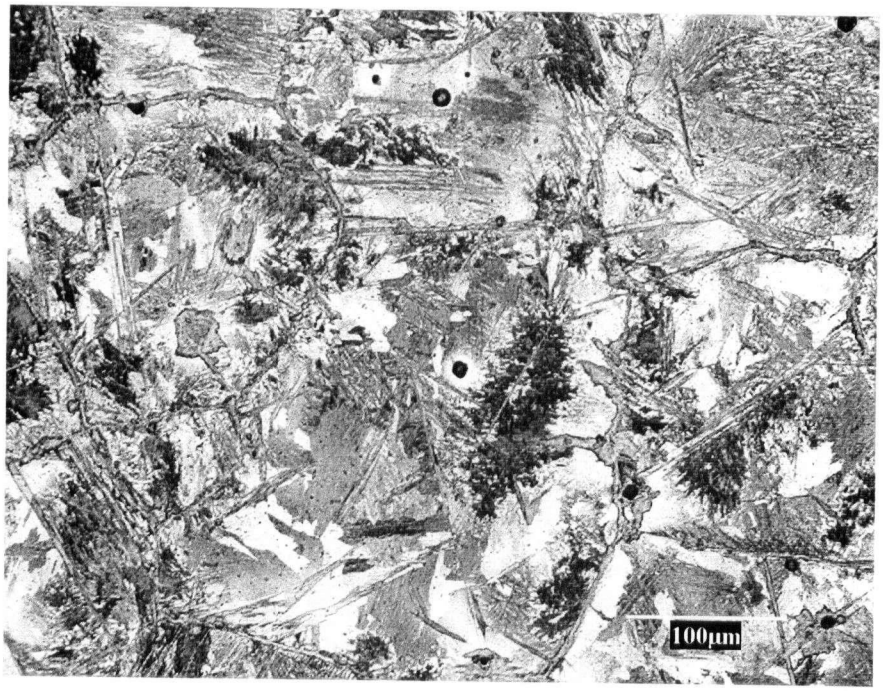

Figure 4.31 Porosity and microstructure of DSC sample 12, held 20 minutes at 1290°C

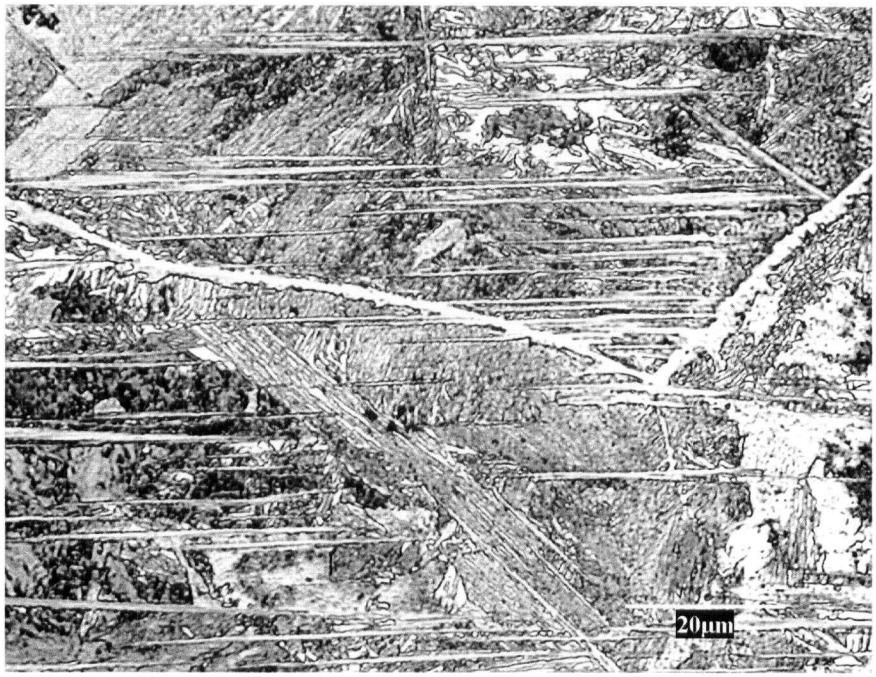

Figure 4.32 Grain boundary and plate structure in DSC sample 13, heated to 1460°C

Figure 4.33 Nucleation of carbide plates at an inclusion in DSC sample 13

Chapter 5: Analysis and Discussion

This chapter attempts to organize and interpret the experimental results presented in Chapter 4 in order to extract the information most relevant to the objectives of this study as well as completing other analysis for additional perspective on the supersolidus sintering process. In general, evidence supports the following progression of events during the process, some of which may overlap;

- Debinding and delubrication events
- Diffusion of carbon from graphite into Fe-Mo powders - homogenization
- $\alpha \rightarrow \gamma$ phase solid state phase transformation
- solid state sintering - bonding
- liquid formation
- liquid phase sintering – densification
- solidification
- $\gamma \rightarrow \alpha$ solid state phase transformation

The discussion is structured as a chronological progression through the sintering process of heating, holding, and cooling, so that the information extracted regarding each event becomes part of the knowledge foundation necessary to evaluate subsequent events.

5.1 Initial Structure, Debinding and Delubrication

The microstructure and porosity arrangement present in the green state after pressing play a significant role as the starting point for the supersolidus sintering process. In the process of interest, and this study, a high green density (90% theoretical) is used. The green density reflects the pore structure; a high green density generally corresponds to a low pore density and small pore diameter. This is seen in the results presented in Section 4.3.1 and in the microstructures of Figures 4.14 and 4.15. It is important to keep in mind that these pores are not empty or gas-filled on entry into the sintering furnace; they contain the organic lubricant (EBS) and binder materials (PVP) that were added to aid the pressing operation. Complete removal of these products is the first priority in the

furnace, as improper delubrication can lead to a number of problems later in the sintering process (Legzdins, 2000).

It has been reported (German, 1996) that a saturated pore condition is not particularly desirable, as on rapid heating, vapour will form quickly beneath the porous surface. If pores are not open to the surface to allow pyrolysis vapour to escape the compact, pockets of internal pressure form. While there is no specific evidence in this study of a link between delubrication/debinding and subsequent porosity formation, there is almost certainly a saturated pore condition, in combination with the closed porosity situation described by Westerman, (1962) when the green density is greater than 90%. A conservative measure involving lowering this green density might be advantageous and will almost certainly not hinder densification, as Lund reported full densification from loose powders (Lund, 1972, 1974).

Of the Blend B DSC samples, 8, 9, 11 and 12 all contained binder and lubricant and thus underwent their removal in the DSC furnace. A close up of the temperature region of interest with traces for these samples as a function of temperature is shown in Figure 5.1. While some peaks attributed to the delubrication and debinding processes are discernible on the DSC curves, the sensitivity of the apparatus was not well suited to detection of events such as these, thus limiting the conclusions that could be made. Small peaks occurred at 152°C and 153°C for samples 11 and 12, heated at 10 °C /min, and at slightly higher temperatures for the samples heated more quickly (159 °C and 166 °C respectively for sample 8 (20 °C/min) and sample 9 (30 °C/min). Peaks at these temperatures are consistent with both the melting temperature of EBS (Jesberger, 1996), as well as typical melting points for many polymeric binders (German, 1996). As such, it is difficult to attribute such peaks exclusively to either the debinding or delubrication processes.

There is however, evidence of activity at temperatures around 400 °C that correspond well with known decomposition temperatures for EBS (300-500 °C, as determined by DTA by Jesberger (1996)). The broadness of these small DSC peaks is consistent with the fact that delubrication occurs by thermal pyrolysis over a range of temperatures during heating. As with the debinding process, delubrication appears to exhibit a slight dependence on heating rate. However, in all tests it appears that the

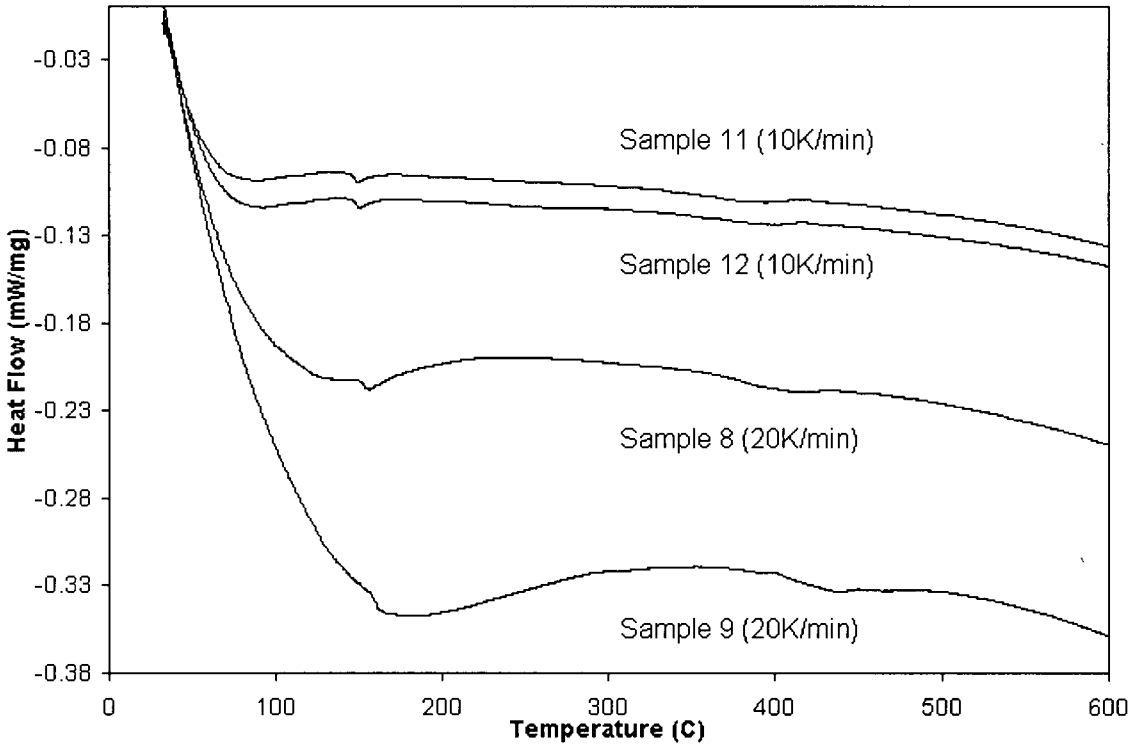

Figure 5.1 DSC traces vs. temperature for DSC samples 11, 12, 18 and 9 over the temperature range of delubrication and debinding

delubrication and debinding events are completed by the time a temperature of 500 °C is reached.

5.2 Phase Transformation and Homogenization

Following the delubrication and debinding events, the next significant occurrence in both powder blends on heating is the phase transformation from a body-centred cubic (BCC) structure to the high temperature equilibrium face-centred cubic (FCC) austenite. This phase transformation is complicated by the interdiffusion occurring between the Fe-Mo and graphite powders. From the Fe-C phase diagram it is known that if the iron powders contained no carbon, they would undergo transformation at approximately 911°C, while if they contained as little carbon even as 0.02%, transformation would begin at the eutectoid temperature of 723°C. In this study the average transformation onset of Blend A was observed to be 745°C, and the average for Blend B was 747°C, both temperatures well below 911°C, indicating that at least some carbon diffusion into the iron powders had taken place.

Several factors contribute to the interpretation of the observation that transformation onset temperatures are approximately 20°C higher than the eutectoid predicted by the phase diagram. The first is the presence of a small amount of molybdenum, which acts to raise the transformation onset slightly. Please see the binary phase diagram section for (Fe-0.85wt%Mo)-C as calculated using Thermocalc™ software in Figure 5.2, as well as the relevant portion of the Fe-C version given in Figure 5.3. The second factor relates to the intrinsic limitations of the DSC in measuring the onset of the transformation peak; a threshold volume of the second phase is necessary for before detection is possible. Finally, we recognize that the heating rates employed are not infinitely slow as assumed in the equilibrium calculations of the phase diagram, and this also contributes to the discrepancy.

The phase transformation and carbon diffusion are simultaneous and synergistic. A schematic view of the process is illustrated in Figure 5.4, where initially, the Fe-Mo powder is surrounded by a film of pure carbon. On heating from room temperature to 740°C, a small amount of carbon diffuses into the metal powder. Once the transformation onset is reached, the carbon containing volume of metal transforms into a

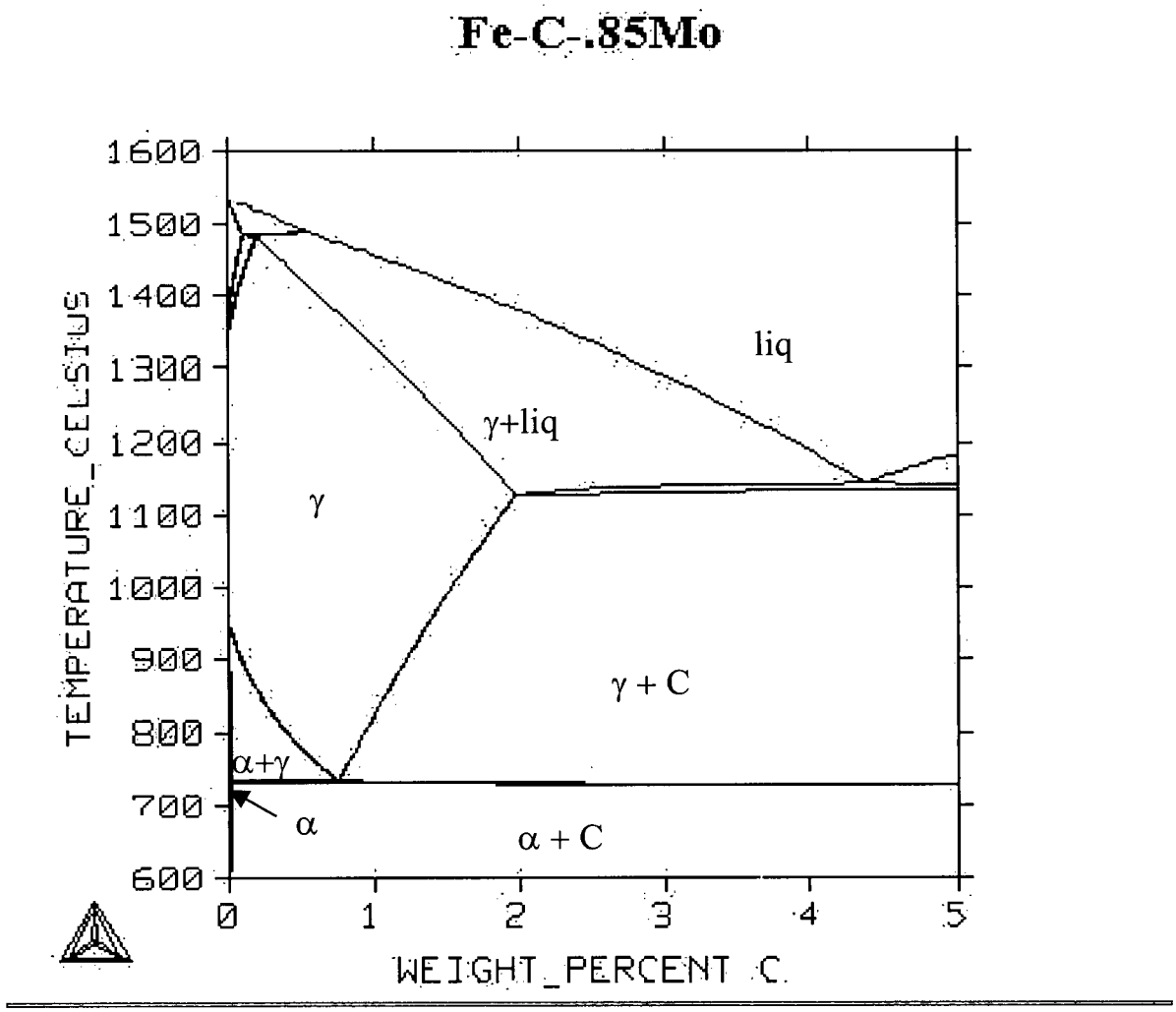

Figure 5.2 Thermocalc™ equilibrium diagram for Fe-C-0.85wt% Mo for 600-1600°C

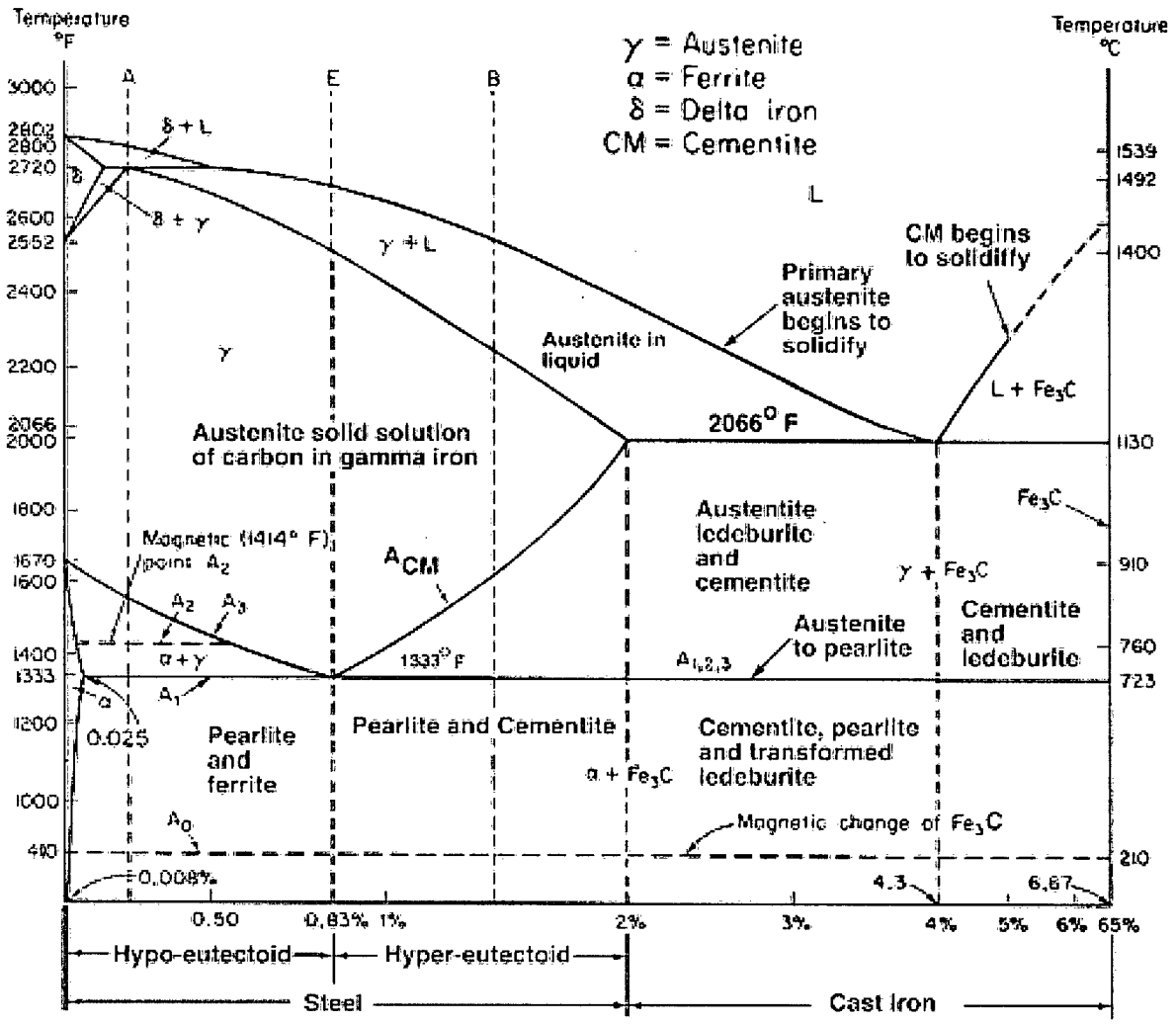

Figure 5.3 Iron-Fe_3C equilibrium diagram (from the Georgia Tech Joint Student Chapter of ASM/TMS website www.cyberbuzz.gatech.edu)

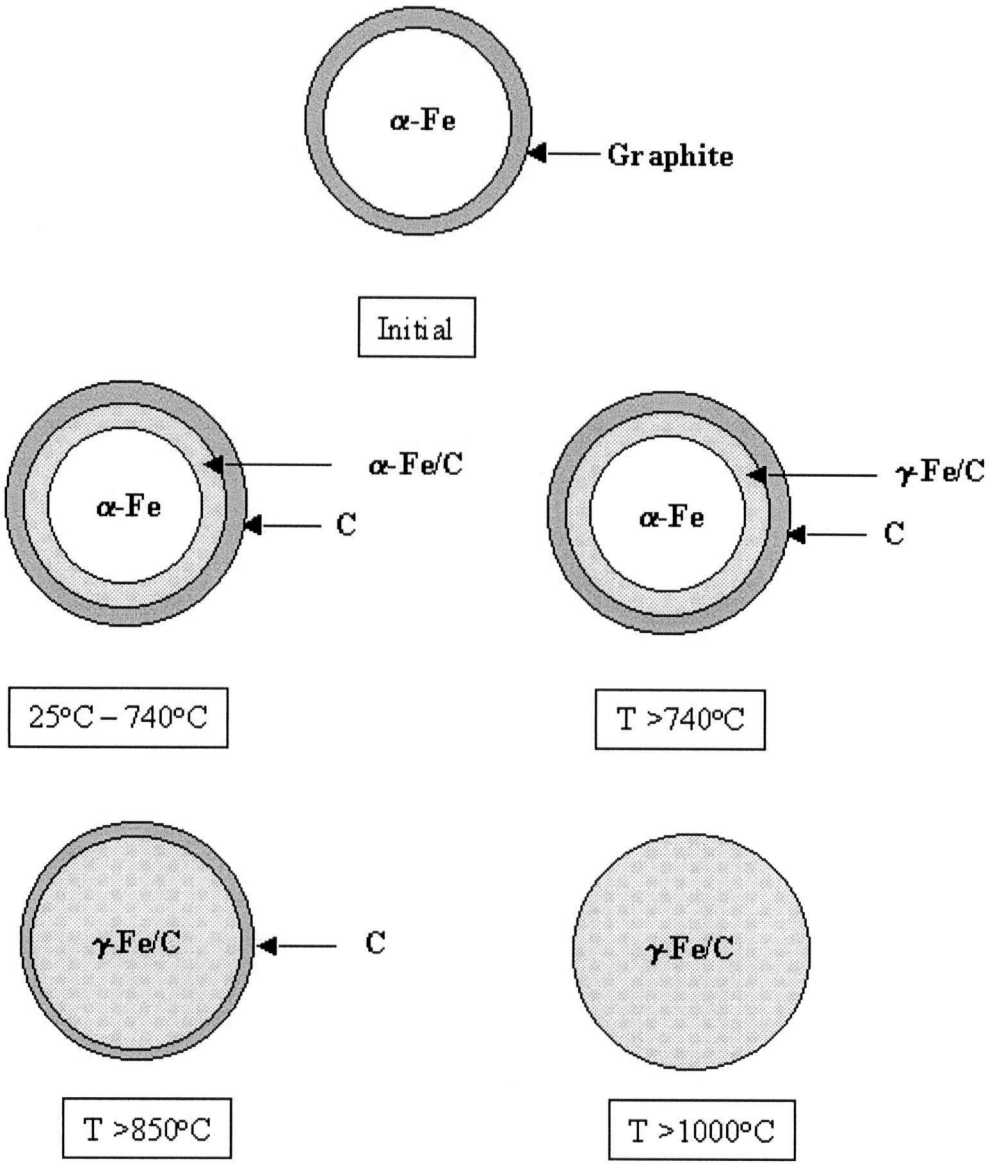

Figure 5.4 Schematic of proposed phase transformation and diffusion sequence

mixture of austenite at the equilibrium composition, and ferrite. Carbon continues to diffuse into the ferrite at higher rates due to the increase in diffusivity with rising temperature. In turn, as the carbon concentration of the ferrite increases, it undergoes transformation. The self-perpetuating process continues until the transformation is complete, and the material is fully austenitized. DSC results indicate that transformations measured were usually complete by 850°C. Once this occurs, the material is free to continue absorbing carbon, more readily as the temperature rises, until the bulk concentration of 1.5 wt% C, well below the solubility limit of austenite, is reached. The question now becomes this: when is the material fully homogenized with respect to carbon content? The answer will be dependent on heating rate, and an estimation of the homogenization is given as follows.

For simplicity, the implications of the phase transformation below 911°C will be ignored, and it is assumed that the material is fully austenitic at 911°C with no carbon diffusion below that temperature. This will provide an upper bound for the initiation of homogenization. The following assumptions are made:

1) The diffusivity is not concentration dependent. This is a conservative assumption, as it has actually been shown that the diffusivity of carbon in iron increases with carbon concentration (Shewmon, 1989).
2) The 0.85 wt% molybdenum has no significant effects on carbon diffusion.
3) The surface concentration is not a function of temperature.
4) The homogenization is diffusion controlled, ie. there is no interfacial barrier.

Since the temperature and thus the diffusivity are constantly changing in this system, an *effective* diffusion product that combines the diffusivity and time must be used. This is an averaged product, Dt_{eff} given by

$$\overline{Dt_{eff}} = \int_0^t D(t)dt \tag{5.1}$$

where t is time and D is diffusivity. D is usually given as a function of temperature, T,

$$D = D_0 \exp[-Q/kT] \tag{5.2}$$

where D_o is a proportionality constant, k is Boltzmann's constant, and Q is the activation energy for diffusion. Temperature is related to time by means of the heating rate, ξ, and thus a simple transformation of variables yields

$$\overline{Dt_{eff}} = \int_0^t D(t)dt = \frac{1}{\xi}\int_{T_o}^{T} D_o \exp\left[\frac{-Q}{kT}\right]dT \tag{5.3}$$

where T_o is the initial temperature. Since analytical integration of the exponential term is not possible, determination of Dt_{eff} was achieved by numerical evaluation, assuming a heating rate of 20°C/min (the industrial maximum), initial temperature of 911°C, and using diffusion data from Bester (1972).

In his monograph *The Mathematics of Diffusion*, Crank (1972) solves the diffusion equation for the case of non-steady state diffusion in a sphere, assuming constant surface concentration. He gives the solution for the concentration C as a function of radial position r as:

$$\frac{C - C_1}{C_o - C_1} = 1 + \frac{2a}{\pi r}\sum_{n=1}^{\infty}\frac{(-1)^n}{n}\sin\frac{n\pi r}{a}e^{-Dn^2\pi^2 t/a^2} \tag{5.4}$$

where C_1 is the initial concentration (in this case C_1=0), C_o is the surface concentration (in this case C_o=1), and a is the radius of the sphere. The concentration at the centre is given by the limit as r →0, so

$$\frac{C - C_1}{C_o - C_1} = 1 + 2\sum_{n=1}^{\infty}(-1)^n e^{-Dn^2\pi^2 t/a^2} \tag{5.5}$$

In this case, a particle size of 100μm was used, giving a radius of 50μm, and the calculated Dt_{eff} is substituted for the product of diffusivity and time, Dt. The concentration profile as a function of time from equation (5.5) is plotted in Figure 5.5. From the graph, we can see that the centerline concentration is unity by the time that the temperature has reached 970°C. Thus, it is concluded that the material is fully homogenized with respect to carbon concentration well below the temperatures of first liquid formation, and even before temperatures at which substantial solid state sintering take place.

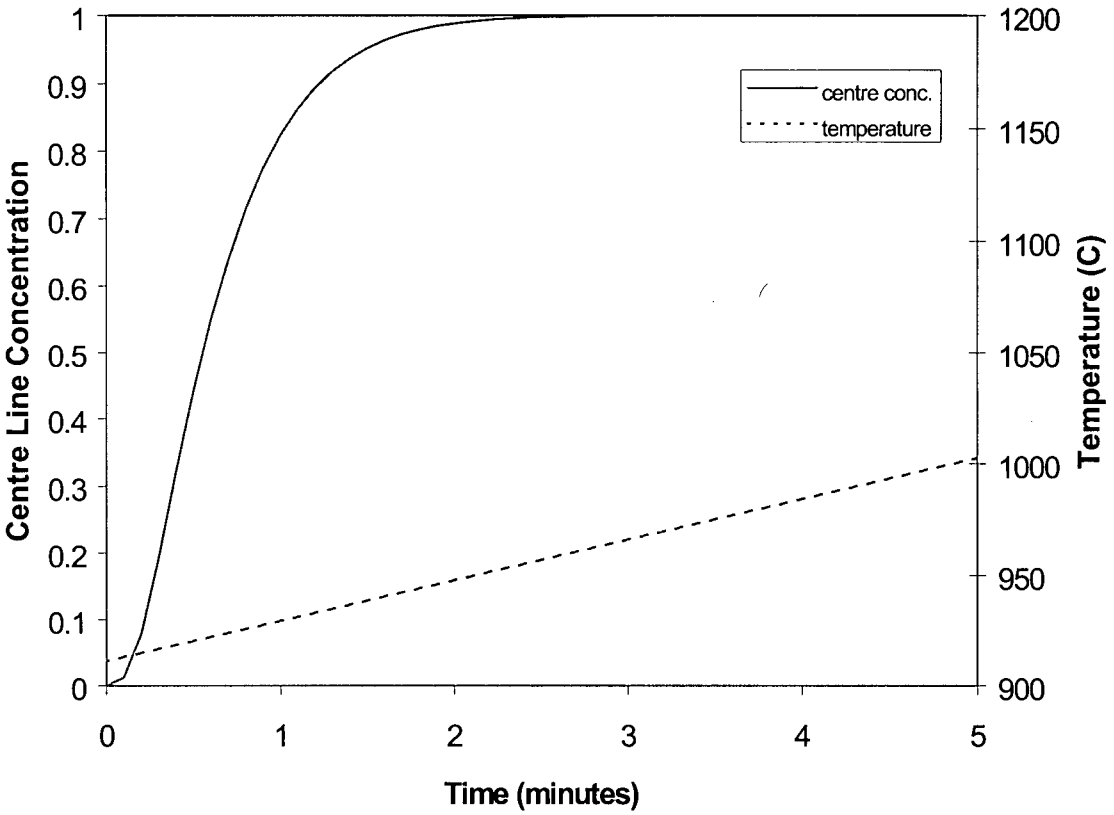

Figure 5.5 Centreline carbon concentration as a function of time in 100μm particles surrounded by graphite, heated at 20K/min from 911°C

5.3 Solid State Sintering

Once the alloy is homogeneous and austenitized, the final precursor to the formation of liquid is the bonding that occurs by solid state sintering. Solid state sintering is able to occur once the temperature is high enough to promote sufficient atomic motion for the primarily diffusive mechanisms to become operational. Traditionally, iron based P/M products are sintered in the solid state at 1190°C, as were the samples in this study. The effects of solid state sintering in Blend A were presented in section 4.3.2 and can be seen as a progressive sequence from Figure 4.14 at time zero, to Figure 4.16 after 30 minutes and then to Figure 4.17 after 60 minutes.

The significant feature of these results is that even though the total amount of porosity does not decrease significantly during sintering, the pore density, or number of pores/unit area does. In addition, the mean pore size increases slightly from that observed in the green state. Visually, it is observed that pores are slightly smoother after time at temperature. This evidence suggests that the solid state sintering in this case may be described by the classic two-sphere sintering model, whose intermediate stage is characterized by a smoothening of the pores, and interconnected cylindrical porosity network. Large pores grow at the expense of small ones; ie. Ostwald ripening via vacancy transport at grain boundaries is the mechanism of pore coarsening. For a more comprehensive description of the two-sphere sintering model, the reader is referred to German (1994).

The amount of densification observed during the solid state sintering experiments performed in this study is small compared to that found in a traditional ferrous press and sinter P/M operation where sufficiently high densities are achieved after an hour of sintering. For example, German (1994) reports that a pure iron powder underwent a porosity reduction from 20% to less than 10% after sintering for 100 minutes at only 870°C. However, this powder had a particle size of only 7 μm, providing a significantly high driving force for surface area reduction by sintering. (Recall that the driving force for sintering is inversely proportional to particle radius). Powders designed for supersolidus liquid phase sintering are often large, one of the economic advantages of the process, as in this case where 70% of the powder has diameters that fall between 45 and 150 μm. As such, the driving force for solid state sintering in these powders is relatively

low. From a densification point of view this is not too important, since the SLPS process will provide the primary mode of densification. However, even a small degree of metallurgical bonding between particles will help to provide strength to the compact upon liquid formation.

5.4 Liquid Behaviour

As was determined by the DSC measurements, the first liquid in Blend A begins to form at 1227°C, while in Blend B it appears slightly earlier at 1213°C. In order to see how the measured values compared with those predicted by phase equilibria, Thermocalc™ software and Fe 2000 database were used to generate values for mole fraction liquid as a function of temperature for both alloys. The results are plotted in Figure 5.6, also showing the reciprocal quantity, ie. mole fraction FCC austenite, with temperature.

The first observation of this plot is that the temperature dependence of the liquid fraction is very non-linear; a linear approximation between the solidus and liquidus temperatures would be very inaccurate. The second observation is the similarity of the curves for the Blend A and Blend B alloys; they are identical in shape but there is a difference of approximately 5% or greater in the amount of liquid present at any given temperature. Blend B has the higher volume liquid present, as expected due to its higher percentage of alloying elements.

The Thermocalc (TC) and DSC solidus and liquidus values are presented in Table 5.1 and are remarkably consistent. Both of the measured solidus values are slightly below the theoretical ones; this is within the realms of experimental error, but might also be predicted due to the nature of the prealloyed Fe-Mo powder. Prealloyed powders often begin to melt at temperatures slightly below the melting point due to non-equilibrium freezing during production. Homogenization during slow heating often eliminates this artifact, but in any case the discrepancy is not significant. The excellent agreement between the measured and calculated values of the solidus and liquidus temperatures is an endorsement of the validity of the Thermocalc™ database and its applicability to the alloy systems that are being studied.

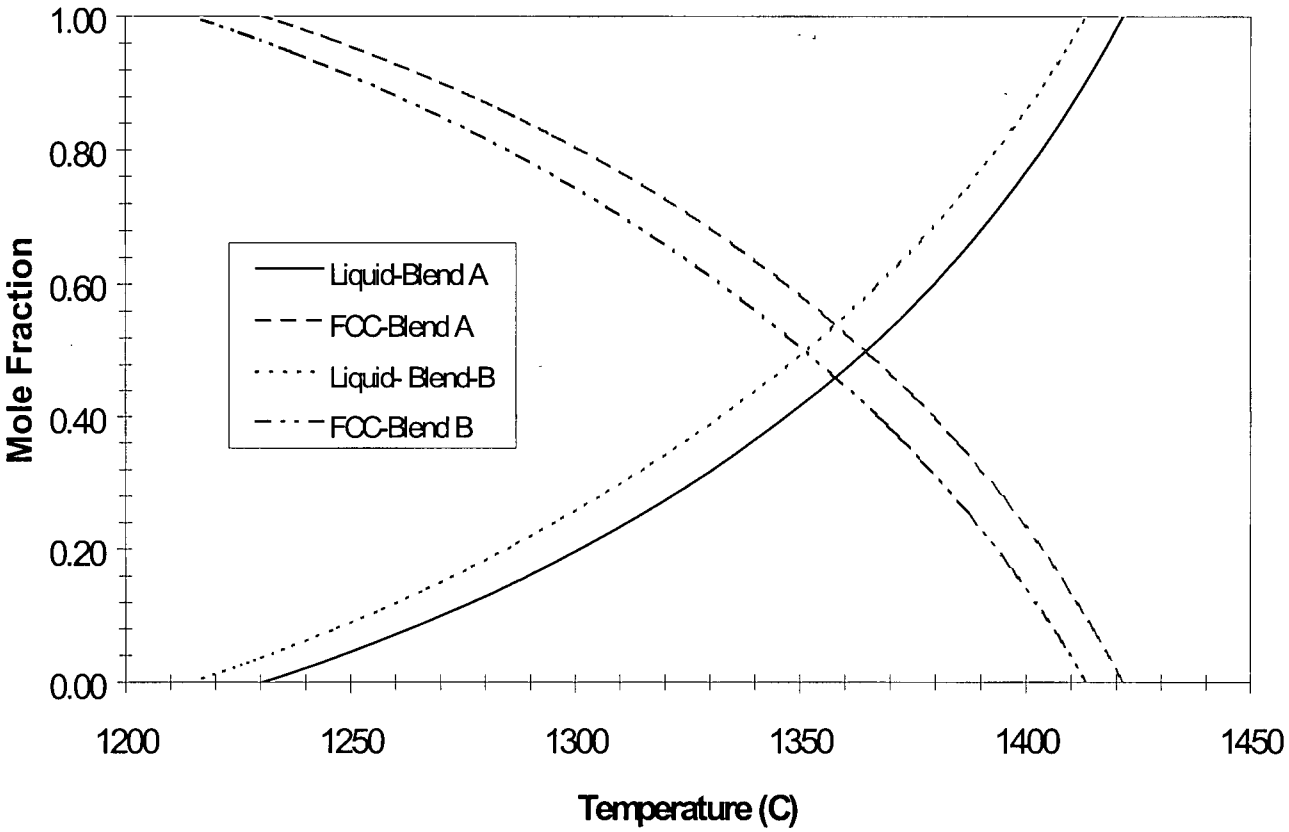

Figure 5.6 Mole fractions of liquid and austenite as a function of temperature for Blend A and Blend B, calculated using Thermocalc^{TM}

Table 5.1 Measured and Calculated Liquidus and Solidus Temperatures

	Blend A (DSC)	Blend A (TC)	Blend B (DSC)	Blend B (TC)
Solidus Temperature (°C)	1227 +/-5	1230	1213 +/- 5	1217
LiquidusTemperature (°C)	1400 - 1422	1421	1400-1412	1413

5.5 Liquid Phase Sintering

On arrival at the sintering temperature, the material has undergone delubrication and debinding, phase transformation, has a homogeneous composition, and has been strengthened by some degree of solid-state bonding. Liquid formation has been initiated, and the liquid begins to penetrate the grain boundaries of the material. Attention may now be focused on densification and pore evolution.

The first tool for characterizing the densification behaviour is the isochronal sintering curve, which was presented for powder Blend A in figures 4.9-4.11 for three different sintering times. The shape of these curves is characteristic of supersolidus sintering, and is similar to those curves shown for various alloys in Figure 2.11 of the literature review chapter. It is obvious from figures 4.9-4.11 that an increase in hold temperature increased the maximum density that was achieved; a sintering temperature of 1285 - 1290°C induced the most densification. While 15 minutes proved insufficient for density improvements of more than 5% at this temperature, after 30 minutes samples were close to 98% fully dense. Sintering for 60 minutes yielded minimal improvements.

Unfortunately, since the temperature at which distortion was observed, T_d, was approximately 1300°C, only slightly higher than the temperature required for full densification, the optimal sintering window is extremely small. One important conclusion from the isochronal tests is that the "sinterability" of the alloy is inherently low.

Turning to Figures 4.12 and 4.13, showing the evolution of density with time, two rates of density change are visible in all samples sintered in the presence of a liquid phase. The first, rapid regime of densification is attributed to viscous flow sintering due to the capillary action of the liquid. It appears to operate over the first fifteen minutes of sintering for samples at 1250 and 1270 °C, and over the first 30 minutes for samples

sintered at 1285°C. The stress, σ, due to the capillarity exerted by the liquid is estimated by equation 2.8, repeated here:

$$\sigma = \frac{5.2\gamma_{lv}\cos\theta}{R\left(\frac{\Delta L}{L_o}\right)} \tag{5.5}$$

where γ_{LV} is the liquid-vapour surface energy, θ, is the wetting angle, assumed to be 0°, R is the particle size, and $(\Delta L/L_o)$ represents the linear shrinkage. Note that in this study, greater shrinkage occurred with greater temperature and thus liquid volume, meaning that the capillary stress was actually smaller at higher liquid volumes. The question is then raised: why is higher densification achieved with more liquid? The answer lies in the fact that while the driving force is lower at the higher liquid content, the extra liquid helps to lubricate the grain boundaries and aid grain sliding and rearrangement during sintering. It is estimated (German, 1997) that a fractional coverage of grain boundaries by liquid of 0.73 is necessary to initiate densification. Thus the critical amount of liquid for densification is balanced between the need for a high driving force, but also grain boundary liquid coverage. This explains why the Blend A samples sintered at 1250°C, at a liquid fraction of 0.05, limited densification occurred, while at 1285°C, at a liquid fraction of 0.15, the density approached 98%.

It is postulated that the second, slow regime of densification in SLPS systems seen in Figures 4.12 and 4.13 is governed by the removal of pores from the system. This is difficult, as pores must travel long distances to the sample surface for removal. The migration of pores to sample surfaces is evidenced in Figures 4.26 and 4.27. In addition, the driving stress for this stage is much smaller than that of the initial stage, as it is dominated by the surface energy of the vapour/liquid interface. It is also limited by the pressurization of the gas in the pores. German (1997) gives this driving stress as

$$\sigma = \frac{4\gamma_{LV}}{d_p} - P_g \tag{5.6}$$

where d_p is the pore size, and P_g is the gas pressure in the closed pore. In addition, the final density will also limited by ability of the material to absorb furnace gas at the high temperature. While soluble at the high sintering temperature, any dissolved gas may evolve as pores during rapid cooling.

One phenomenon that remains unexplained is that of the actual *increase* in porosity, or decrease in density, observed in Blend A samples sintered at 1295°C, shown in Figure 4.25. At 1295°C, the liquid content is approximately 20%. While the porosity, found primarily at sample edges, dropped to around 3% after sintering for 30 minutes, after 60 minutes the total pore volume was greater than that present in the green state. Figure 5.7 plots densification parameter as a function of percent liquid for samples sintered for 60 minutes, showing a clear drop in density for the sample sintered at 1295°C. While pore coalescence definitely contributes to the increase in size of the pores seen in Figure 4.25, the increase in volume is more difficult to explain. It appears to be linked to the amount of liquid present, which provides an indication of what might have occurred. It is known that the pores remaining in the system after 60 minutes of liquid phase sintering are closed, since the density is higher than 90%, and gas filled, since the first regime of sintering, driven by capillarity, is finished, leaving the removal of pores responsible for any further densification. This gas could be by-products of deburication and debinding, carbon monoxide evolved from the reaction of carbon in the material with surface oxides, or simply furnace gas. The pressure due to gas in the pores is significant, as the temperature is high, and pressure and temperature are related by the ideal gas law

$$P_g = \frac{nRT}{V} \tag{5.7}$$

where R is the universal gas constant, T is the temperature, n is the number of moles of gas present, and V is the volume of the pores. If there are closed pores present as early as the green state, the pressure differential in these pores at 1300°C is estimated to be approximately 0.58 MPa. This pressure will be lower if the pores close later during the sintering process.

If such pores were present in a solid system, the material would have sufficient rigidity to restrain any expansion due to gas pressure. However, as more and more liquid is introduced to the system, its strength is reduced. At 1295°C, there exists a semi-solid mixture with 20% liquid, and the gas pores, significantly pressurized (on the order of MPa), may apply a stress greater than the yield strength of the weakened metal, causing the blistering and large pores observed in this study. It is possible that 20% may be close to the threshold fraction of liquid necessary to lower the strength of the material below

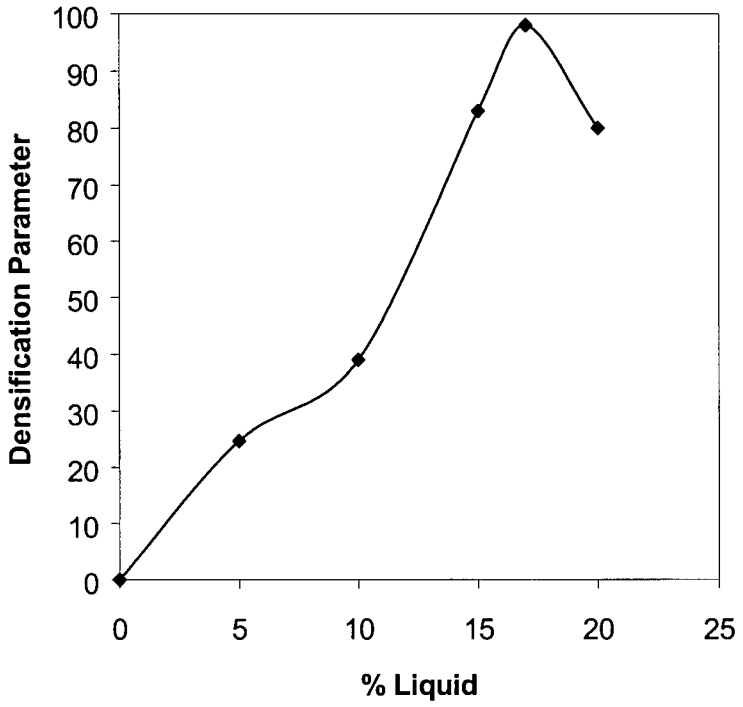

Figure 5.7 Densification as a function of liquid fraction for Blend A samples

the stress exerted by the gas in the pores. If this is true, then temperature control is of the utmost importance, particularly for the sintering of the industrial alloy, Blend B, which is more highly alloyed and will have greater amounts of liquid present at high temperature. While more study of porosity evolution in the presence of high amounts of liquid is necessary, the conclusion is that both of the alloy systems studied have a narrow window of opportunity for successful sintering.

5.6 Cooling Behaviour

The cooling behaviour of the alloys studied appears to be reasonably straightforward. For samples taken to full melting in the DSC, solidification was initiated at temperatures around 1400°C. After completion of solidification, the next significant event to occur was the $\gamma \rightarrow \alpha$ transformation. In all cases, the onset of transformation of transformation was delayed substantially beyond the eutectoid temperature of 723°C, and the majority of samples of both blends did not begin to transform until well below 600°C. However, it is well recognized (Liu, 1995) that small amounts of molybdenum, a component of both powder blends, significantly affects the decomposition of austenite to ferrite in iron–carbon alloys, exerting a significant solute drag force on moving boundaries. The delayed transformation temperatures observed in this work are attributed to the relatively high (0.85wt%) amounts of molybdenum in the materials.

Aside from the late start, in all the samples studied the phase transformation was complicated only in the case of Blend B samples taken to nearly full melting at 1410°C, with a liquid fraction of approximately 0.965. A double transformation peak was observed in these cases. While the double peak might be attributed to some effect of the proprietary alloying additions present in Blend B, since the Blend A samples heated to 1410°C did not exhibit a double peak, this may not be the complete explanation. Recall that at 1410°C, Blend A had a much lower liquid fraction of 0.765. Additional experimental work would be necessary to clarify this phenomenon.

Chapter 6: Conclusions, Summary and Recommendations

The study documented in this thesis was intended to generate an overview of the metallurgical processes involved in the high density supersolidus sintering of an industrially relevant P/M steel. Information about this specific system was provided by means of a broad survey of some important aspects, namely, the thixotropic nature of the system, the effects of time and temperature on densification and porosity evolution, and the effects of secondary issues such as delubrication, homogenization and phase transformation. Subsequently, this allowed for insight into the feasibility of the process, and the identification of critical steps in processing that may warrant additional investigation.

The purpose of this chapter is to summarize the major findings of the study and consequently to put forth some recommendations based on the findings with a view to improving the quality of steel parts sintered by supersolidus sintering. In addition, suggestions are made as to some research avenues that may be worthy of further exploration in the future.

6.1 Summary of Major Findings

1) From differential scanning calorimetry, the following statistics were determined:
   - Evidence from literature and DSC suggests that the debinding and delubrication processes occurring in the samples on initial heating consist of several steps, culminating in thermal pyrolysis, and are completed by 500°C.
   - In both powder blends, A and B, the $\alpha \rightarrow \gamma$ phase transformation begins above the eutectoid temperature and is complete by 850°C.
   - Blend A (Fe-C-Mo) has a solidus temperature of 1227°C and a liquidus temperature that falls in the range 1400 - 1422°C, while Blend B (proprietary) has a solidus of 1213°C and a liquidus temperature in the range of 1400 - 1412°C.
   - In both blends, there is a large degree of undercooling before the $\gamma \rightarrow \alpha$ phase transformation proceeds at temperatures below 600°C. This can be explained

by the solute drag effect exerted by molybdenum during austenite decomposition.

2) The metal powder/graphite mixture homogenizes with respect to carbon content very quickly. This is evidenced by the phase transformation that proceeds at temperatures just above the eutectoid, meaning that the carbon concentration in the metal powder has reached at the very least a minimum value of 0.02 wt%. Diffusion calculations show that the upper temperature limit for homogenization is 970°C under current process conditions. Thus the material will exhibit a homogeneous, bulk concentration of 1.5% well below the temperature of first liquid formation, or even solid state sintering.

3) Solid state sintering occurs during the heating period between the phase transformation temperature and maximum sintering temperature. While densification is minimal, the porosity structure changes significantly from that observed in the green state. The number of pores in a given area decreases markedly and pores begin to spheroidize in shape.

4) The amount of liquid, as determined by the hold temperature, present during sintering has an important role in densification. If insufficient liquid (T_{max}<1280°C) is present, rate of densification is prohibitively slow. If there is superfluous liquid (T_{max} >1295°C), the consequences are shape loss, distortion and blistering. However, in the optimal sintering window between 1280 and 1290°C, densities of greater than 98% theoretical were achieved for both powder blends. Thus, phase diagrams that accurately predict the volume of liquid with temperature are indispensable in the design of a supersolidus sintering program. It is to be noted that the sintering window for this system is extremely narrow.

5) During sintering, porosity tends to migrate to the sample surfaces, particularly when a liquid phase is present. If a high volume of liquid is present, pores may

greatly expand in volume to relieve internal gas pressure, since they cannot be constrained by the non-rigid semi-solid structure.

6) When a liquid phase is present, densification occurs in two regimes. The first involves a fast rate of densification as a result of capillary forces that draw the structure together through viscous flow processes. Approximately 80% of the densification occurs in this regime. This is followed by a much slower rate of densification that is governed by pore removal, ie. pore coalescence, migration to the surface and release to the atmosphere. In this second regime, long holds yield minimal improvements in density.

6.2 Recommendations

1) The current practice is to hold samples at the maximum sintering temperature for times approaching one hour. Since it was observed that most of the densification occurs within the first 30 minutes, it may be beneficial to reduce the hold time to 30 or 45 minutes, if a small decrease in final density is tolerable. Holding for 60 minutes yields only minimal improvement of the density achieved at 30 minutes, yet the probability of pore agglomeration is much greater.

2) It is documented in the literature that at green densities of approximately 90%, there is change from an open, interconnected porosity network to a condition of isolated, closed porosity, and this is evidenced in the green structure observed in this work. Prior to any heat treatment, these pores are saturated with binder and lubricant. While there is no specific evidence that there is residual lubricant, binder or entrapped gas in the pores after sintering, it is suggested that the green density be reduced, at the least to approximately 85% to facilitate the extraction of any products inside the pores. Because supersolidus sintering is such an effective means of densification, it is predicted that a small decrease in green density will not have any effect on the

final density achievable. It may, however, have an effect on the distortion behaviour of compacts.

3) Due to the high sensitivity of liquid volume to temperature in the alloys examined, and the absence of an adequate sintering window, process control is of the utmost importance in successful sintering of these alloys. It is recommended that the maximum temperature not exceed 1285°C.

4) Due to the difficulties inherent to the sintering of these particular alloys, especially the small sintering window, it would be worth investigating, in a scientific way, possible modifications in the chemistry of the alloy that would result in an improvement in sinterability. An alloy with less sensitivity of liquid volume to temperature might be suitable. Software such as Thermocalc™ would be valuable in this type of endeavour.

6.3 Future Work

There are a number of possibilities for a continuation of research in supersolidus sintering of steels for high density applications. As mentioned, this work was intended as a broad study and any aspect of it could be examined more comprehensively. A key result of this study was the identification of a link between the fraction of liquid present and the tradeoff between densification and pore enlargement. Now that the phase equilibrium information has been established, an in-depth look at density evolution as a function of liquid formation with a more quantitative look at the porosity profile is possible. It would also be interesting to study the mechanical properties of the solid-liquid system in an effort to learn more about pore enlargement.

Design of an alloy with a more robust sintering window but with the same general attributes would also be of practical importance. A study of the mechanical properties of the material, specifically strength and fatigue life, is also warranted as it is these properties that will determine the success of this material in automotive applications. Finally, the unusual phase transformation behaviour of the proprietary alloy, as

discovered in the DSC experiments, is as yet unexplained, and poses an interesting, if not critical problem.

6.4 Final Remarks

While the process of supersolidus liquid phase sintering has not been used extensively in industrial powder metallurgy operations, it is clear that there is excellent potential for the production of high or full density components. This particular study established some fundamental data on one industrially relevant system. Further research will certainly help to eliminate the processing sensitivities that preclude SLPS as a viable alternative to expensive mechanically-assisted P/M routes. In particular, the acquisition of accurate phase diagram information provides an excellent initial foundation for the development of a robust supersolidus sintering operation.

References

Allibert, C.H., "Present Knowledge on Liquid Phase Sintering", Advances in Powder Metallurgy and Particulate Materials, Metal Powder Industries Federation, Princeton, NJ, 1998.

Ashby, M., "A First Report on Sintering Diagrams", Acta Metallurgia, Vol. 22, March, 1974, pp. 275-289.

Bala, S.R., and Lund, J.A., "Studies of the supersolidus sintering of cupronickel powder", Zeitschrift fur Metallkunde, Vol. 70, No.3, March, 1979, pp. 185-190.

Beddow, J.K., The Production of Metal Powders by Atomization, Heyden and Son Ltd., London, England, 1978.

Bester et al., "Estimation of Average Values for Diffusivity of C, O, H, N and S in Solid and Molten Fe", Arch. Eisenhuttenwesen, Vol. 43,April, 1972, p. 207-213.

Borg, R.J. and Dienes, G.J., The Physical Chemistry of Solids, Academic Press, Inc., San Diego, 1992.

Bowman, H.A. et al., "Procedure for High Density Precision Density Determinations by Hydrostatic Weighing", Journal of Research of the National Bureau of Standards C", Vol.71C, No.3, 1967, pp.179-198.

Cambal, L. and Lund, J.A., "Supersolidus sintering of loose steel powders", International Journal of Powder Metallurgy, Vol. 8, No.3, 1972, pp.131-140.

Cannon, H.S. and Lenel, F.V., "Some observations on the mechanism of liquid phase sintering", Metallwork Plansee, Austria, 1953, pp. 106-121.

Chalmers, B., Principles of Solidification, John Wiley and Sons, New York, 1964.

Crank, J., The Mathematics of Diffusion, Clarendon Press, Oxford, 1975.

Evans, J.W. and DeJonghe, L.C., The Production of Inorganic Materials, Macmillan Publishing Co., Toronto, 1991.

German, R., Powder Metallurgy of Iron and Steel, Wiley, New York, 1998.

German, R., "Supersolidus liquid phase sintering of prealloyed powders", Metallurgical and Materials Transaction A, Vol.28A, July 1997, pp. 1553-1567.

German, R., "Advances in high alloy sintering using supersolidus liquids", Advances in Powder Metallurgy and Particulate Materials, Metal Powder Industries Federation, Princeton, NJ, 1997.

German, R.M., "Thermal Extraction of Binders and Lubricants in Sintering", Advances in Powder Metallurgy and Particulate Materials, MPIF, Princeton, NJ, 1996, p. 10.3-10.15.

German, R., Powder Metallurgy Science, Metal Powder Industries Federation, Princeton, NJ, 1994.

German, R., "Supersolidus liquid phase sintering part I: Process review", International Journal of Powder Metallurgy, Vol. 26, No.1, 1990, pp. 23-34.

German, R. "Supersolidus liquid phase sintering part II: Densification theory", International Journal of Powder Metallurgy, Vol. 26, No.1, 1990, pp. 35-43.

German, R., Liquid Phase Sintering, Plenum Press, New York, 1985.

Guyard, C., et al., "Liquid phase sintering of prealloyed powders of Co-base alloys", Science of Sintering, Vol. 13, Sept. 1981, pp.173-160.

Heady, R.B. and Cahn, J.W., "Analysis of the capillary forces in liquid phase sintering of spherical particles", Metallurgical Transactions, Vol.1, No.1, 1970, pp. 185-189.

Hemminger,W., Calorimtery: Fundamentals and Practice, Weinheim, Deerfield Beach, FL, 1984.

Jesberger, T.J. and Reardon, D.P., "Delubrication byproduct reactions using various assist systems of powdered metal compacts", Advances in Powder Metallurgy and Particulate Materials, MPIF, Princeton, NJ, 1996, pp. 10.17-10.26.

Johnson, D.L., and Su, H., "The master sintering curve", Advances in Powder Metallurgy and Particulate Materials, MPIF, Princeton, NJ, 1997, pp. 14.115-14.121

Jones, P.K. et al., "Densification strategies for advanced high endurance P/M components", Advances in Powder Metallurgy and Particulate Materials, Metal Powder Industries Federation, Princeton, NJ, 1996.

Kingery, W.D., " Densification during sintering in the presence of a liquid phase", Journal of Applied Physics, 1959, Vol.30, pp. 301-306.

Krielaart, G.P. et al., "Analysis of phase transformation in Fe-C alloys using differential scanning calorimetry", Journal of Materials Science, Vol. 31, 1996, pp. 1501-1508.

Lal, A. and German, R., "The role of viscosity during liquid phase sintering", Advances in Powder Metallurgy and Particulate Materials, Metal Powder Industries Federation, Princeton, NJ, 2000.

Legzdins, C.F., "Delubrication of Powder Metallurgical Compacts", PhD Thesis, University of British Columbia, 2000.

Lesuer, D.R. et al., "Ultrahigh carbon steel for automotive applications", SAE Technical Paper Series, Warrendale, PA, 1996, pp. 159-168.

Liu, J. et al., "Densification and shape retention in supersolidus liquid phase sintering", Acta Materialia, Vol. 47, No.18, 1999, pp. 4615-4626.

Liu, Z.K., "The transformation phenomena in Fe-C-Mo alloys: a solute drag approach", Phase transformations during the thermal/mechanical processing of steel, Vancouver, Canadian Institute of Mining, Metallurgy and Petroleum, 1995, p.65.

Lund, J.A. and Bala, S.R., "Supersolidus sintering", Modern Developments in Powder Metallurgy, Vol.6, Metal Powder Industries Federation, Princeton, NJ, 1974, p.409-421.

Lund, J.A. et al., "Supersolidus liquid phase sintering of a prealloyed monel powder", Powder Metallurgy International, Vol.4, No.4, 1974, pp.174-175.

Metal Powder Industries Federation, "Standard Test Methods for Metal Powders and Powder Metallurgy Products", MPIF, Princeton, NJ, 1996.

Molinari, A. et al., "Investigation of liquid-phase sintering by image analysis", Materials Characterization, Vol. 34, 1995, pp. 271-276.

Myers, N.S. et al., "Supersolidus liquid phase sintering of PIM M2 tool steel", Advances in Powder Metallurgy and Particulate Materials, Metal Powder Industries Federation, Princeton, NJ, 1998.

Podob, M.T. et al., "The mechanism of sintering high speed steel to full density", Modern Developments in Powder Metallurgy, Metal Powder Industries Federation, Princeton, NJ, 1981, pp. 93-112.

Prutton, M., Introduction to Surface Physics, Oxford University Press, New York, 1998.

Shewmon, P., Diffusion in Solids, 2nd Edition, TMS, Materials Park, PA, 1989.

Su, H. and Johnson, D.L., "Master sintering curve: A practical approach to sintering", Journal of the American Ceramic Society, Vol. 79, No. 12, 1996, pp. 3211-3217.

Takajo, S. et al., "Behavior of liquid phase sintering of high speed steel powder compacts", Journal of the Japanese Society for Powder Metallurgy, Vol.33, No. 8, 1986, pp. 398-401.

Vollertson, F., "Optimizing liquid-phase sintering by temperature-limit-diagrams", Metal Powder Report, February, 1991, p. 45-48.

Westerman, E.J., "Sintering of Nickel-Base Superalloys", Transactions of the TMS-AIME, Vol. 224, 1962, p.159-164.

Wright, C.S. et al., "Supersolidus sintering of high speed steels. III: Computer aided design of sinterable alloys", Powder Metallurgy (UK), Vol. 42, No. 2, 1999, pp.131-146.

Wright, C.S. et al., "Supersolidus sintering of high speed steels. II: Sintering of tungsten based alloys", Powder Metallurgy (UK), Vol.38, no. 3, 1995, pp. 221-229.

Wright, C.S. et al., "Supersolidus sintering of high speed tool steels- comparison of sintering theory with experimental observations", Solid State Phenomena, Vol. 25-26, 1992, pp. 463-470.